CFD study on the Ocean Grazer Wave Energy Converter

Author: E.A Neven

Supervisors: Antonis Vakis (Mechanical Engineering)
Eize Stamhuis (Energy and Environmental Sciences)

June 11, 2021

Abstract

In this study, a CFD model is developed for the analysis of the Ocean Grazer wave energy converter. The model is developed in COMSOL. In previous time and frequency domain models, the floaters have been fixed in surge, which is a big assumption. In this study, the floaters are connected by a distance joint. This distance joint is represented by a rod connecting the floaters. The motion and interactions of the bodies are computed using multibody dynamics. Besides the interactions of the bodies, the energy extraction of wave energy converters is analyzed as well. The damping coefficient, which is used to model energy extraction is optimized for a real-time wave. One of the main findings is that a more dense floater array has higher performance, caused by radiation effects. The model including multibody dynamics is compared to fixed floaters to obtain insight into the assumption to fix the floaters in surge. The result from this comparison is that the connected floaters' energy production is slightly smaller. The decrease in produced power is caused by energy losses due to increased rotations and displacement in surge. Besides the performance, it was found that it is important to look at the floaters' motion caused by the flow field of the wave. The motion of the connected floaters do have a big impact on each other, causing collisions in some situations.

Acknowledgements

Contents

1 Introduction

One of the main problems related to energy is the fact that the consumption is increasing [1] each day (see Figure 1). To cope with this increase in demand for energy, the response has been to use fossil fuels [2] (see Figure 2), which can easily be converted to energy by combustion. Due to the increase in demand, the reserves for fossil fuels are reduced every day, since the regeneration of fossil fuels is a lot slower than the current consumption.
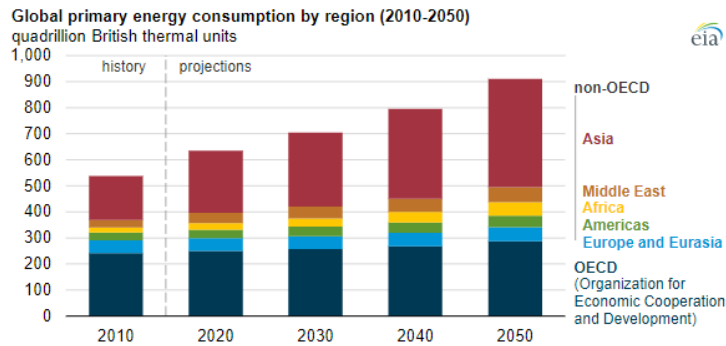
Figure 1: EIA predictions of energy consumption estimated in 2019 [1].

Figure 2: BP review of global fossil fuel consumption [3].

As can be seen in Figure 3, the reserves for different fossil fuel sources are presented, with an estimation of the lifetime of the resource. The largest reserve is coal since coal has a smaller energy density compared to oil and gas and is least favorable. The reserves for oil and gas a lower, the estimated reserve is about 55

years for both the oil and gas. The reserve for coal has a lifespan of 110 years. As mentioned before, the production of fossil fuels is not even close to the consumption and will therefore deplete eventually.
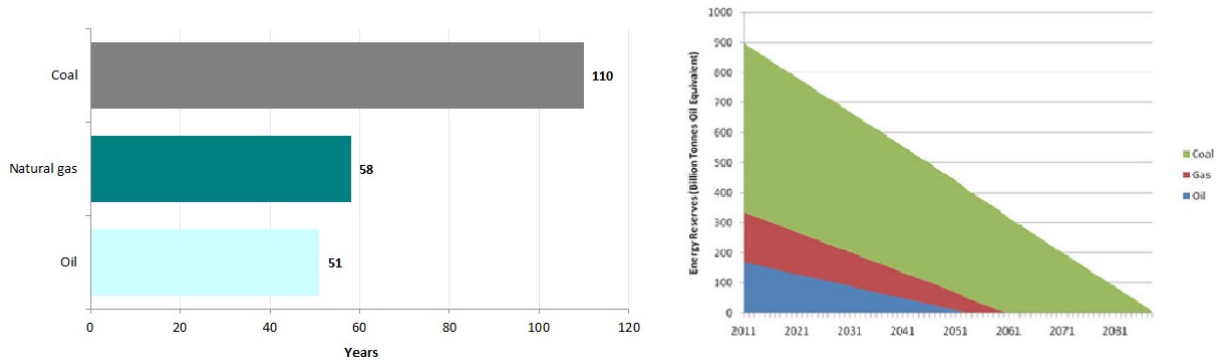
Figure 3: Fossil fuels world reserves [4] (left). In the right picture, the prediction of the depletion of fossil fuels is presented [5].

Besides the fact that fossil fuels are running low on supply, the combustion of fossil fuels has a second devastating effect, known as global warming. Global warming occurs due to the addition of CO_2 and other particles like NO_x to the atmosphere (see Figure 4). The particles increase the temperature on earth, because the heat generated on earth is kept in the atmosphere, due to the addition of particles (like CO_2 and NO_x) that radiate the heat back to earth, whereas normally the heat would leave the atmosphere [6]. The effect is also called the greenhouse effect, because the addition of pollutants keeps the heat inside the 'greenhouse' created by the particles. The main effect of global warming is the increase of the temperature on earth Figure 5. The effects of even a small increase in temperature can be disastrous for ecosystems [7].
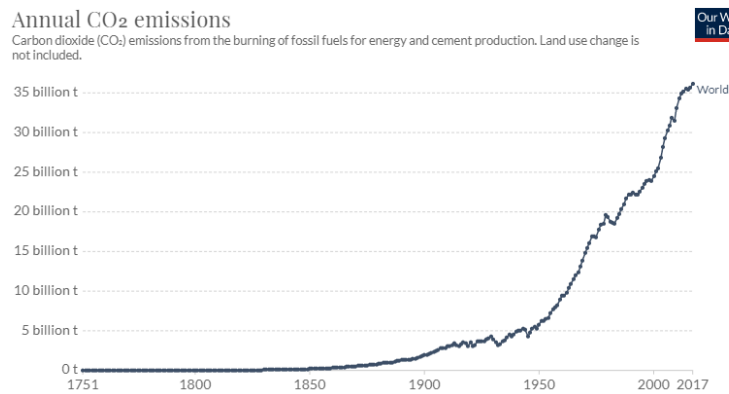
Figure 4: Annual Carbon dioxide (CO_2) emissions from combustion of fossil fuels for energy and cement production [8].

RECENT TEMPERATURE TRENDS (1990-2019)
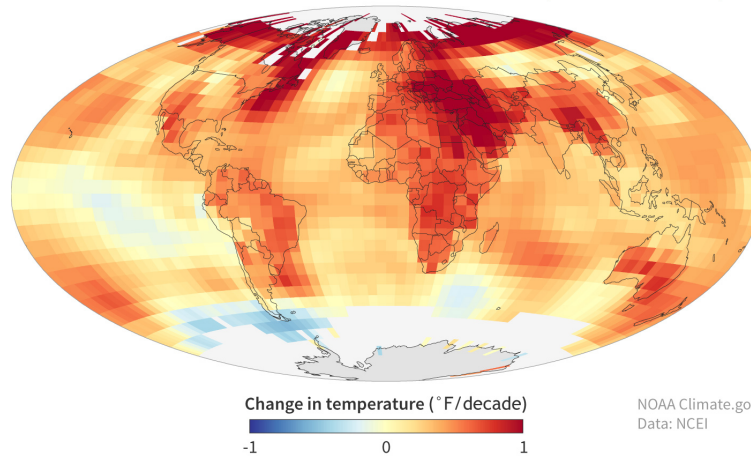
Figure 5: Recent temperature trends 1990-2019 [9] note that 1 F $= \frac{5}{9}$ degrees Celsius.

1.1 Renewable energy

To cope with the depletion of resources and global warming, an alternative to cope with the increasing energy demand has to be found, without the use of fossil fuels. The solution to this problem is renewable energy, which is named renewable since there is an infinite supply available. The most known renewable energy sources are solar and wind energy. Solar energy is harvested with the use of solar panels, where the photon's energy is captured by the panel and converted to electrical energy [10].

Wind energy is harvested with the use of wind turbines, where the mechanical motion caused by the lift of the blades is converted to electrical energy [11]. Wind turbines can be placed either on-shore or off-shore, where for off-shore turbines the power generation is larger, but the installation and maintenance costs are higher [12].

Besides Solar and Wind energy, there are also other types of renewable energy.

1. Hydro energy: The energy from the flow of waters is captured using a turbine-like system, where the flow from e.g. rivers is used to drive a dynamo-like mechanism to capture the kinematic energy from the water and convert it to electrical energy [13].

2. Geothermal energy: The heat from the core of the earth is used to extract power using the heat. This requires deep drilling operations which can be quite expensive. For most systems, water is pumped through pipes that are exposed to the 'warmer' areas. This is used for either driving a turbine, or the heated water can be used directly in homes or other facilities [14].

3. Biomass: Plants can be combusted to generate electricity. The amount of land needed for energy production is massive for biomass.

1.2 Ocean energy

Another source of renewable energy, which is often overlooked, is Ocean energy. Ocean energy is energy that is available in oceanic environments. There are different types of oceanic energy extraction, the most important are listed below.

1. Tidal energy: Tidal energy is energy captured from the tides. The main working mechanism is comparable to hydro energy since the flow of water is used to produce electricity using turbines. With regard to tidal energy, the difference in height of the tides is the main driver behind the flow of the water and therefore for harvesting energy.

2. Wave energy: Wave energy is the energy that is present in waves. The waves present in the ocean are created by different sources, which will be discussed later on.

The main issue with tidal energy is that there are limited sites that are available for construction. The main advantage of tidal energy is that the production of energy is easy to predict since it is known when the switch of the tides takes place [15].

Wave energy, on the other hand, has a huge potential. The main reason for this is the fact that there is a lot of space available for such an energy harvester, especially due to the fact that the system is placed off-shore. Wave energy has some other advantages as well:

- Reliability: Ocean energy is a very reliable energy source.

- Predictability: Ocean energy is predictable. The predictability is a lot higher compared to wind energy for example [16].

- High energy density: Wave energy has a high energy density. The estimated potential is 80,000 Twh, which is 5 times the global energy consumption [16].

1.3   Ocean Grazer

The Ocean Grazer is a novel concept, where not only electricity is generated from ocean energy, but can also be stored at the source [17]. Research on the Ocean Grazer started in 2013 and the inventor is Drs. W.A. Prins. Currently, the latest version of the Ocean Grazer is the Ocean Grazer 3.0. In 2018, the Ocean Grazer company was launched. Most research for the Ocean Grazer is conducted by the University of Groningen, who are closely connected to the company side of the Ocean Grazer.

Figure 6: Large scale Ocean Grazer energy farm [18].

To capture the energy from the waves, wave energy converters (WECs) are used. Wave energy converters use the vertical displacement of a floater from the incident wave to generate power. In the current configuration of the Ocean Grazer, multiple smaller floaters are placed in a certain formation, where the floaters are connected to another through hinges [18]. For more information on WECs, consult Section 3.1. In Figure 6 the orange floating object are the floaters, which are connected to the power take-off (PTO) to extract energy

The Ocean Grazer does not only comprise floaters but also a PTO and a storage method. The PTO system converts the heave motion of the floaters into potential energy. The PTO of the Ocean Grazer uses the heave of the buoys' motion to pump water into a flexible bladder, where the energy is stored. To generate electrical energy, the water is released from the bladder and enters the lower level, where electrical energy is generated by a turbine. The working fluid is then released in the reservoir, where the cycle is completed

and can be repeated. One of the main advantages of this system is that it is a closed system, so no exchange of fluids is possible. Because multiple pumps are present, the whole PTO system is called the multi-piston, multi-pump PTO (MP2PTO). A schematic view is presented below in Figure 7. The main idea of multiple pumps is that the pumps can be tuned for different wave properties.
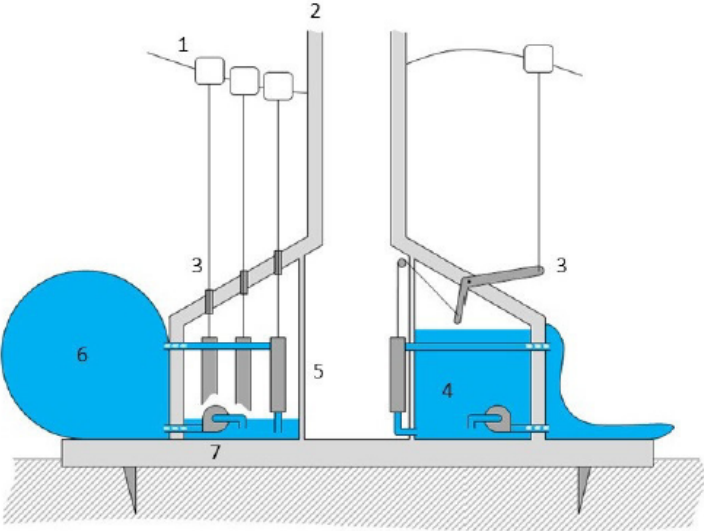
Figure 7: Ocean Grazer 3.0 schematic view [18].

The Ocean Grazer is the main focus of this project, where research of the energy extraction of the WECs is the main goal.

2   Problem description

Currently, the Ocean Grazer is still in development. In the current phase, modeling is used widely. Modeling is a cheaper option compared to prototypes, where the results can be quite accurate. In this study, the main focus is on the wave energy converters (WECs) of the Ocean Grazer. For the WECs, a lot of time and time and frequency-domain models have been used to analyze power extraction. An example is WEC-SIM, which is an open-source code used to simulate wave energy converters. The main disadvantage of such models is that they employ a long list of assumptions. Another disadvantage is that there is little insight in the flow field. Besides this, these models are heavily dependent on linear wave theory to extract the hydrodynamic coefficients for which the classical BEM method is used. The effect of harvesting energy from a wave might have an effect on the field of the wave, which might either increase or decrease the energy available for the next floater. This is illustrated in Figure 8
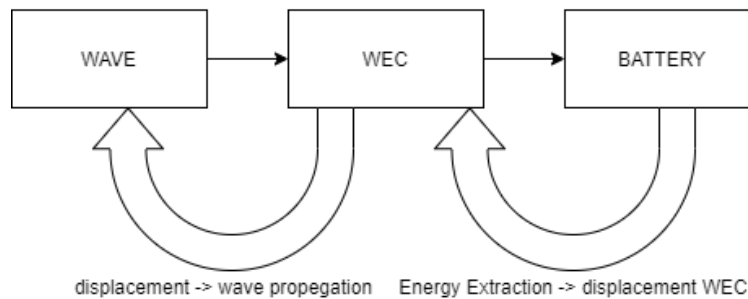
Figure 8: The concept of the dynamics of the system.

To obtain insight into both the behavior of the floater and the fluid flow, a CFD model is developed. The main advantage of a CFD model is that the behavior of fluid flow can be analyzed.

Another reason to develop a CFD model is to obtain insight into the interactions between the floaters. In a real floater array, the floaters are connected to keep them in place. In the current models, one of the assumptions is that the floaters are fixed in the x-direction (surge). This is not realistic for a real floater array and the model should be able to deal with the multibody dynamics of the system. Secondly, a CFD model gives more insight in the actual movements of the floaters.

2.1   Goal of the research

The goal of this study is to deliver a model:

- That can deal with all the effects mentioned above, including the energy-related equations.

- Is able to analyze the floaters' motion, which is not fixed in the x-direction (surge).

- Is able to include the multibody dynamics, to obtain insight into the interaction of the floaters.

- Is able to give some insight into the effect of energy extraction on the fluid flow of the wave.

The deliverable is a model that satisfies the goals mentioned above. Besides the model, an analysis of a real-life situation should be delivered as well. This implies that a wave from real data is used in the model. The analysis that will be conducted is partially a comparison study, where a comparison is made between fixed floaters and connected floaters. Fixed floaters are fixed in the x-direction. For the comparison, different floater arrays with different shapes are tested.

Besides the analysis of the motion of the floaters, the flow field will be analyzed as well, for different situations. In this analysis, some insight into the behavior of the flow after energy extraction should be obtained.

Besides the effect of energy extraction, the motion and behavior of the floater should be analyzed

Finally, the power produced by the floater array will be discussed. The power produced is the key performance indicator of the floater arrays and is therefore quite important. For the power produced, the most important factors regarding power production should be identified and discussed.

2.2 Scoping of the research

Scoping for the model is important because CFD is highly complex and some factors may have to be left out or simplified to decrease the computational times. In this section, the scoping of the research is explained.

2D approach The model is a two-dimensional (2D) model. A 3D model would take extremely long to compute and is very complex. The complexity is due to a large amount of fluid flow, combined with the multiphysics of the rigid floaters in the fluid domains. Since the model has to be developed from scratch, a 2D approach is chosen.

Regular waves For the simulation of ocean waves, there are two options. Ocean waves consist of multiple types of waves, that form a wave with a variable period/wavelength, which are called irregular waves (see Section 3.5 for a more in-depth explanation). For this research, regular waves are assumed, with a constant period and wavelength. The main reason for this is that the modeling is not only easier, but the results are also easier to interpret since the waves are stable and predictable.

Connection floater and PTO In the real system, the floaters are connected to the PTO with cables. In this study, the cables are not taken into account. Since the model is a 2D model, there is no physical way to model the cables, since the flow cannot evolve around the cable. The PTO system is modeled as a mass-damper applied to the center of mass of the floaters. The cable is not actually present in the model.

2.3 Research Questions

The research questions are derived from the problem statement and goal.

- How can a CFD model be developed and used to analyze the floaters?

- What is the effect of the inclusion of the floater interactions on the energy production and the flow field?

- What is the effect of different array configurations and floater shapes on the energy production and flow field?

The second research question deals with the interaction of the floaters and the effect on the flowfield. The third question deals with the analysis of different floater array configurations and shapes. The main reason for this question is to get insight into the behavior of different shapes and arrays. The energy production is the key performance indicator of a floater array and the flow field is key to obtain insight into the behavior of the flow and motion of the floaters.

2.3.1 Sub questions

The sub-questions deal with parts of the research questions:

- How can a free-surface wave be created in COMSOL?

- How can a WEC be modeled in a CFD environment?

- What is the effect of the floaters' motion on the neighboring floaters?

- What is the effect of the floaters' interaction on the power production?

- What is the effect on the wave if a floater is modeled with the forced displacement caused by the power extraction?

- What is the effect of different floater shapes on the power production and flow field?

- What is the effect of different floater arrays on the power production and flow field?

2.4   Stakeholder analysis

In this section, a short stakeholder analysis is conducted.

Inventor, Drs. W.A. Prins   The inventor of the Ocean Grazer, Wout Prins, is closely connected to both the company side of the Ocean Grazer and the Research group. Wout Prins is one of the main stakeholders, as the inventor and scientific advisor.

Ocean Grazer company   The company is the business side of the Ocean Grazer. The company has a stake in this project because the model is relevant to the design of the wave energy converters of the Ocean Grazer. Nowadays, the focus of the company is more on the Ocean Battery, and therefore the company might currently be a little less interested in the wave energy converters.

Supervisors   The first supervisor of this project, prof. dr. Antonis Vakis is a scientific advisor for the Ocean Grazer company. Antonis Vakis is a major stakeholder in this project, interested in CFD models for the Ocean Grazer. The research side of the subject has the main focus, where Antonis Vakis is the main stakeholder.

The second supervisor for this project is dr. E.J. Stamhuis. dr. E.J. Stamhuis is an expert on CFD and plays a supportive role during the project. Besides knowledge of CFD, dr. E.J. Stamhuis is also very knowledgeable in fluid mechanics. dr. E.J. Stamhuis is not directly part of the Ocean Grazer group but is closely related.

Students   Since the Ocean Grazer group consists of students and PHD's all working on the Ocean Grazer design and application, there is an interest from the current and future students at the Ocean Grazer group.

2.5   Software selection

For the model, there are a few software packages available.

- COMSOL: COMSOL is a commercial multiphysics software package. COMSOL is used widely in industry and for educational purposes. COMSOL is not a CFD specialized software package but has some modules that solve for CFD. The CFD module is used to compute CFD-related problems, which can be coupled to other physics. An example is the multibody dynamics module, which includes solvers to model complex multibody dynamics and interactions [19].

- OpenFOAM: OpenFOAM is an open-source software package, solely used for CFD. OpenFOAM is a Linux-based package. OpenFOAM is used widely, mainly because the software is free. OpenFOAM is used for different applications, from industrial environments (e.g pipe-flow) to aeronautics [20].

- ComFLOW: ComFLOW is a CFD package developed at the Rijksuniversiteit Groningen. ComFLOW is specialized in free-surface flow. Currently, the main focus of the software is on 'the prediction of hydrodynamic wave loading on ships and offshore platforms' [21].

The software that is selected is COMSOL. The main reason for this is the multiphysics presented in the model. The combination of fluid mechanics, phase field tracking and multibody dynamics is quite complicated. In COMSOL, the different modules are available and are coupled quite easily. The main issue with the OpenFOAM and ComFLOW is the fact that structural mechanics and multibody dynamics are not present in the solver, which implies that a solver has to be created to include the multi-body interactions. This is quite complex and might take more time than is available for this project.

3   Theoretical background

In this section, the theoretical background is discussed.

3.1   Classification of WECs

There are different types of WECs, with different mechanisms. There is a general classification for WECs, that deals mostly with the direction of the incident waves and the orientation of the WEC. There are three main types: terminator, attenuator and point absorber WECs. In Figure 9, a schematic view is given of these devices [22].
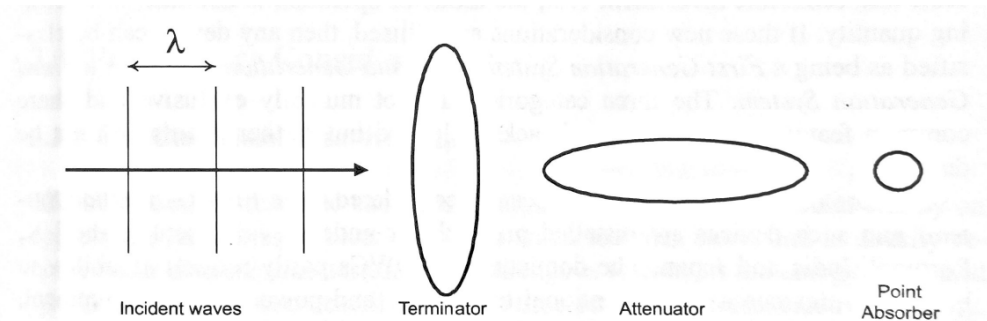
Figure 9: Schematic view of the orientation of the WEC with regard to the incoming wave, where λ represents the wavelength [22].

As one can see, the designs have a different strategy to capture energy from incidental waves. The terminator uses the depth of the water column under the wave, whereas the attenuator uses more of the wavelength to its advantage. Point absorbers are relatively small compared to the other designs, which are often used in a formation with multiple point absorbers. Some of the main advantages of point absorbers are mentioned below [22]:

1. The device is unidirectional, meaning that the direction of the incoming wave does not affect the performance.

2. Because the dimensions of the WEC are relatively small compared to the wavelength, there is less scattering.

3. Besides the efficiency of the point absorber, the point absorber is prone to fewer forces. The main reason for this is that the body moves with the wave, where the direction of the incident wave has little impact.

Attenuators and terminators need a controlling mechanism to ensure that the orientation with respect to the direction of the incident wave is correct. Without control, the WEC is inefficient. Examples of point absorbers, attenuators and terminators are given in the next section.

3.2   Examples of point absorbers, attenuators and terminators devices

In this section, some examples of ongoing projects for the devices mentioned above are explained briefly.

3.2.1   The Aguçadoura wave farm

A famous example of an attenuator WEC is the Aguçadoura wave farm, located offshore from the coast of Portugal. The total amount of energy installed was 2.25MW. The mechanism for this attenuator uses a hydraulic pump, which pumps oil through hydraulic motors. The oil driving the motors is displaced by floating buoys powered by the incident wave, which are flexible and can bend to displace the oil. The main problem with this farm and the reason that it was shut down 2 months later, is the fact that there was a

specific problem related to maintenance of the bearings. The company that supplied the WECs went into voluntary administration and therefore the WECs were never repaired [23].

The wave energy converters were produced by the Scottish company Pelamis Wave Power, which went bankrupt in 2014. A schematic view of the Pelamis wave energy converters can be found below in Figure 10.
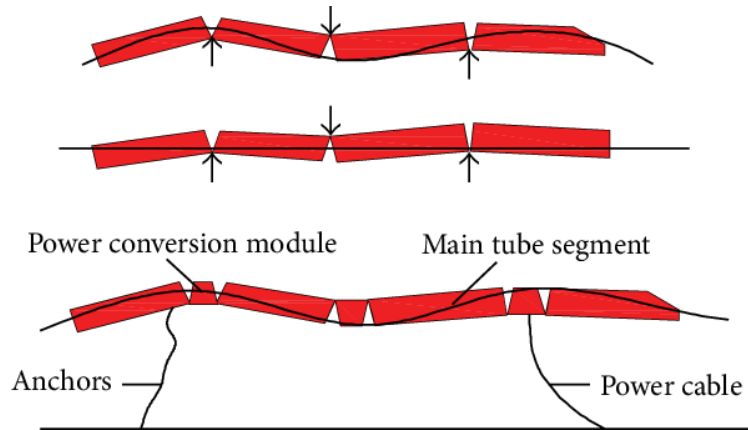
Figure 10: Working principle of the Pelamis wave energy converter [24].

As one can see, there is a difference in height due to the heave of the wave, which lifts a certain part of the Pelamis WEC. Because of the lifting, the oil will flow towards the lower area, where the oil drives the turbines [24]. As mentioned before, the main problem with an attenuator like the Pelamis wave energy converter is the fact that the direction of the incident wave is quite important; without control there is no or low power generation. Besides power generation, the WECs are prone to large forces if the direction of the incident wave is not optimal.

3.2.2   The Oyster wave energy converter

An example of a terminator wave energy converter is the Oyster project. In Figure 11, a side view of the Oyster is presented. As one can see, the Oyster uses the complete depth of the water column, hence it is classified as a terminator. The main working principle for the Oyster is the seawater piston. The flap of the Oyster is pushed by the waves, where the hydraulic piston pump fluid to the surface and the displacement of the fluid is used to generate the energy using turbines [25].
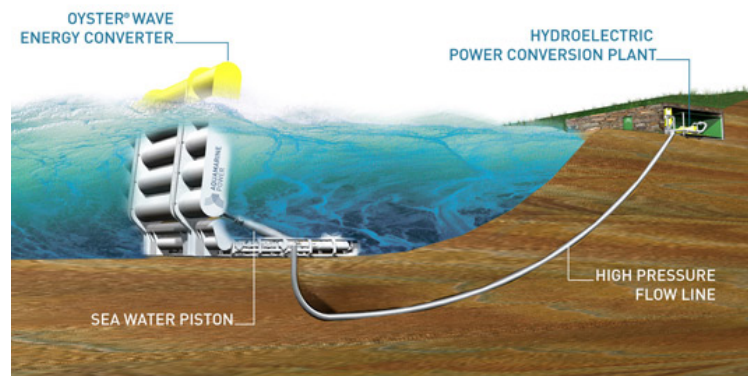
Figure 11: The working principle of the Oyster WEC [5].

The Oyster project is an ongoing project. In 2009 the first Oyster was installed and connected to the British grid. The current developments are on Oyster 2, an improved version of Oyster 1. The main disadvantage

of the Oyster is that it is designed for a depth of 10-12 meters. This implies that the total area available for harvesting ocean energy with the Oyster is rather small. The direction of the incident is also important, since the device is not unidirectional. Because the Oyster is placed near the shore, the direction of the incident waves is predictable, due to the effect of the seabed on the waves.

3.2.3   Powerbuoy

An example of a point absorber WEC is the Powerbuoy WEC. The Powerbuoy is a point absorber WEC, where the main working mechanism is the heave of the buoy due to the incidental wave, which is converted to electrical energy. The Powerbuoy is present in multiple locations, mostly in the US and Australia [26]. A side-view of the Powerbuoy can be found in Figure 12.
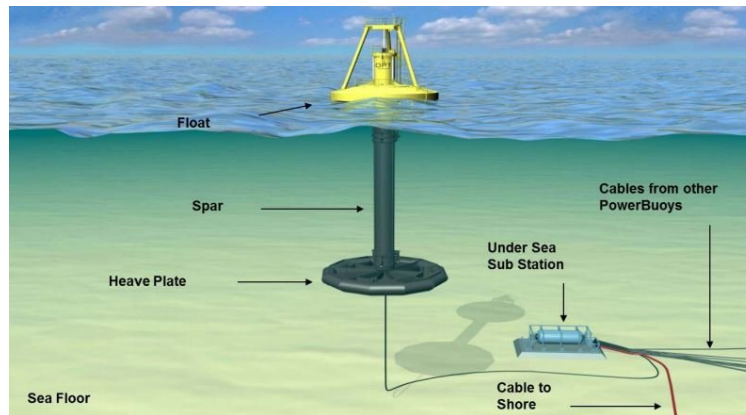
Figure 12: Concept of the Powerbuoy WEC [26].

As mentioned before, there are multiple advantages using a point absorber WEC. An example for a disadvantage for a terminator WEC is that the Oyster has a large influence on the flow, where it might be inefficient to use multiple Oyster devices in a relatively small area. In 2014 an aerospace company built the largest wave energy farm, near Victoria. The wave energy converters used are Powerbuoys to support the case that point absorbers are the most efficient for large-scale wave energy harvesting [27].

3.2.4   Other WEC devices

There are a few other devices that capture ocean energy, which are discussed briefly.

Oscillating water column systems   Besides the WECs mentioned before, there are other types of WECs, which cannot be classified as easily. An example is the oscillating water column (OWC) WEC. An OWC can only be placed near the shore since its main working mechanism is to capture the incident wave and convert its energy using pressure in a cabin to drive turbines. A schematic overview is given below in Figure 13.
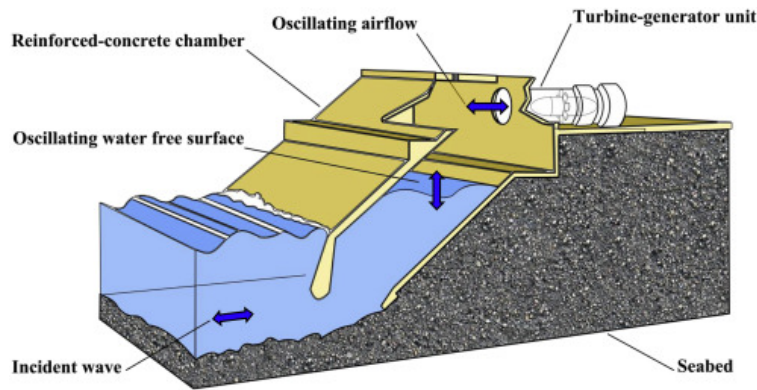
Figure 13: Schematic view of an OWC device with a Wells turbine [28].

The concept is that the incident wave enters a cabin, where the air present in the room is pressurized because of the incident wave and reduces the total space available for air. The pressurized air flows through a turbine, where electrical energy is produced [28]. The main disadvantage of this device is the fact that it can only be built on the shore, where little space is available if applied on large scale.

Overtopping terminator systems The overtopping terminator is a device that collects water in a reservoir, which is captured when the water flows over the device. The potential energy of the water is then used to drive a turbine and generate electrical energy [29]. In Figure 14, a schematic view of two overtopping terminator devices is presented. In the left picture, a schematic view of a floating, offshore overtopping terminator is presented. On the right, an onshore overtopping terminator is presented.
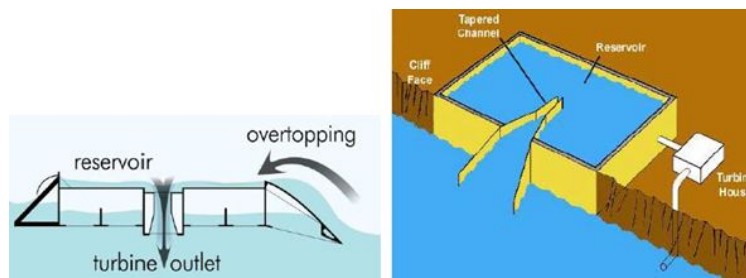
Figure 14: Offshore versus onshore overtopping terminators [29].

3.3 Ocean waves

The most important properties of ocean waves are the period of the wave, the wavelength and the amplitude. The period of a wave is the time for a wave to complete one full cycle. The period is often replaced by the angular velocity of the wave, which is found by:

$$\omega = \frac{T}{2\pi} \tag{1}$$

where T is the period of the wave and ω is the angular velocity of the wave.

Next, the surface elevation is introduced. The surface elevation is the total elevation of the highest point (crest) with respect to the still water level. The wave height is also an important factor, which is double the amplitude and represents the total height from crest to trough. In the figure below, one can see the properties discussed.
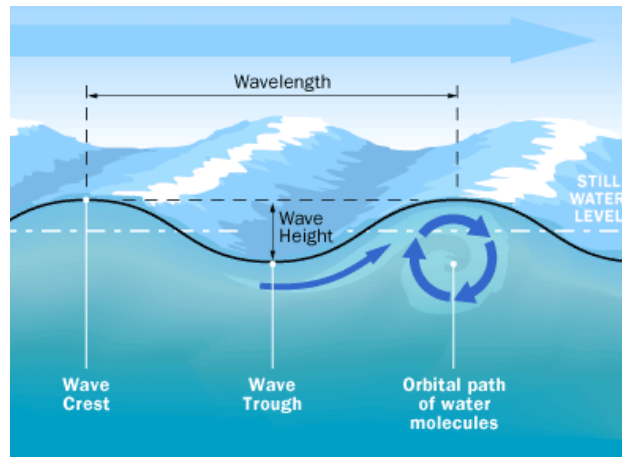
Figure 15: Properties of a wave [30].

3.4 Types of waves

Ocean waves are irregular waves, a superposition of waves with different periods and heights. The main reason that the waves have different periods and wave heights is that they are created by different mechanisms. Some of the most frequent mechanisms are listed below [31]. In Figure 16, the different types of waves causing the irregular wave are discussed, alongside an indication of their periods.

- Trans-tidal waves: Trans-tidal waves are waves generated by the low-frequency fluctuations of the earth's crust. Trans-tidal waves have the longest period of ocean waves.

- Tides: Tides are generated by the interaction of the ocean and the movement of the moon and the sun.

- Storm surges: Storm surges are waves generated by storms and cause a general surface elevation, where the surface elevation is caused by the pressure difference induced by the storm. The period of the waves is rather large, as they scale directly with the storm.

- Tsunamis: Tsunamis are a smaller scale storm surge.

- Infra-gravity waves: Infra-Gravity waves are waves generated by wind; their period is roughly a few minutes.

- Seiches: Seiches are waves generated by the resonance of the basin of the ocean. These waves are difficult to predict and vary widely in frequency.

- Swells: Swells are generated by gravity and are predictable. Swells are the product of wind sea waves leaving the generation area, where they form long, regular crested waves. Swells are relatively high in energy.

- Wind sea: Wind sea waves are generated by the wind and are unpredictable and quite random since they are not fully developed yet. As mentioned before, if wind sea waves leave the generation area, they become swells.

- Capillary waves: Capillary waves are waves caused by surface tension. The period is quite small, as is the energy present in the waves.
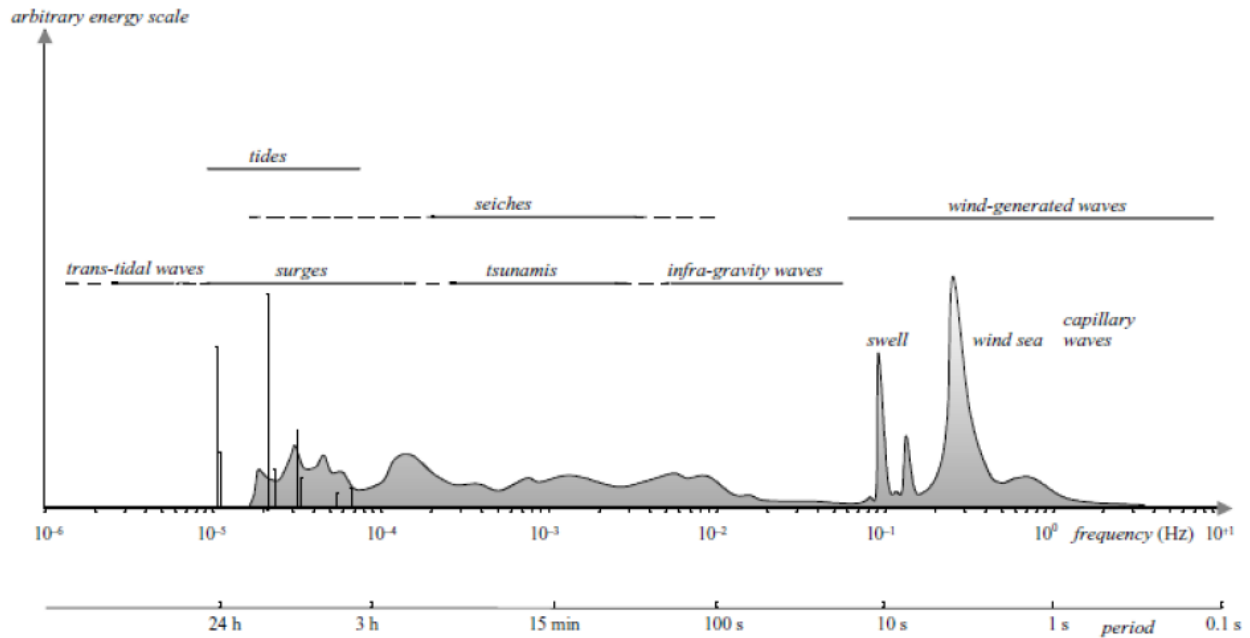
Figure 16: Frequencies and periods for different ocean waves [31].

The most important waves are swells, generated by wind. The energy content of these waves is high, which implies that there is a lot of energy available to be harvested. The waves are predictable and reliable. As mentioned, swells are developed wind sea waves and are therefore less random and easier to predict. For wave energy conversion, swells are ideal due to their predictability and mostly due to their high energy density.

3.5 Regular vs Irregular waves

There is a key difference between regular and irregular waves. Regular waves have the same period and wave height for each wave, whereas irregular waves have different periods and/or different wave heights. In Figure 17, the difference between regular and irregular waves is presented. In this specific case, the final combined wave is a product of different regular waves.
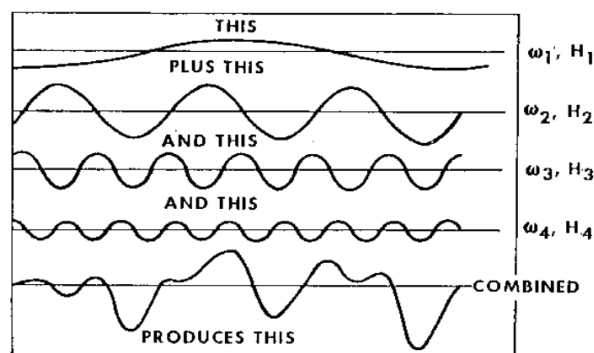
Figure 17: Creation of irregular waves [31].

In ocean waves, different waves are present, as discussed in the previous section. These waves form a 'final' wave by superposition. Since there are a lot of different waves present, ocean waves are highly irregular. Highly irregular implies that the wave periods and wave height are highly diverse.

3.6   Linear wave theory

Linear wave theory, also known as Airy wave theory, is a set of equations to describe the wave and its movement. For this research, linear wave theory is used to determine the properties of the wave. There are four main assumptions relating to linear wave theory, listed below [31]:

1. The fluid is incompressible.

2. The fluid has a constant density.

3. The fluid is ideal or inviscid.

4. The body of water must be continuous.

In ocean waves, the fluid is incompressible, since there are no extreme forces/pressures to compress the fluid. The density of the fluid must be constant as well, which is the case for oceanic waters. There can be a difference in the density of the water due to a different composition (salt vs sweet water), although this does not happen locally [31]. Another reason for different densities is temperature. The viscosity of the fluid is also assumed to be negligible. Therefore, linear wave theory applies to modeling of the Ocean Grazer.

3.6.1   Coastal waters versus Oceanic waters

There is a large difference between oceanic and coastal waters in linear wave theory. For oceanic waters, it is assumed that the depth of the water is deep enough to have no impact on wave formation and propagation. Waves are categorized as deep-water waves when the total depth is at least half of the wavelength.

$$\begin{cases} d \geq 0.5 \text{ L} & \text{deep-water (Oceanic)} \\ d < 0.5L & \text{shallow water (Coastal)} \end{cases}$$ (2)(3)

Since the Ocean Grazer will be located in deep-water, it is important to ensure that the depth is larger than half the wavelength.

3.6.2   Velocity potential function

To map the movement of waves using linear wave theory, the velocity potential is used. The velocity potential is a scalar function that represents the particle velocities. An important assumption is that that the particles are irrotational. The main cause for rotation is vorticity. For a deepwater case, the vorticity is only generated due to the slip near the bottom of the ocean and therefore has little impact. Since linear wave theory is mainly used to describe the movement near the surface, it is assumed that the particles are irrotational. The velocity potential function and its derivation are presented below.

$$\phi(x, y, z, t)$$ (4)

The velocity potential function is defined in three dimensions, where the velocity is found by the partial of the potential divided by the partial of the direction.

$$u_x = \frac{\partial \phi}{\partial x}, u_y = \frac{\partial \phi}{\partial y}, u_z = \frac{\partial \phi}{\partial z}$$ (5)

The velocity potential can then be plugged into the continuity equation. The continuity equation is derived from the mass balance:

$$\frac{\partial \rho}{\partial t} + \frac{\partial \rho u_x}{\partial x} + \frac{\partial \rho u_y}{\partial y} + \frac{\partial \rho u_z}{\partial z} = S_p$$ (6)

where the density is constant, which is one of the assumptions made. The total production should be zero since the mass should remain equal. The final continuity equation for linear wave theory is:

$$\frac{\partial \rho u_x}{\partial x} + \frac{\partial \rho u_y}{\partial y} + \frac{\partial \rho u_z}{\partial z} = 0$$ (7)

With regard to the momentum balance, it is found that the momentum per direction over time is defined by the density of the fluid and the pressure over the distance, which represents the pressure gradient.

$$\frac{\partial u_x}{\partial t} = \frac{-1}{\rho} \frac{\partial p}{\partial x} \tag{8}$$

$$\frac{\partial u_y}{\partial t} = \frac{-1}{\rho} \frac{\partial p}{\partial y} \tag{9}$$

$$\frac{\partial u_z}{\partial t} = \frac{-1}{\rho} \frac{\partial p}{\partial z} \tag{10}$$

As for the mass balance, one can plug the velocity potential function into the momentum balance and obtain the following momentum balance for the velocity potential. The velocity of the particle is replaced with the velocity function.

$$\frac{\partial}{\partial x} \left(\frac{\partial \phi}{\partial t} + \frac{p}{\rho} \right) = 0 \tag{11}$$

$$\frac{\partial}{\partial x} \left(\frac{\partial \phi}{\partial t} + \frac{p}{\rho} \right) = 0 \tag{12}$$

$$\frac{\partial}{\partial x} \left(\frac{\partial \phi}{\partial t} + \frac{p}{\rho} \right) = 0 \tag{13}$$

The gravitational term can also be added to the function.

$$g = \begin{bmatrix} 0 \\ 0 \\ 9.81 \end{bmatrix} \tag{14}$$

Therefore, the general equation for the momentum is:

$$\frac{\partial \phi}{\partial t} + \frac{p}{\rho} + gz = 0 \tag{15}$$

Finally, the boundary conditions will be applied to velocity potential. To ensure that the bottom is non-penetrable, the velocity potential for the z coordinate at the bottom (z = -d), should be zero.

$$\frac{\partial \phi}{\partial z} = 0 \quad \text{for} \quad z = -d \tag{16}$$

Near the surface, the water should not be able to leave the surface, implying the following boundary condition:

$$\frac{\partial \phi}{\partial z} = \frac{\partial \eta}{\partial t} \quad \text{for} \quad z = 0 \tag{17}$$

Besides the kinematics that describe the movement and the energy, there is a dynamic boundary as well, that deals with the pressure. The pressure near the surface (z = surface elevation (η)) should be 0, due to the interface present.

$$\frac{\partial \phi}{\partial t} + g\eta = 0 \quad \text{for} \quad z = 0 \tag{18}$$

3.6.3 Propagation of harmonic waves

As waves have a period and amplitude, their behavior is best described with a sine wave.

$$\eta(x,t) = Asin(\omega t - kx) \tag{19}$$

The time dependent surface elevation, η, is determined by the following factors: a, ω and k, which represent amplitude, frequency and the wavenumber respectively. The wave number represent the number of cycles per unit distance. t represents the time and x the coordinate. Another important factor is the forward speed, c, which is the speed of the propagation of the wave, determined by the wavelength over the period, resulting in a velocity.

$$c = \frac{\omega}{k} \tag{20}$$

3.6.4 Particle velocity and motion

An important aspect of linear wave theory is the motion of the particles in the wave. The particles move in an orbital motion, where the orbital motion of the particles is as big as the amplitude of the wave. With an increase in depth, the orbit of the particles decreases. For deep-water, the orbital motion is negligible when the depth is more than half the wavelength.
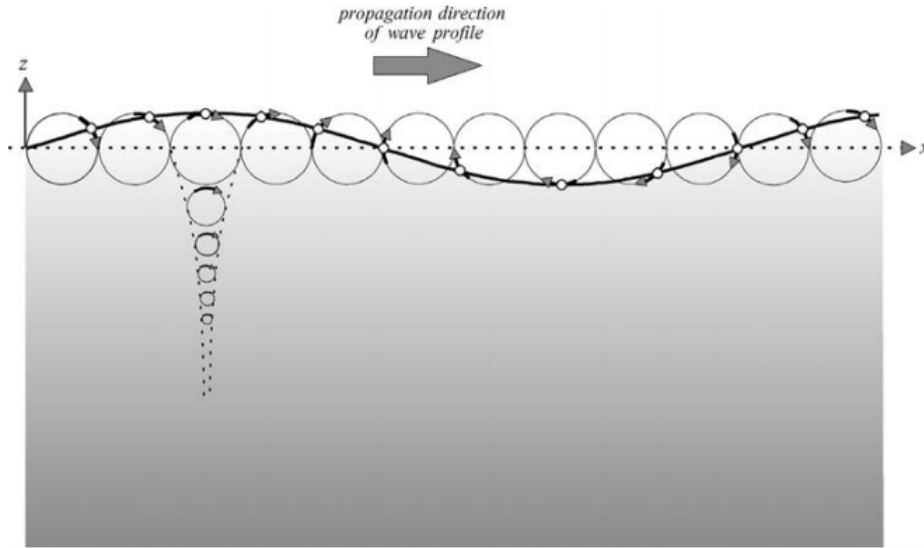
Figure 18: Orbital motion of water particles [31].

The velocity of the wave in is found with the following equation:

$$u_x = \omega A \frac{cosh[k(d + z)]}{sinh(kd)} * sin(\omega t - kx) \tag{21}$$

The term $\omega a \frac{cosh[k(d+z)]}{sinh(kd)}$ is an extra term added to model to the amplitude of the velocity potential 19. There is a difference in amplitude of the orbital motion for deep or shallow water. For deep-water, the amplitude is found by:

$$\hat{u}_x = \omega A e^{kz}, \hat{u}_y = \omega A e^{kz} \tag{22}$$

The amplitudes of the velocity components are equal for the x and y direction, since the motion is circular. The wave-induced velocities decrease with an increase in the depth of the investigated point. For z = 0, the term e^{kz} reduces to 1, where the amplitude is the velocity amplitude. This also implies that

more energy is available in the top layer, where the orbital motion is at its maximum. One of the main reasons why floating WECs outperform submerged WECs is due to the relation with energy available per depth.

For shallow water, the equations are quite different, because the seabed affects the wave. For shallow water, the motion is not orbital but more elliptical, due to the effects of the seabed.
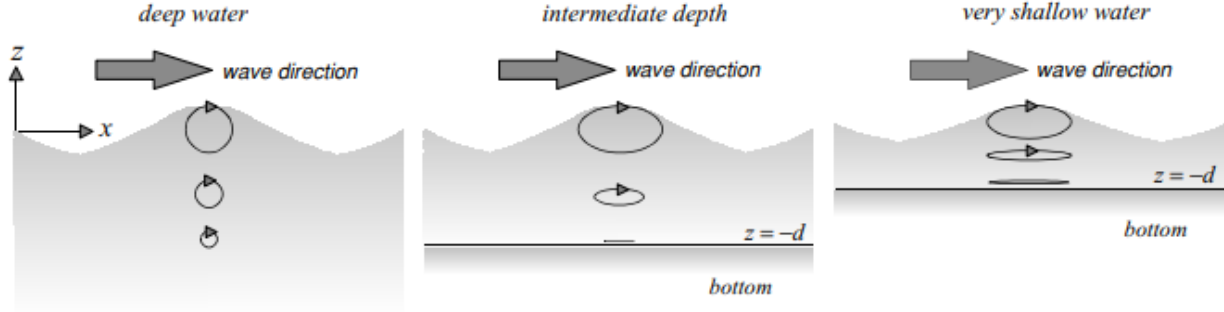
Figure 19: The orbital motion of the particles under different depths [31].

The criterion for shallow water conditions is that kd approaches 0. This is caused by a shallow depth or a small wavenumber, which implies that there are fewer cycles per unit distance. For the shallow water amplitude, it is found that:

$$\hat{u}_x = \frac{\omega A}{kd}, \hat{u}_y = \omega A(1 + \frac{z}{d})$$
(23)

Please note that the equations only represent the amplitude and not the full wave motion. For this research, the condition should be deep-sea and therefore the particle motion should be circular.

3.6.5   Particle path

Besides the particle motion and the particle velocity, the path is important as well. The path is identified from a chosen coordinate, that will be denoted by $\bar{x}$ and $\bar{z}$. The local coordinates of the field will be described with x' and z'. The equation for the particle's path is found by:

$$x' = -A\frac{cosh[k(d + \bar{z})]}{sinh(kd)}cos(\omega t - k\bar{x})$$
(24)

$$z' = -A\frac{cosh[k(d + \bar{z})]}{sinh(kd)}sin(\omega t - k\bar{x})$$
(25)

3.6.6   Dispersion

Dispersion is the separation of waves due to different velocities. The main reason for this separation of the waves is due to the different wavelengths, where longer waves travel faster and therefore depart from the shorter waves. Linear wave theory assumes that the wave is a free wave. A free wave is a wave that is only affected by gravity. To comply with this assumption, the pressure of the air-water interface must be zero. As mentioned before, the dynamic pressure boundary is set to:

$$\frac{\partial \phi}{\partial t} + g\eta = 0.$$
(26)

This boundary condition can then be applied to the harmonic wave equation and velocity potential function, to obtain an expression for the frequency of the wave and the wavelength.

$$\omega = \sqrt{gktanh(kd)}$$
(27)

24

$$L = \frac{gT^2}{2\pi} tanh(\frac{2\pi d}{L}) \tag{28}$$

This relation is called the dispersion relation. As mentioned before, the expression is different for deep or shallow waters. For deep-water, the frequency and the wavenumber are as stated above. For shallow waters, the equations are:

$$\omega = k\sqrt{gd} \tag{29}$$

$$L = T\sqrt{gd}. \tag{30}$$

3.6.7   Phase velocity

Due to dispersion, the phase velocity changes. The phase velocity, in general, is stated as $c = \omega/k$. The phase velocity is now written differently, due to the assumption that the wave is a free wave. The frequency and the wavenumber from the dispersion are plugged into the general phase velocity equation.

$$c = \frac{g}{\omega} tanh(kd) \tag{31}$$

This equation refers to any situation

$$\begin{cases} c = \sqrt{\dfrac{g}{k_0}} & \text{deep-water} \tag{32} \\[2ex] c = \sqrt{gd} & \text{shallow water} \tag{33} \end{cases}$$

where the main interaction for deep-water is dependent on the wavenumber, the main interaction for shallow waters depends on the depth of the water column considered. Since the waves for shallow depths are independent of the wavenumber, there is no difference in the velocity of the different waves; therefore, the waves are non-dispersive. For deep waters, the phase velocity differs for different wavenumbers and therefore dispersion will occur due to different wave phase velocities. Group velocity is also discussed shortly since the fluid-body interaction causes radiated waves. The total surface elevation for group velocities is determined by the sum of the surface elevations of both waves.

$$\eta = \eta_1 + \eta_2 \tag{34}$$

The formation of the waves is also highly dependent on the frequency and the phase of the wave. If the two waves have the same phase, the waves will reinforce each other. On the other hand, if the waves are out of phase, the waves diminish each other.

3.6.8   Wave-induced pressure

The velocity potential of the particles is induced by the pressure of the water. There is an analytical solution with regard to the pressure:

$$p = -pgz + pgA\frac{cosh[k(d+z)]}{cosh(kd)}sin(\omega t - kx) \tag{35}$$

The first term represents the hydrostatic pressure. The second term relates to wave-induced pressure. The pressure that is influenced by the wave is therefore called wave-induced pressure. For deep and shallow water, the wave-induced pressure is found by:

$$\begin{cases} p_{wave} = \rho gAe^{kz} & \text{deep-water} \tag{36} \\ p_{wave} = \rho gA & \text{shallow water} \tag{37} \end{cases}$$

3.6.9   Wave energy

One of the important aspects of this research is the energy present in the wave. For waves, there is both elevation and velocity, therefore both potential and kinetic energy are available. The potential energy is generated by the storage of particles due to elevation opposite to gravity. Kinematic energy is obtained due to the displacement, caused by velocities. In general, the potential and kinematic energy are:

$$E_{kin} = \frac{1}{2}mv^2 \tag{38}$$

$$E_{pot} = mgh \tag{39}$$

For waves, the potential energy is found with the integral over the wave, calculating the total elevation of the area.

$$E_{pot} = \int_0^\eta pgz\,dz \tag{40}$$

Since the wave's motion is constant and predictable, an average of the potential energy can be determined by:

$$E_{pot} = \frac{1}{4}\rho g A^2 \tag{41}$$

The kinematic energy in a wave is determined by the velocity of the particles. Since the kinematic energy is not only determined by the motion of the upper orbital movement, the whole depth must be considered.

$$E_{kin} = \int_{-d}^\eta \frac{1}{2}\rho u^2\,dz \tag{42}$$

As mentioned before, an average can be found by

$$E_{kin} = \frac{1}{4}\rho g A^2 \tag{43}$$

When only considering the top of the wave in deep-water, the total energy available is the sum of the potential and the kinematic energy. The kinetic and potential energy parts are equal for regular waves since the number of elevated particles should be equal to the incoming velocity of the particles.

$$E = \frac{1}{2}\rho g A^2 \tag{44}$$

3.6.10   Wave energy transport

The energy flux of waves is discussed briefly in this section. The energy transported is found by the energy in the area and its displacement. The energy contained is multiplied by the time step and the displacement in the y direction. The potential and kinematic energy flux is found by:

$$f_1 = \left(\int_{-d}^\eta (\rho g z)\,u_x dz\right)\Delta y\,\Delta t \tag{45}$$

$$f_2 = \left(\int_{-d}^\eta (\frac{1}{2}\rho u^2)\,u_x dz\right)\Delta y\,\Delta t \tag{46}$$

Besides potential and kinetic energy transport, there is also another type of energy that is transported, in the form of pressure. The pressure is transported in the direction of wave propagation.

$$f_3 = \left(\int_{-d}^\eta \rho\,u_x dz\right)\Delta y\,\Delta t \tag{47}$$

As mentioned before, the pressure is split into the hydrostatic pressure and the pressure of the wave, which can can be used to expand equation 48 to:

$$f_3 = \left(\int_{-d}^{\eta} -\rho g z_{pwave} \, u_x dz \right) \Delta y \, \Delta t \tag{48}$$

The total transport of energy is the sum of all parts f_1, f_2 and f_3.

3.7 Hydrodynamics of offshore devices

In this chapter, the hydrodynamics for off-shore devices are discussed. Besides translational movements in the x, y and z directions, named surge, sway and heave respectively there is also rotational movement. As with the translational movements, they are defined for each direction of the plane, which is for the x, y and z-direction roll, pitch and yaw, respectively.
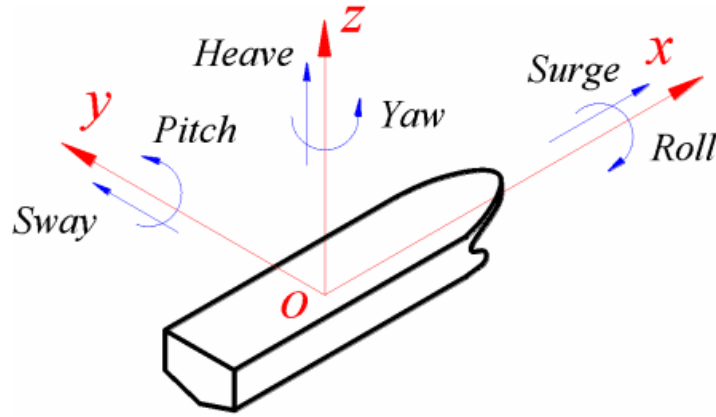
Figure 20: Translational and rotational movements of a rigid body [32].

The general equation of motion for a rigid body in a fluid is:

$$\ddot{X} = F_T(t) + F_{ext}(X, \dot{X}, t) \tag{49}$$

From the equation, one can see that the mass and acceleration of the body are dependent on wave-induced and external forces. The motion of the body is determined by the wave and the extraction of the power, in a specific case for power extraction of WECs. The WEC is not only a floating body, dominated by fluid-induced pressures, but also an energy extractor, which has some resistance to the PTO mechanism.

3.7.1 Fluid forces on a floating object

In this section, the fluid forces on a floating object are explained. The fluid forces are split into three different components, as follows:

$$F_f(t) = F_S(t) + F_R(t) + F_H(t) \tag{50}$$

Where $F_S(t)$ is the excitation force, $F_R(t)$ is the radiation force and $F_H(t)$ is the hydrostatic force.

$F_S(t)$, the excitation force is the force on the body if it is held into place. The excitation force can be split up into the effect of the diffracted and incident waves. The effect of the incident wave is caused by the pressure applied on the rigid body from the incident wave. Diffraction is the effect of the diffracted wave on the body.

$F_R(t)$, the radiation force is the force of a moving body on the fluid. This implies that radiated force can also be present in a fluid without waves if the body moves. The radiation force consists of two components,

relating to the body's velocity and acceleration. Concerning the body's acceleration, the force is found with the product of the added mass and acceleration. The velocity force is found using the velocity and damping coefficient.

$$F_R(t) = -(A(\omega)\ddot{X} + B(\omega)\dot{X}) \tag{51}$$

The acceleration of the body is related to the added mass, A, and the velocity is related to the damping coefficient, B.

The added mass coefficients and the radiation resistance (damping coefficient) have an impact on the energy extraction. The radiation resistance is directly linked to the power extraction, which is discussed in Section 3.8.1. The radiation resistance and the added mass can be tuned using the wave properties.

$F_H(t)$, the hydrostatic force, is the buoyancy force of the body.

$$F_H(t) = -\rho g V \tag{52}$$

where ρ is the density of the fluid and V is the displaced fluid volume. The hydrostatic force is the net force of the buoyancy and the gravity, where, for a positive value, the object floats, and for a negative value, the object sinks.

3.8   Equations of motion including PTO

With the fluid interactions known, the full equations of motion can be formulated, where the external forces are included. The external forces in this case are related directly to the extraction of energy. The full equations of motion can be found by adding the fluid-induced forces 50 to the full equation discussed before in 49.

$$m\ddot{X} = F_s(t) + F_R(t) + F_H(t) + F_{Ext}(X, \dot{X}, t) \tag{53}$$

Using the formula above, a more in-depth view of the motion and its interactions is found below:

$$(m + A)\ddot{X} + B\dot{X} + CX = F_S + F_{ext}(X, \dot{X}, t) \tag{54}$$

Note that from 54, the motion of the object is dependent on the excitation force of the incident wave and the extraction of energy. The excitation force causes the heave of the floater and the extraction of energy is caused by the resistance of the damper. The radiation forces are important to keep into account as well, especially if an array consists of multiple floaters.

Note that the equations of motion as mentioned before can also be interpreted as a potential function [33]. For example, the fluid forces on an object can also be written as:

$$\phi = \phi_0 + \phi_d + \phi_r \tag{55}$$

where ϕ is the overall potential function of the hydrodynamics, ϕ_0 is the potential of the incident wave, ϕ_d is the potential of the diffraction of the incident wave and ϕ_r is the velocity potential of the radiated wave.

3.8.1   Energy extraction by PTO

The energy extracted from a PTO is calculated using the following formula:

$$P = \frac{1}{2} B_{PTO} \omega^2 \Delta y^2 \tag{56}$$

Where ω represents the angular velocity, Δy the heave of the floater, and B_{PTO} the damping coefficient of the system.

In this study, the frequency of the waves is equal and therefore constant. This implies that the damping coefficient and the displacement in heave determine the power generated. In the final chapter, the damping coefficient is also constant, which implies that the displacement in heave solely determines the performance of the floater.

3.9 Operators in CFD

The most important operators in CFD are the divergence and gradient. The gradient (Equation 57) is a vector describing the direction of the expansion of the field. This also indicates the direction of the fluid, when pushed away by some floating object. The divergence (Equation 58) is a scalar value, representing the volume density of the outward flux. The gradient and the divergence indicate the direction and the velocity of the flow and therefore are crucial operators in CFD. Besides the gradient and the divergence, the curl indicates the rotation of the field. The curl is basically a collection of gradients for different positions, to find the direction of the rotation.

$$\nabla s = \left[\frac{\delta s}{\delta x} \frac{\delta s}{\delta y} \frac{\delta s}{\delta z} \right] \tag{57}$$

The gradient represents the slope of a plane. This implies that for higher values, the inclination angle is steeper.

$$\nabla \cdot v = \left[\frac{\delta v_x}{\delta x} \frac{\delta v_y}{\delta y} \frac{\delta v_z}{\delta z} \right] \tag{58}$$

For positive divergence values, more fluid is 'extracted' from a point, or leaves a point (source). For negative values, more fluid is 'gained' at a certain point, as the fluid goes towards a point (sink).

$$\nabla \times v = \left[\frac{\delta v_z}{\delta y} - \frac{\delta v_y}{\delta z} \frac{\delta v_x}{\delta z} - \frac{\delta v_z}{\delta x} \frac{\delta v_y}{\delta x} - \frac{\delta v_x}{\delta y} \right] \tag{59}$$

The Laplacian operator (Equation 60 is a combination of the gradient and the divergence. The Laplacian represents the divergence of the gradient. The Laplacian represents the maxima and minima of the potential.

$$\Delta = \nabla \cdot \nabla = \nabla^2 \tag{60}$$

3.9.1 Transport of fluids

In this section, the transport of fluid is discussed briefly.

Advection Advection is the transport of a substance by bulk. An example is air pollution due to the combustion of fuels in a power station. This implies that the transport of the fluid is quite uniform. The equation is presented below:

$$\frac{ds}{dt} = -v \cdot \nabla s \tag{61}$$

where s represents any property, for example, a concentration or temperature. In the formula, one can see that the transport over time is defined by the velocity.

Diffusion Diffusion is another transport system. Diffusion is the transport of particles to obtain a uniform solution. An example is a droplet of ink in a glass of water, where the droplet will start to diffuse in the water and spread in the fluid equally.

$$\frac{ds}{dt} = k\nabla^2 s \tag{62}$$

In the formula, one can see that the transport over time is influenced by the rate of diffusion (k) and the Laplacian of the scalar field. The Laplacian represents the 'hotspots' of the material to be diffused.

Pressure gradient   The pressure gradient is the driving force of fluid flows. Fluid tends to flow to the place with the lowest pressure, to create a uniform pressure field. The pressure in the field is determined by a lot of parameters, where the area is an important factor. In the Bernoulli theorem, one can see that the pressure is related to the area and the velocity of the fluid. The Bernoulli equation is presented below:

$$P_1 + \frac{1}{2}\rho v^2 + \rho g h = constant. \tag{63}$$

The theorem describes the relationship between pressure and velocity, where an increase in pressure implies a decrease in velocity and vice versa.

3.10   Navier-Stokes equations

The Navier-Stokes equations (Equation 64) are an important aspect of CFD simulations. The Navier Stokes equation represents the conservation of mass, energy and momentum in a fluid. These equations are a combination of multiple equations. The complete Navier-Stokes equations cover many aspects of fluid flow but are in most cases too complex to solve, due to computational time. To reduce the computational time, different aspects that are deemed less important can be excluded from the equations. The Navier-Stokes equation can be found below.

$$\frac{d\mathbf{v}}{dt} = -\mathbf{v} \cdot \nabla \mathbf{v} + \mu \nabla^2 \mathbf{v} - \nabla p \tag{64}$$

COMSOL uses the Navier-Stokes equations to calculate the flow of fluid, in a simplified form.

3.10.1   Compressibility

One of the main assumptions in the Navier Stokes equations is the compressibility of the fluid. In most low pressure systems the fluid is incompressible. This constrain will have a low impact for the simulations to be conducted in this research, since there is no tendency for the fluid to compress.

3.11   Creation and selection of waves

In this chapter, the selection of wave parameters is discussed. As mentioned before, a real-time ocean wave will be used for the simulations. Secondly, wavemaker theory and some practical issues with wavemakers in CFD environments are discussed.

3.11.1   Wave parameter selection

Since the model gives the freedom to create a large spectrum of waves, parameters have to be selected for the wave in the simulations. The parameters of the wave are based on a probability matrix of real wave data, namely the data from the Bay of Biscay, located near the western side of France. The probability matrix represents the average significant wave height and period of the wave. The average is a yearly average.
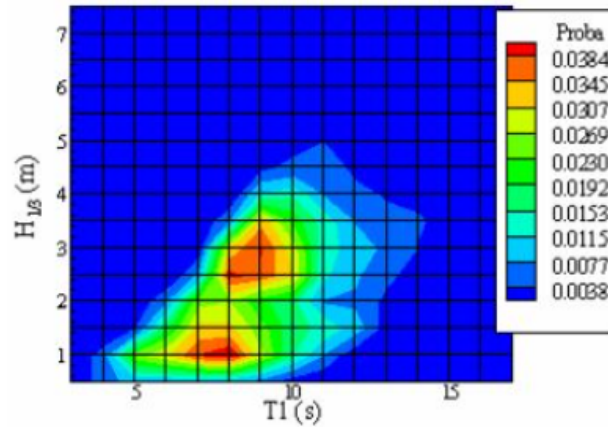
Figure 21: The probability matrix near bay of Biscay. On the horizontal axis the period is presented and on the vertical axis the significant wave height (A.Bechlenberg, 2020).

From Figure 21, one can see that there are two types of waves that have the highest probability.

Wave height	Period
2,5 - 3 m	8-9,5 sec
1 m	7-8 sec

Table 1: Wave properties of the most probable waves at the bay of Biscay.

For this project, the selection of wave properties does not have to be very exact. The main reason for this is because the main focus of the research lies on the WEC properties and behavior. From previous research on the Ocean Grazer, comparable parameters have been used. The main issue is that, in the current study, regular waves are generated and most previous studies use irregular waves.

3.11.2 Wavemaker theory

Different types of wavemakers can be considered for simulations. The first type is a piston wavemaker, which has horizontal movement only. The second type, a flap wavemaker has rotational movement. A combination of both systems also exists. Besides the motion of the wavemaker, the positions of the wavemaker can also be changed, to be closer or further away from the lower boundary.
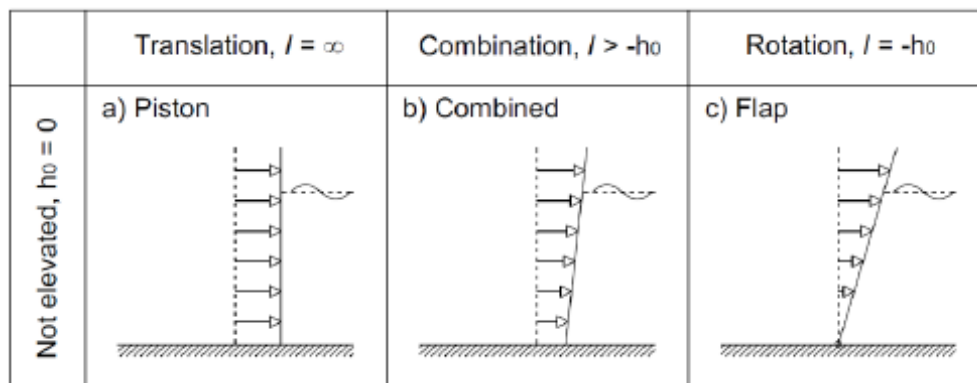
Figure 22: Different types of wavemakers [34].

A flap type wavemaker, moving with a certain rotation is the best to simulate deep-water ocean waves, whereas a piston type is the better choice when considering shallow water [35]. Since the waves in this study

are deep-water waves, a flap type wave generator will generate more realistic waves. In the Figure 23 one can see that the piston type wavemaker produces shallow-water waves, whereas the particle motion is more elliptical. For the flap type, the particle motion is more circular, which represents deep-water waves. This is caused by the movement of the flap type wavemaker, where the displacement varies with the height of the wavemaker due to the rotational motion. This results in larger movements near the surface. The larger movements create larger velocities and therefore larger circular motions near the surface. With an increase in depth, the velocity is smaller which is in line with deep-water waves.
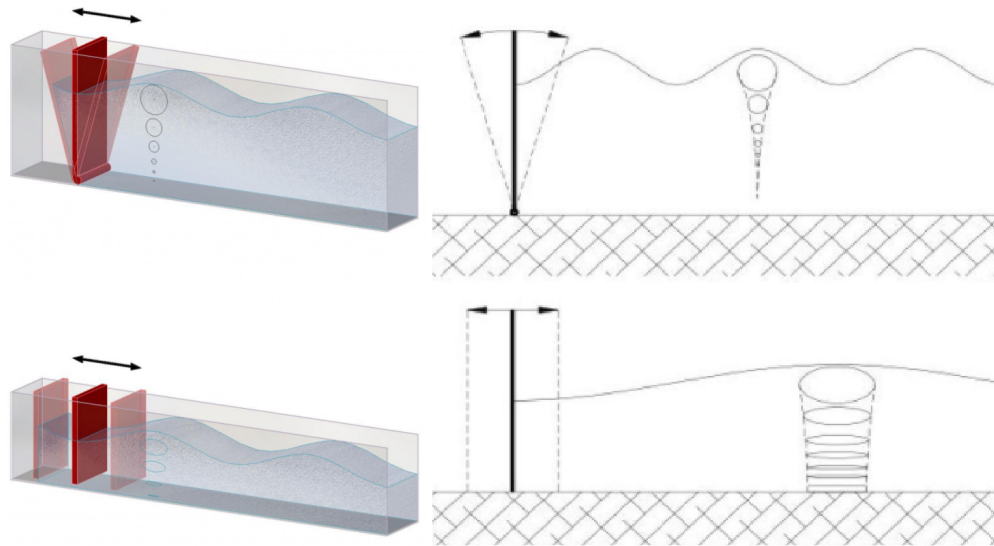
Figure 23: The two types of wavemakers suitable for this research, on the left the flap type wavemaker and on the right the piston type wavemaker [34].

Since the Ocean Grazer is placed in deep waters, the flap type wavemaker is the best option. In Section 5.1, a test is conducted to obtain insight and validate the particle motion for a piston and flap wavemaker in COMSOL.

3.11.3 Wave creation in CFD environments

As mentioned before, the wavelength of ocean waves is quite long, because of long periods. The wavelength is independent of the amplitude. The most frequent waves from the probability matrix have a rather long period, with small amplitudes. A factor, let's call it Q_{wave}, is introduced to investigate the relation between the wave height and the wavelength.

$$Q_{wave} = \frac{Waveheight(H)}{Wavelength(\lambda)} \tag{65}$$

For example, a wave with a low Q_{wave}, where the wave height is small compared to the wavelength, is harder to create compared to a wave with a high Q_{wave}. The main reason for this has to do with the motion of the wavemaker. The speed of the motion of the wavemaker is dependent on both the amplitude and the frequency of the wavemaker, due to the sine wave used to define its movement. With a low amplitude and low frequency, the wavemaker moves slowly. For a low velocity, a low amount of energy is transferred to the wave. If too low, waves are not created, but the fluid is moved without an increase in surface elevation. This effect can be thought of as moving water with an object: if the object is moved slowly, no waves are created but the fluid flows around the object. Gravity makes the situation even worse, where the 'wave' that is created disappears rapidly and does not propagate. The main problem here is that in the simulated domain there is no initial velocity of the fluid. Therefore the waves have too much shear resistance since the kinetic energy is low due to the slow moving flap. Due to the resistance and gravity, waves are not created. It is

therefore not possible to simulate waves with a too low Q_{wave}. Below, Q_{wave} for the most frequent waves near the Bay of Biscay are presented.

Q_{wave}	Period	Amplitude	Q_{wave}
Wave 1	8-9,5 sec	2,5-3 m	0.263-0.375
Wave 2	7-8 sec	1 m	0.125-0.143

Table 2: Q_{wave} for both waves.

Because of this, the decision is made to only use the first wave from Table 2, because Q_{wave} is a lot higher compared to the second wave.

3.11.4 Wave scaling

For a wave in a CFD environment, the domain needs certain dimensions. The main reason is reflection, caused by the outer boundaries of the domain. The most important dimension is the length of the domain. To simulate waves with little reflection, the domain has to be at least three/four times as long as the wave. For the wave that is selected in the previous chapter, the wavelength is very long, resulting in a very large domain. This results in a very long computational time.

To reduce the domain size, the wave is scaled down. To scale the waves Froude's number is used. Froude's number is a dimensionless value that represents the different flow regimes in an open channel. Froude's number is a ratio of the inertial and gravitational forces. To properly scale waves, Froude's number should remain constant.

$$Fr = \frac{V}{\sqrt{gD}} \tag{66}$$

where V is the velocity of the fluid, g represents the gravity and D is the hydraulic depth. The hydraulic depth is found with the cross-sectional area divided by the top width. Since the simulations are in 2D, the hydraulic depth is constant since there is no top width, therefore D is any dimension used to scale the waves. V, the velocity of the waves, is calculated with the propagation speed of the waves [36]. Since Froude's number should be constant, the following equation is used to scale the waves properly.

$$\frac{V_f}{\sqrt{g_f D_f}} = \frac{V_S}{\sqrt{g_S D_S}} \tag{67}$$

where subscript f implies full-scale, or the original wave in this case, and S the scaled wave. For the scaling of the amplitude, the velocity is the same, since the velocity is determined as the propagation speed of the wave. Therefore, the amplitude of the wave scales one to one. For example, if the wave is scaled down by a factor 2, the scaled amplitude is half the original amplitude. For an equal frequency, $V_f = V_S$, $D_f = 2D_S$ and the gravity remains equal as well. A_f and A_S represent the amplitudes.

$$\frac{V_f}{\sqrt{g_f D_f A_f}} = \frac{V_S}{\sqrt{g_S D_S A_S}} \tag{68}$$

$$\frac{1}{\sqrt{g_f D_f A_f}} = \frac{1}{\sqrt{g_S D_S A_S}} \tag{69}$$

$$\frac{1}{\sqrt{\frac{1}{2} g_f A_f}} = \frac{1}{\sqrt{g_S A_S}} \tag{70}$$

resulting in,

$$A_f = 2A_S \tag{71}$$

On the other hand, the frequency does change the velocity of the fluid and is therefore scaled with the speed of the fluid. As with the example above, the wave is scaled by a factor 2. The gravity is a constant and $D_f = 2D_S$.

$$\frac{V_f}{\sqrt{D_f}} = \frac{V_S}{\sqrt{D_S}} \tag{72}$$

$$\frac{V_f}{\sqrt{\frac{1}{2}}} = V_S \tag{73}$$

Resulting in,

$$V_f = \sqrt{\frac{1}{2}}V_S \tag{74}$$

$$\sqrt{2}V_F = V_S \tag{75}$$

For a higher velocity, the frequency is higher and therefore the period is shorter.
In the table below, the amplitude and period for different scaling can be found.

Scaling factor	Period	Amplitude
1:1	9 sec	3 m
1:2	6.3 sec	1.5 m
1:3	5.1 sec	1 m
1:4	4.5 sec	0.75 m
1:5	4	0.6 m

Table 3: The parameters for different scaling values.

Besides Froude's number, Froude's scaling factors are also using in later chapters. Froude's scaling factors determine the scaling effect using the units of a parameter. The Froude's scaling factor table is presented in appendix A.

4   Model Description

In this chapter, the model is described. The full model can be found in Appendix C.

4.1   Geometry and materials

The geometry of the domain is quite simple. The domain consists of four outer walls to ensure that the fluid does not leave the domain. The domain is vertically split into two different domains that represent water and air respectively. The wavemaker is placed near the left side boundary, to minimize the amount of wasted computational resources since the wave formation left of the wavemaker is not used. A better option would be a moving boundary instead of a wavemaker in the domain; unfortunately, this is not possible in COMSOL. The wavemaker is modeled as empty space, the boundaries of the empty space move with a certain motion, as discussed in the next section. The geometry and materials used can be found in Figure 24, Table 5 and Table 4 below.
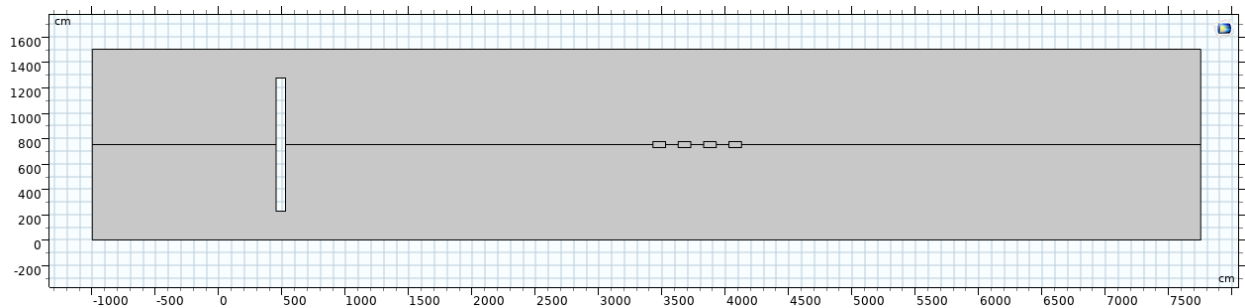
Figure 24: The geometry of the domain including the wavemaker and floaters.

Domain	Density	Dynamic viscosity
Water (15 $°C$)	1023.7 (kg/m^3)	1.1373 e-3 (Pa*s)
Air (15 $°C$)	1.2 (kg/m^3)	1.7875 e-5 (Pa*s)
Floaters	514 (kg/m^3)	N/A

Table 4: Material properties for the different domains.

	Domain	Absorption layer	Wavemaker
Length	67.5[m]	5[m] (both sides)	0.75[m]
Height	7.5[m]	7.5[m]	10.5[m]

Table 5: The dimensions of the domain, absorption layer and wavemaker

The dimensions for both the rectangular and the conical floater can be found below in Figure 25a and Figure 25b.

(a) Dimensions of the rectangular floater.

(b) Dimensions of the conical floater.
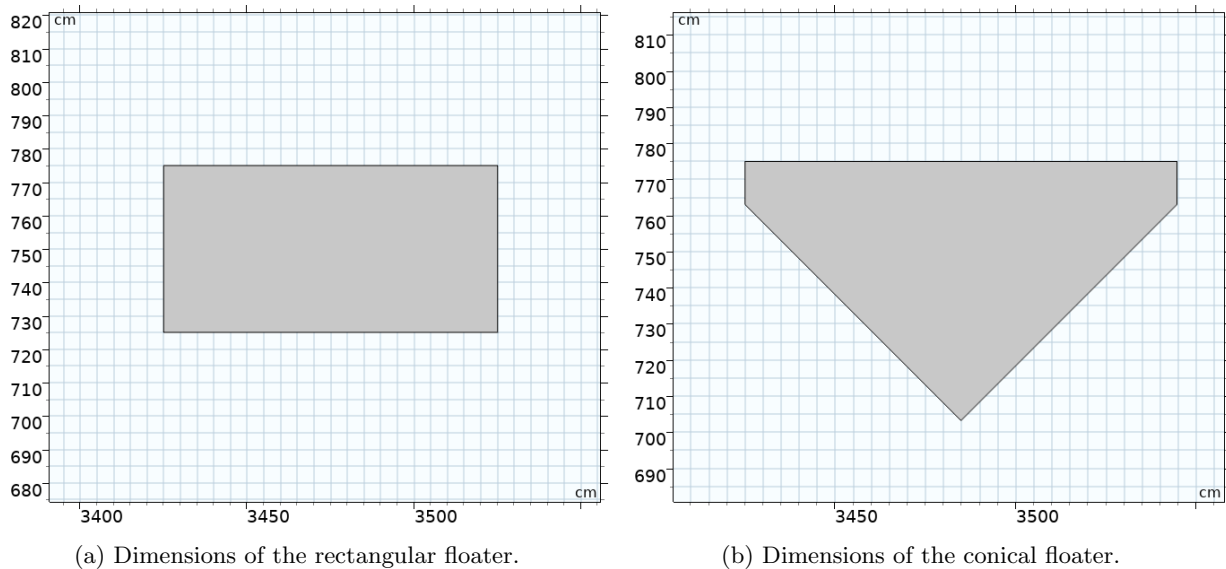
Both the water and air domains are deforming domains. This allows the domains to change their shape according to the changes during a transient study. An example is the movement of the wavemaker, which changes the geometry of the domains as well. Besides the wavemaker, the floaters should move with the interface. The floaters themselves are not deformable, since it is assumed that there are no deformations in the floaters.

4.2 Wavemaker motion

The wavemaker operates using an angle and a rotation point, r_x. r_x is set directly underneath the wavemaker, located on the lower boundary of the domain. The main reason is that in an ideal case, the wavemaker would be connected to the lower boundary, but due to the boundary conditions and constraints, this is not possible in COMSOL. The main reason for this is that the boundaries cannot 'touch' and therefore have to be separated. The angle α of the wavemaker is calculated with a sine wave, or wave function in COMSOL, which is stated below in Equation 76:

$$\alpha = A sin(\omega t + \phi) \tag{76}$$

where α is the angle of the wavemaker, A is the amplitude, ω represents the angular velocity and ϕ is the phase. The wavemaker starts its motion from the initial position to the positive direction, therefore the phase is not changed.

4.3 Pressure settings

The initial pressures of the fluids have to be determined as well. For the air domain, the pressure is equal to the absolute pressure of 1 atm. For the water, the hydrostatic pressure is determined with the following equation:

$$Hydrostatic\ Pressure = \rho g (height - y) \tag{77}$$

where ρ is the density of the fluid, g is the gravity, height is the height of the initial water column and y is the y-coordinate. The hydrostatic pressure is 0 on the interface, increasing with depth.

To validate the pressure, a plot is presented where the analytical solution is compared to the actual pressures present in the water column. As one can see in Figure 26, the pressure increases with an increase in depth. The values in the pressure points match the pressure of the fluid. Since the height of the water column is 7.5 meters, ρ is 1023.6 kg/m^3 and gravity is 9,81 m/s, the pressure on the bottom should be equal to 7.56 e^4 Pa, which corresponds to the values found in the plot.
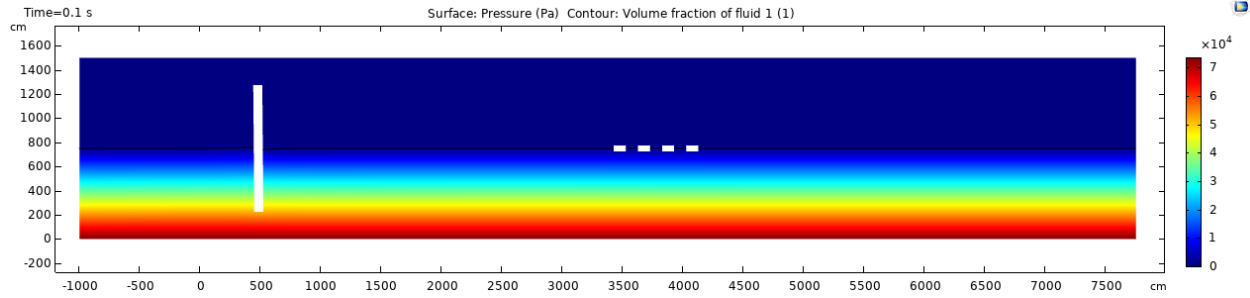
Figure 26: Pressure plot of the hydrostatic pressure in the domain. Please note that the hydrostatic pressure is plotted, which is added to the absolute pressure.

When creating waves, the hydrostatic pressure changes, since the height of the water column changes as well. This can be seen in Figure 27 below, where the hydrostatic pressure takes the same shape are the wave profile.
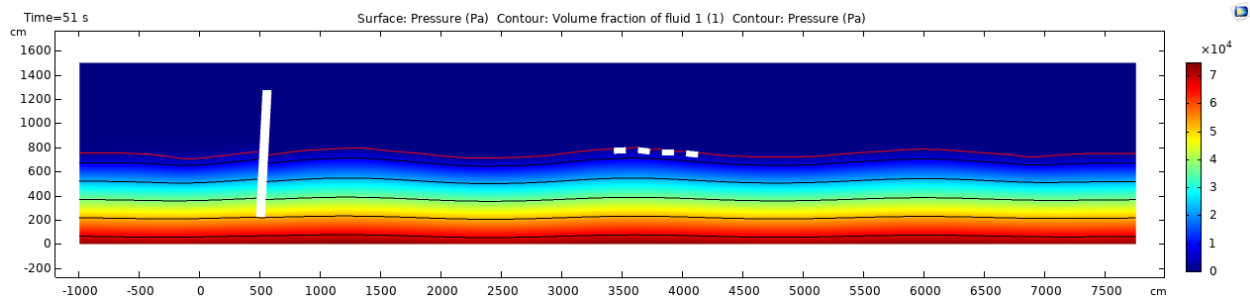
Figure 27: Pressure plot of the hydrostatic pressure in the domain during wave creation. The red line represents the interface and the black lines the pressure contour.

The fluid-induced pressures are calculated automatically.

4.3.1   Pressure point constraints

Pressure point constraints are necessary in COMSOL models to allow for convergence. The main reason for this is that the Navier Stokes equations use the derivative of the pressure. The pressure has to be defined at least at one point, to ensure that there is a solution. If there is no pressure point defined, there is an infinite amount of solutions and the simulation will not converge [37]. In the model, two pressure points are set, located on the top edges of the domain. The location and the values for the pressure point constraints are presented in Figure 28 and Table 6.
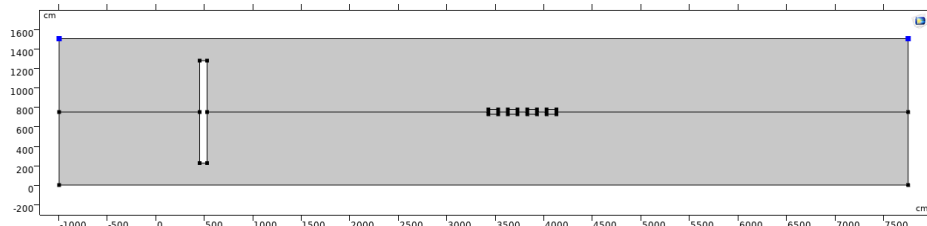
Figure 28: Pressure point constraints in the model.

Pressure point	Pressure
Pressure top right	1 [atm]
Pressure top left	1 [atm]

Table 6: Pressure constraints for the domain edges.

4.4 Wall conditions

In the model, the wall conditions have to be configurated as well. This is quite important since the walls that are present are non-physical walls since they are only used to enclose the domain and do not serve the function of a 'real' wall. In the following two sections, the wall conditions for both the flow and the phase field are discussed.

4.4.1 Walls (flow condition)

There are different settings for the wall conditions. Most relevant are the slip and no-slip conditions. No-slip implies that the velocity with respect to the boundary is 0. The physical explanation is that the adhesive forces are larger than the cohesion forces. The adhesive force is the attraction of the fluid particles to the solid particles and the cohesive force is the attraction of the fluid particles to other fluid particles. No-slip implies that the particles are stuck against the boundary, so the velocity is 0. Slip implies that the particles 'slip' amongst the wall and thus the velocity of the particles near the boundary is non-zero [38]. In Figure 29 slip vs no-slip is visualized. The slip condition assumes a no-penetration condition, where $u * n = 0$, where u represents the velocity and n the normal. Besides this, there is no boundary layer development since it is assumed that there are no viscous effects and thus a boundary layer does not develop.
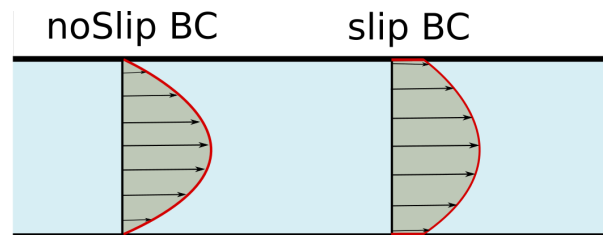
Figure 29: Slip vs no-slip condition [39].

For the outer boundaries of the domain, slip is used. Slip is the best option for non-physical walls where the development of a boundary layer is not a desirable effect, since the only function of the wall is to ensure that the fluid does not leave the domain. For the boundaries of the wavemaker, the same holds: slip is used to ensure that the particles do not 'stick' to the wavemaker, causing undesirable effects on the wave. The slip length is not defined for a slip condition in COMSOL [19].

In short, the slip condition is the best condition to model a domain that in reality is not present. The no-slip condition would be used if a real wall should be modeled [40], for example, the floaters.

4.4.2 Walls (phase field condition)

With regard to the phase field, the conditions for the wall have to be configured as well. The condition used in this case is the 'wetted wall' condition. The function of the wetted wall is to set a condition to the wall that it will be in contact with one or multiple fluids. One of the parameters that is defined is the contact angle (see Figure 30). The contact angle is set to pi/2, which is the contact angle for a water/air wall interaction [41].
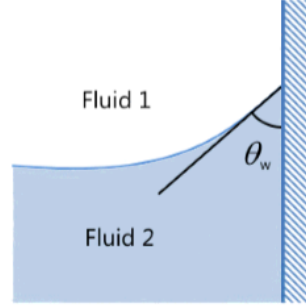
Figure 30: The contact angle in a situation with two fluids and a wall [19].

4.5 Interface tracking

The phase field and the level set method are both field-based methods, whereas the free surface is represented as an isosurface. The main difference is how the methods deal with the external forces for the velocity component of the Navier-Stokes equation, presented below:

$$\frac{\delta\phi}{\delta t} + \nabla\phi \cdot u = F \tag{78}$$

The phase field method tries to minimize the free energy of the external forces applied to the fluid. The level set method sets the external force to zero, which is why the method is not that useful for real-time simulations because of lower accuracy. Besides accuracy, the level-set implies that the physics of all the domains are the same. This is not the case for this study, since both fluid flow, phase field, and multibody dynamics are present which cannot be defined by the same physics. The phase field method is superior for this study.

The interface of the fluids can be found where the phase-fraction is 0.5. Both methods use the fractions of the fluid to calculate the combined dynamic viscosity and the combined density.

4.6 Phase field settings

An important setting in the phase field method is the interface thickness. The interface thickness is set by parameter ϵ_{pf}. The parameter is determined by the maximum mesh size surrounding the interface. For a too thin interface, the solution will not converge; however, if the interface is too thick, inaccuracies will occur. The formula is found below:

$$\epsilon_{pf} = \frac{1}{2}h_{max} \tag{79}$$

where ϵ_{pf} is the thickness in meters and h_{max} is the maximum element size near the boundary. For more information on the mesh and the size, please consult Section 4.9 and Section 5.5.2.

For the default settings, the interface is half the size of the largest element which causes instabilities with the floaters. To cope with this problem, the interface thickness was reduced until the solutions do not converge from the initial solution, where the interface thickness is set to 1/6 times the maximum element size. This produced accurate results.

The mobility tuning parameter is another parameter that deals with the interface of the two fluids by controlling the time scale of the diffusion. The mobility tuning parameter can be calculated from the velocity at the interface of the fluid.

$$\chi = \frac{Uh_{max}}{3\sqrt{2\sigma\epsilon}} \tag{80}$$

where χ represents the mobility tuning parameter, U the velocity of the fluid at the interface, h_{max} the maximum element size near the interface, σ the surface tension of the two fluids and ϵ the interface thickness.

4.7   Absorption layer

Since the wave in the model should represent real ocean waves, absorption should be included to account for the reflection of the waves caused by the domain boundaries. There are different strategies in CFD to absorb the reflection of waves. The main types are active and passive absorption. Active absorption is mostly a moving boundary, which moves with the dynamics of the waves to absorb reflection. This is quite complex and not realizable during the period of this research. A passive absorption layer was designed to absorb most of the reflection of the waves. A simple strategy is chosen, where the dynamic viscosity of the water is increased with the x-coordinate inside the absorption layer [42]. The absorption layer has a certain length and is applied to both sides of the domain. The formula for the absorption can be tuned to match the parameters of the incident wave. The main reason for this is that larger wave heights need a higher dynamic viscosity to be absorbed compared to waves with a smaller wave height since more energy is present in higher waves. The formula used for the increase in dynamic viscosity inside the absorption layer can be found below:

$$Viscosity \begin{cases} Absorption\ layer\ left & v + (\alpha \cdot 250,000 \cdot v(-X)^2) \\ Absorption\ layer\ right & v + (\alpha \cdot 250,000 \cdot v(X - X_0)^2) \\ Otherwise & v \end{cases} \tag{81}$$

where v is the dynamic viscosity of the fluid, X_0 represents the x-coordinate where the absorption layer starts and X is the current x-coordinate. α, the viscosity tuning parameter, is a factor that is used to tune the viscosity to the parameters of the incident wave. The main reason to not include the 250,000 in α is because the 250,000 is used in Martinelle's research [42]. α is used to tune the factor to the current model. To create a smoother function, the distance inside the absorption layer is squared.

An example is given below, where the dynamic viscosity is increased over the length of the absorption layer, where α equals 1 and the length of the absorption layer is 5 meters.
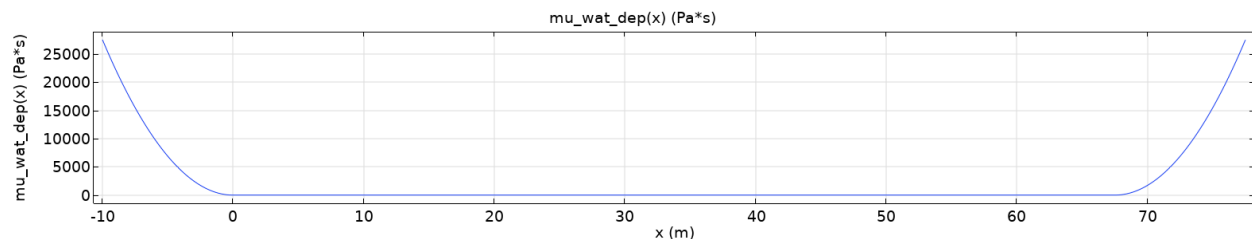
Figure 31: Plot of Equation 81 for a 67.5 meter domain, 10 meter absorption layer and $\alpha = 1$. The vertical axis represents the dynamic viscosity, the horizontal axis represents the x-coordinate.
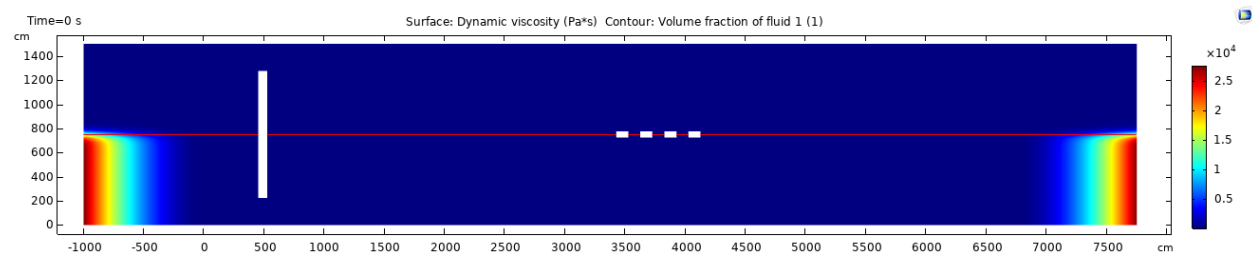
Figure 32: Figure of the dynamic viscosity in the domain.

4.8   Floaters

Modeling the floaters is quite complicated. In the real system, the floaters are connected to a rigid wind turbine or pole. Because the rigid pole is not able to move, the floaters are also not able to move too

much. Due to the complexity of this system, there are many degrees of freedom, which makes the problem difficult to solve [43]. In most studies, the floaters are fixed in surge and they are only free to move in heave. This is a big drawback since, in the real system, the floaters can move and rotate in six dimensions.

4.8.1 Fixed floater array

As mentioned before, the results will be split in a fixed floater array. In the first section, the floaters can only move in heave and are fixed in surge. In the second section, the floaters are connected, using multibody-dynamics to solve for movement and rotation.

For the fixed array, the surge of the floaters is fixed. Heave and pitch are both free. The constraints are listed below:

$$Motion\ of\ the\ floaters \begin{cases} u_{x\,floater} & 0 \\ u_{y\,floater} & free \\ \theta & free \end{cases} \tag{82}$$

Since the PTO is connected to the center of mass of the floater, pitch will occur due to the motion of the waves and is therefore important to include in the model. Heave is the main key performance indicator of the floaters and should be free. To model the fix in surge, a pre-described displacement in applied to the center of mass, where $u_x = 0$.

4.8.2 Connected floater array

For the second part, the model is changed to include multibody dynamics, where the floaters are connected. In the real system, rods keep the floaters in place as much as possible. To model this, distance joints are added to the rigid floaters. Distance joints ensure that the initial distance between two selected points is kept constant at all times. Since the rod is not able to stretch, distance joints are sufficient. In Figure 33, the connections between the floaters are presented with the red line. The black points represent the connection points.
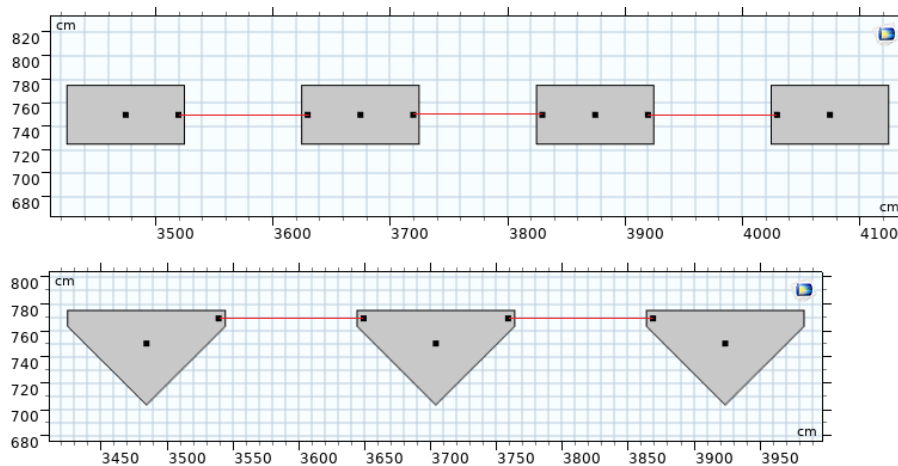
Figure 33: Connection points of the floaters.

For this configuration, the whole array will move with the propagation of the wave, which is undesirable since in the real system the array is fixed to a pole. To obtain a model as close as possible to reality, the first floater is fixed in surge. The rest of the floaters are free to move and are only constrained by the distance joints.

4.8.3   Damping floaters

To model energy extraction, a damper system is connected to the center of mass of the floater. The main reason for a damper instead of a spring is because a damper does not conserve energy. On the contrary, a spring stores the energy and is therefore not suitable to model the energy extraction since the energy is conserved in the system.

A difficulty with modeling the WEC is the fact that the energy is only extracted for positive heave displacements. This implies that the damping forces should only be applied when the floater's motion is upwards. When the floater's motion is downwards, no energy is extracted, where the driving force for the downwards motion is gravity. To model this properly, the damping is made dependent on the motion of the WEC; in this specific case, this is the (heave) velocity of the center of mass. When the vertical velocity is positive (upwards motion), the damping coefficient is set to the selected value. For negative vertical velocity (downwards motion), the damping coefficient is set to 0 and thus there is no damping. To model this in COMSOL, a piece-wise function is created containing the information mentioned above.

$$Damping\ coefficient = \begin{cases} B_{PTO} & \text{if } v_{floater} > 0 \\ 0 & \text{if } v_{floater} \leq 0 \end{cases} \tag{83}$$

where, B_{PTO} is the desired damping coefficient, and $v_{floater}$ is the vertical velocity of the floater.

One of the more complicated settings for the damping is when multiple floaters are present. For multiple floaters, all the floaters have different motions. This implies that for each floater, the damping coefficient has to be determined separately. In COMSOL, for each floater, a different piece-wise function is made. Every piece-wise function has a different input for the velocity, which is measured at the center of mass for the different floaters. In Section 5.4.1, the damping coefficient is discussed further.

4.9   Meshing

In CFD, the mesh is one of the most important parts of the model. The mesh defines not only the number of calculation points (nodes) but also the location. A higher number of nodes increases the accuracy of the solution, but also increases the computational time of the model. It is important to make decisions on meshing and how much time should be invested in a single calculation. Secondly, decisions have to be made on which areas are important and must therefore be meshed densely. A trade-off has to be made, where an increase in the accuracy comes at a cost which is the computational time.

4.9.1   Meshing of the domain

The main idea with the mesh is to have as few elements as possible while obtaining an accurate solution. In this specific case, the most interesting area is the free surface. Certain locations are less interesting, for example, the air domain, or the area left of the wavemaker. To obtain an efficient model, the areas with little interest are modeled with a sparse mesh and the areas of interest with a dense mesh. In Figure 34 the mesh of the model is presented. Please note that due to the size of the domain, the dense meshed areas appear as black areas.
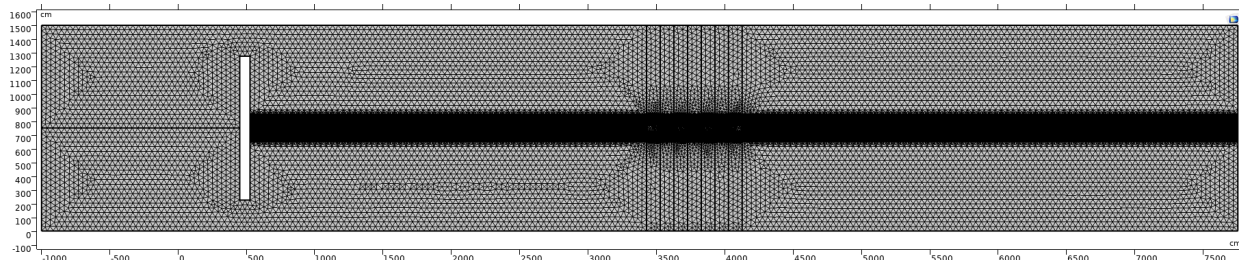
Figure 34: Mesh of the domain.

It is important to keep in mind that the mesh cannot be too sparse since the solution might not converge due to the element size. For the sparse areas, triangles are used to mesh the areas. In the next section, the local refinements are discussed.

4.9.2   Local refinements

In this study, the most important part of the domain is the free surface and its movement; therefore, the free surface is refined locally. A rule of thumb in CFD is that the total wave height should contain at least 15 cells and the wavelength 100 cells [44]. To capture the free surface as accurately as possible, a separate meshing domain is created to allow for a user-controlled mesh. The local refinement is applied to the region where the wave is located, to ensure that the complete wave height is covered in this local refinement. The local refinement uses a mapped mesh, which is the best choice for wave generation in CFD [44] for a few reasons.

1. For mapped meshes, it is easy to control the number of elements.

2. Rectangles are an efficient shape for meshing since fewer elements are needed, though the amount of nodes remains high.

3. Since the water and air domains deform quite a lot, the mesh moves with the domains. Rectangles are an excellent choice for moving meshes, since they are able to stretch quite easily.

The cells do have a high aspect ratio, since they are quite long, although this does not have an influence on the solution [44]. The local refinement for the free surface is presented in Figure 35.
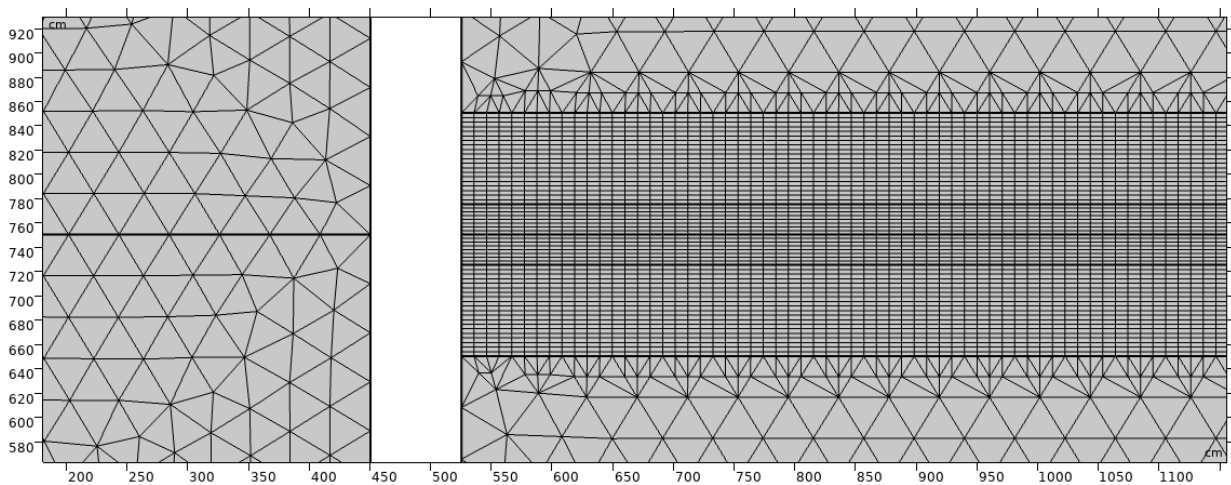
Figure 35: Local refinement for the free surface near the wavemaker.

The local refinements are tested using a mesh refinement study, which is discussed in Section 5.5.2. The second point of interest is the area containing the floaters. The local refinement of the floaters is different from the local refinement of the wave. The rigid domains of floaters have little interest since it is assumed that they do not deform and are meshed sparsely. The areas surrounding the floaters have a dense mesh, where the mesh is partially mapped and partially free triangular. The floaters and the areas above and below the floaters have a free triangular mesh. The main reason for this is because, combined with the moving mesh, the triangles are more capable of deforming with the floaters' movement. This is contrary to the areas surrounding the floaters, which are meshed with rectangles. The main reason for this is that the areas have to respond to different deformations. The areas above and below the floaters have to deal with rotation and elevation, for which triangles are excellent. The rectangular domains mostly deal with general stretching, due to the heave of the floater. In previous iterations of the model, all the domains had a mapped mesh, which caused some numerical issues.
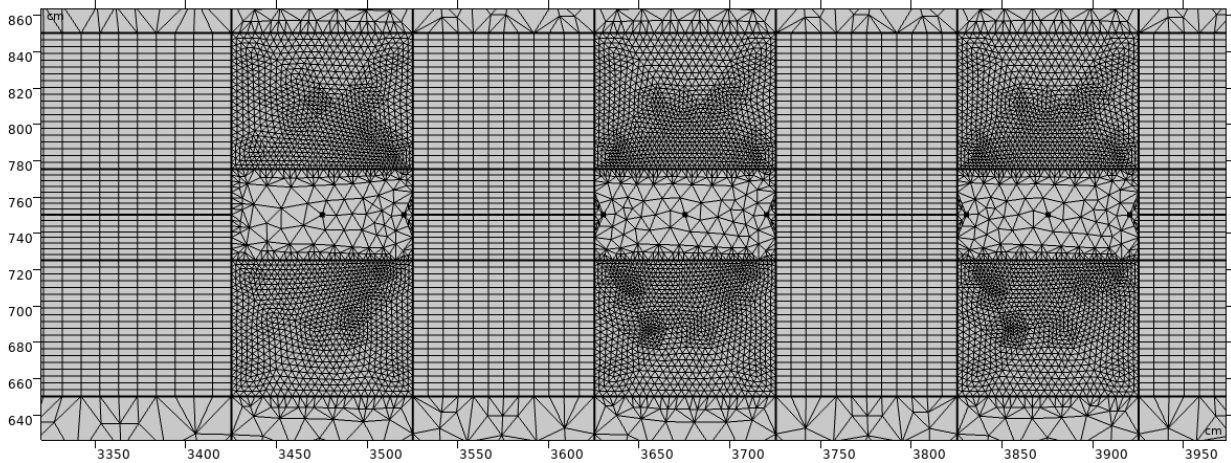
Figure 36: Local refinement of the floaters.

For the final mesh, the mesh consists of 74,798 elements, where 37,614 elements are triangles and 37,184 elements are quads.

4.9.3   Moving mesh

As mentioned before, both the water and air domains are deforming domains. With the deformation of domains, the mesh deforms as well, which is known as moving mesh. The moving mesh is quite important for both the wavemaker and the floaters. An example of the moving mesh is shown in Figure 37.
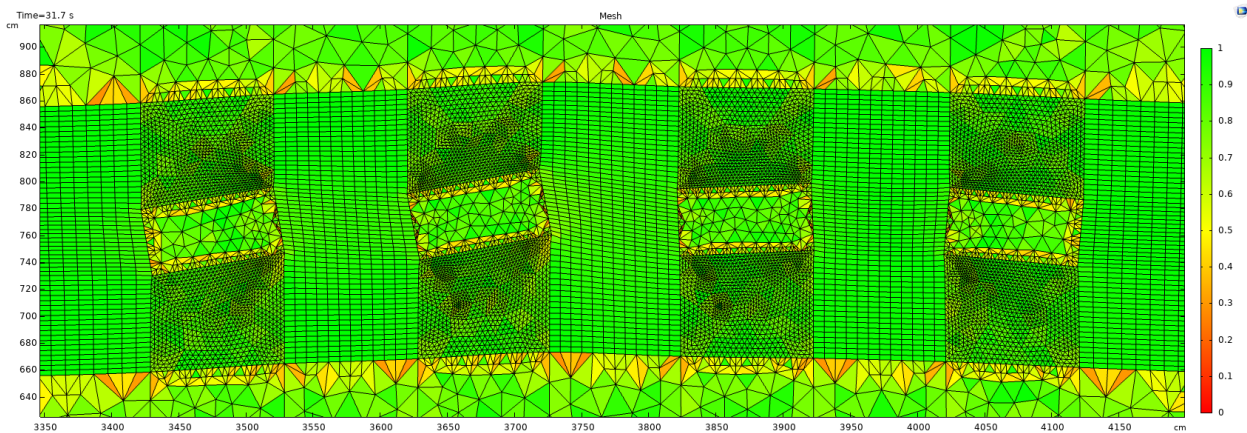
Figure 37: Moving mesh during time-stepping.

As one can see, the mesh moves with the motions of both the wave and the floaters. High mesh quality is important for a moving mesh since the elements must be able to adapt to new shapes and stretch accordingly.

The moving mesh is based on the Arbitrary Lagrangian-Eulerian (ALE) method. In CFD, there is a choice between the main point of reference, which is the point where the fluid is observed. In the Eulerian frame, the point of observation is fixed on the grid. In the Lagrangian reference, the point of observation is fixed in the fluid itself. This implies that the point of observation moves with the fluid. This also implies that the data that is stored is on a fixed point for the Eulerian frame. The data points move in the domain for the Lagrangian method. COMSOL uses a combination of both of these frames, due to the moving mesh. The data is stored in the mesh points, but due to the moving mesh, the data points move. The ALE proves to be a competent method, combing both the Eulerian and Lagrangian schemes.

A new mesh is generated due to the displacement of objects for every time step. For the calculation of the new mesh, a few methods are available. These methods are called smoothing methods, which all have a different approach to generating a new mesh.

1. Laplace smoothing: A linear solver, mostly used for small deformations. The main reason is that there is no mechanism to cope with the inversion of cells. Inverted cells decrease the accuracy and stability of the solution and might cause convergence issues.

2. Winslow smoothing: A nonlinear solver, including control of the inversion of elements. The main drawback is that cells are allowed to stretch quite a lot and there is no control over the maximum stretch. This is a problem in the current study. The first reason is that there are large deformations, causing stretched cells. Secondly, the cells already have a high aspect ratio and are sensitive to stretching.

3. Hyperelastic smoothing: A nonlinear smoothing method, including a control for the inversion of cells. The main drawback is that it does not respond well to large deformations of cells.

4. Yeoh smoothing: A nonlinear method, which not only prevents the inversion of elements but also prevents highly distorted elements. To decrease distortion, the stiffness of elements that have high deformation is increased. The elements surrounding the highly deformed element share the deformation, and the deformation of a single element is spread over multiple elements, reducing the distortion. Yeoh smoothing is the most expensive with regard to computational time.

For this study Yeoh smoothing is selected. The main reason for this is that the domains have large deformations caused by the movement of the wavemaker, waves and floaters. The movements are rather large compared to the mesh size, resulting in inverted elements for poor meshing. This results in numerical instabilities for the first three methods, since elements are inverted with ease. Due to the large deformations in the domain, Yeoh smoothing is the only option, where the main drawback is an increase in computational time.

4.9.4 Mesh refinement study

As mentioned before, an increase in the accuracy of the solution incurs a higher computational cost, but there are certain limits to this approach. An increase in the amount of elements results in an increase in the accuracy, but only until a certain point. The amount of element and the accuracy are not linearly dependent and, after a certain point, the accuracy of the solutions does not increase as much. This point is the optimal point in a CFD study, where the solutions are as accurate as possible, but the computational time is kept as short as possible. A strategy to reach this optimal state is a mesh refinement study. In a mesh refinement study, one decreases the mesh size until the solution does not change or barely changes. The optimal mesh is then the mesh where the solutions are as accurate as possible, with as few elements as possible. The mesh refinement study is conduced in Section 5.5.2.

4.9.5 Solver configurations

Solver selection In COMSOL, there are two choices with regard to the transient solver. The two solvers available are discussed below.

1. Segregated solver: The segregated solver is a solver where the main equation, which is a compiled equation of all the equations in the domain, is split into different steps. An example is where phase field variables are solved separately from the spatial mesh displacement. The main idea is to decrease the complexity by splitting the main formula into smaller steps. The advantage is that the segregated solver can deal with high complexity, but at a cost of an increase in computational time, since multiple equations have to be solved.

2. Fully-coupled solver: The fully coupled solver solves the main equation without splitting it. For simple models with single physics, the fully coupled solver can solve the main equation right away and might be faster. For more complex problems, the fully coupled solver might not converge, or converge slowly.

In the current study, there are multiple physics, multiphysics coupling and a moving mesh present, which results in a complex model. The fully coupled solver is not able to converge and therefore the segregated solver is selected as the main solver. The segregated solver is configurated to split into the main equation into the following steps:

1. Velocities and pressures

2. Phase field variables

3. Displacement field

4. Spatial mesh displacement

For the segregated solver, the maximum number of iterations is set to 10,000 (the default setting is 20). The main reason for this is the initial timestep. The initial timestep is quite complex because there are a lot of changes compared to the stationary solution. An example is the floaters, which start to move during the first timestep. Besides the floaters, the wavemaker moves as well. Most importantly, the fluids start to move, which is quite complex from a stationary state. For the model, the first timestep has a computational time of about 2 hours, where the total computational time of the model is about 20 hours.

Time stepping The timestep for the simulations is set to 0.01s. The timestep is only an indication for COMSOL, where the configured timestep is the maximum timestep. The timestep is decreased if the solution does not converge until either the solution converges or the maximum number of iterations is reached. For most of the models, the initial timestep is decreased to an order of 0.0001 seconds. Unfortunately, the convergence plots are not saved because the model is not solved locally, but on the Peregrine cluster. The main trend is that for the first timestep, the timestep is reduced significantly. Afterwards, the timestep is mostly 0.01s, with some exceptions where the timestep is reduced for a single iteration.

Stability and CFL number The CFL number controls the stability of the numerical simulation. The CFL number ensures that during a single time step, the fluid does not flow through multiple elements. The CFL number is a ratio of fluid flow and the distance of a cell. A CFL of 0.3 represents a fluid flow along 30% of the total length of the cell for example. For skewed cells, the distance of the cell is equal to the cell volume/total surface area. For the velocity of the fluid, the normal is used to identify the direction of the flow. Note that the CFL number differs for different cells since the fluid velocity and element size differ as well. The CFL number is used for the calculation of the adjustable time step. For free surface flow, the CFL number should be below 1; values above 1 would indicate that the fluid 'skips' elements.

In COMSOL, the default setting for the CFL number is 0.1, which is rather low but ensures an accurate solution. For the current model, the velocity of the fluid, the displacement of the floaters and wavemaker per timestep are rather small, since the timestep is quite small. For a full 52 second simulation, the timestep is adjusted due to a too large CFL number for a few instances this is negligible over 5,200 timesteps.

Solving the model To solve the model, the Peregrine HPC cluster is used. Solving the models on a regular PC is not possible at the RUG. The peregrine cluster is a high-performance cluster, containing 210 nodes with 24-28 CPUs each. Each CPU has access to 4GB of memory. To solve the model, 8 high-performance cores are used, allocated with 20 GB of memory. The main reason to only use 8 CPUs is due to COMSOL's inability to use multiple cores efficiently. Tests have been conducted to find the optimal number of cores.

Number of cores	Timesteps completed	Core efficiency
4	289	95.62 %
6	407	95.62 %
8	669	95.45 %
12	412	17.56 %
16	294	6.9 %

Table 7: The performance and efficiencies using a different number of cores.

As one can see, for either 12 of 16 cores, the amount of completed timesteps is lower compared to 8 cores. The efficiency is also lower. This is because the time to exchange information between the cores is longer compared to the time gained by using a larger number of cores. For 3D simulations or segregated solvers with more steps, a larger number of cores might become more efficient. The codes used on the peregrine and a short manual can be found in Appendix C.

5   Model analysis, configuration and intermediate results

In this section, the analysis, configuration of the model and the intermediate results are discussed. Most of the configuration of the model is conducted with trial and error, to obtain desirable effects. An example is tuning the viscosity parameter to reduce the reflection as much as possible. Other aspects that will be discussed are the configuration of the wavemaker to create desired waves, intermediate results in the configuration of the damping coefficient and analyze the particle motion.

5.1   Analysis of wavemakers

To validate the model to the theory on the motion of the particles, a few tests have been conducted. First, the effect of a flap and piston wavemaker is tested. From theory, it is expected that for the flap type wavemaker a circular particle motion is found. For a piston type wavemaker, a more elliptical motion is expected. To track the motion of the particles, the velocity magnitude and direction are analyzed at a fixed point. Unfortunately, COMSOL does not allow for particle tracing. In Figure 38 and Figure 39 below, the particle motion for both a piston and flap type wavemaker is presented.
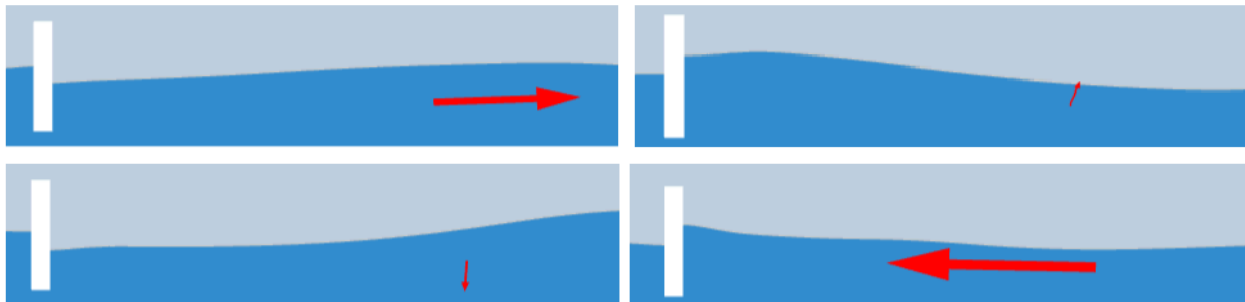
Figure 38: Particle motion using a piston type wavemaker, scaled arrow.

Figure 39: Particle motion using flap type wavemaker, scaled arrow.

One can see that in Figure 38, representing the piston type wavemaker, the horizontal velocity magnitude of the particles is larger compared to the vertical velocity. This results in a more elliptical particle motion which is in line with theory. For the paddle type wavemaker, the horizontal and vertical velocity magnitudes are equal, resulting in a circular motion. Both simulations have sufficient depth for deep-sea waves, therefore, the motion of the particles is not hindered by the bottom of the domain (see Section 2).

5.2   Analysis particle motion

Furthermore, the velocity magnitude should decrease with depth. In a real ocean, the velocity magnitude of the particles decreases because the wave is created near the surface, where the velocity magnitude is the largest, as discussed in the theory section. In the simulation, the velocity magnitude also decreases with depth, caused by the motion of the flap. In the Figure 40 and Figure 41 below, the decrease in velocity magnitude is shown for both the crest and the trough.

Particle motion and propagation
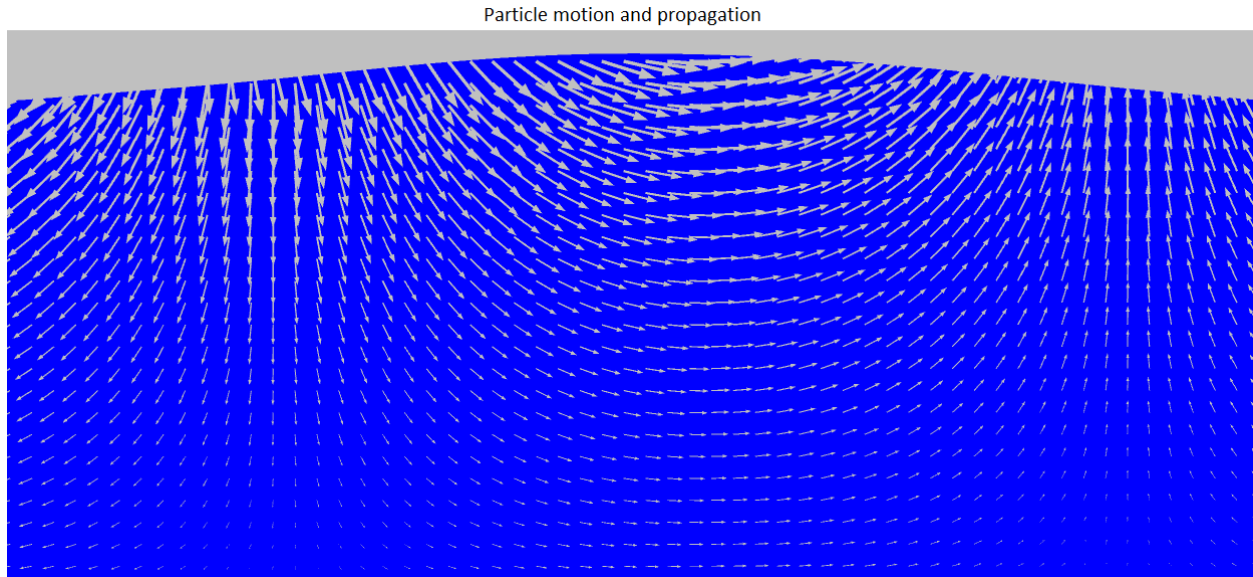
Figure 40: Velocity magnitude flow field for the crest of the wave.

Particle motion and propagation
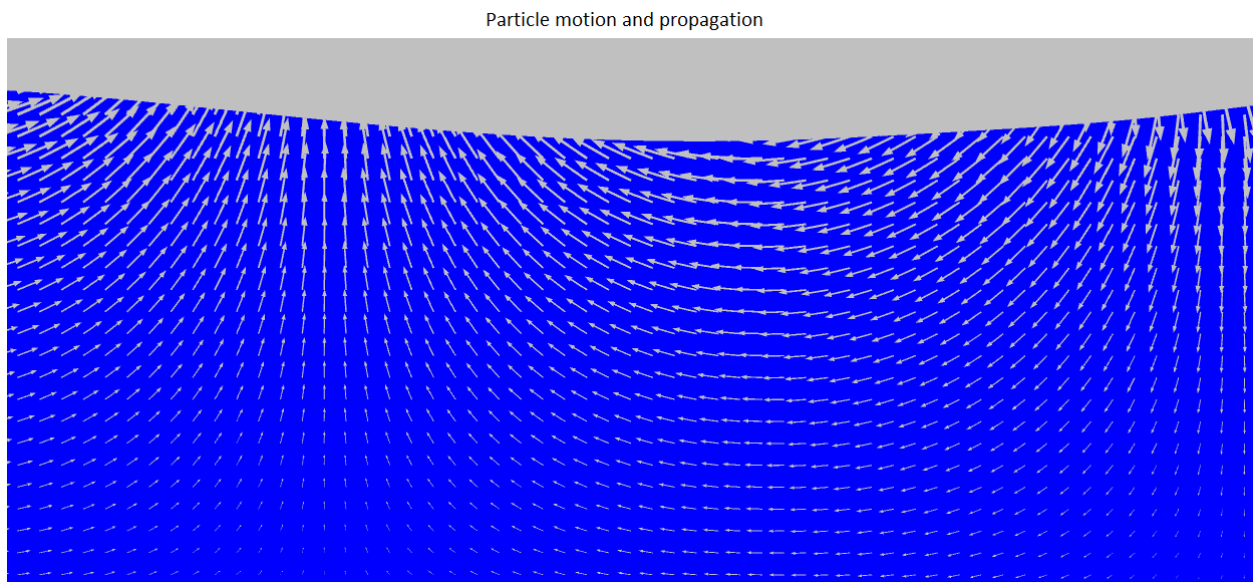
Figure 41: Velocity magnitude flow field for the trough of the wave.

There are a few observations from Figure 40 and Figure 41:

1. The velocity magnitude of the particle decreases with an increase in depth.

2. The particles have a circular motion, which is in line with theory.

3. The motion of the particles is in line with the wave propagation. At the top of the crest, the velocity of the particles is in the same direction as the propagation of the wave. Near the trough, the velocity field of the particles is opposite to the direction of the propagation of the wave.

Overall, the flow field is in line with theory.

5.2.1 Creating waves

The most important factors of waves are the period and the amplitude. Other important parameters like the angular velocity, the group speed and the wave number can be calculated with these two factors. The amplitude of the wave can be regulated with the amplitude of the sinus wave controlling the rotation of the wavemaker (see Equation 76). If the amplitude is changed, the period does not change, which is an interesting result and makes the creation of waves easier. To change the period of the wave, the angular velocity of the sinus wave is changed. The amplitude of the wave does not change when changing the period of the wavemaker. In short, both the period and the wave height can be changed using the angular velocity and the amplitude of the sinus wave. Changing one of the parameters does not directly affect the other parameters; an example is given below, the amplitude of the sinus wave is set to 3°, 5° and 7°.
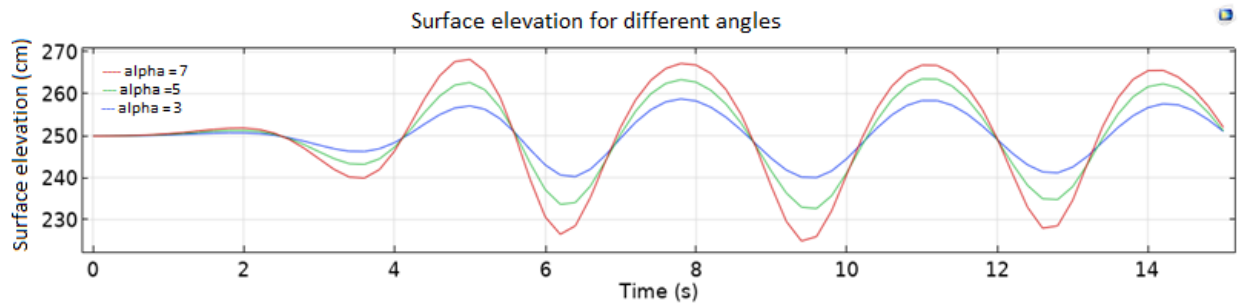
Figure 42: Result of changing the amplitude of the function. On the y-axis the surface elevation is plotted.

The same test has been conducted for the period, a change in the angular frequency did not lead to a change in amplitude.

5.2.2 Relation between wavemaker motion and wave properties

To generate a specific wave, a relation between the wavemaker and the resulting properties of the wave has to be established. As mentioned, the frequency can be set quite easily, since the frequency of the wave is directly related to the angular velocity of the sinus wave. The relation between the period and the angular velocity is presented below in Equation 76:

$$\omega = \frac{2\pi}{T} \tag{84}$$

where ω represents the angular velocity of the sinus wave and T the period of the wave. The frequency can be found using $f = \frac{1}{T}$.

Setting the wave height is quite complicated and requires some trial and error to find the relation between the sinus wave and the resulting wave height. The main reason for this is that the amplitude of the wavemaker is not directly related to the wave height. An increase in amplitude results in an increase in the wave height. To find the exact relation between the two, a test has been conducted. In the test, the amplitude of the wavemaker has different settings and the wave height is measured. The results are presented in Table 8 below.

Amplitude	Waveheight
7.5 deg	1.75 m
10 deg	2.25 m
12.5 deg	2.75 m

Table 8: The parameters selected to investigate the motion of the wavemaker and the resulting waves.

This results in the following graph.
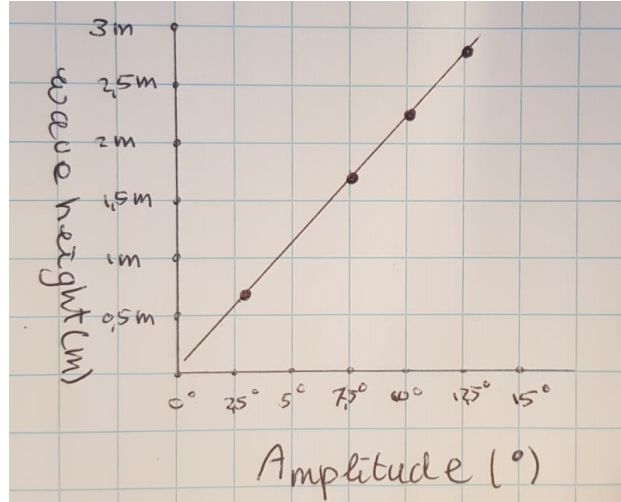
Figure 43: An estimation of the relation between the amplitude and waveheight.

Figure 43 is used later on to estimate the amplitude of the sinus wave needed for a pre-determined wave height. Please note that this is just an estimation, the linear relation is not completely true. This mostly applies for smaller amplitudes, where the movement of the paddle becomes so small that waves are not created, due to a low Q_{wave}.

5.3   Tuning the absorption layer's viscosity parameter

To find a suitable value for the viscosity tuning parameter, a trial and error approach suits the best, since there is no theory available on this. For the starting point, the values from Martinelli's [42] paper are used. A parametric sweep on different values for the viscosity tuning parameter was conducted to analyze the effect of different values. To obtain insight into the effects at different locations, the wave height has been measured at four different locations.

Location number	Location (x-coordinate)
1	22.5 m
2	33.75 m
3	45 m
4	54 m

Table 9: Different measurement locations in the domain.

The main reason to check for different locations is to evaluate the effect of the absorption/reflection since it is expected that the effect of the reflection is larger near the end of the domain, which is the source of reflection.

In Figure 44, Figure 45, Figure 46 and Figure 47, the wave elevation at four different locations for three different viscosity tuning parameters is presented. The simulation runs for 90 seconds, to obtain some insight into the effect over time.
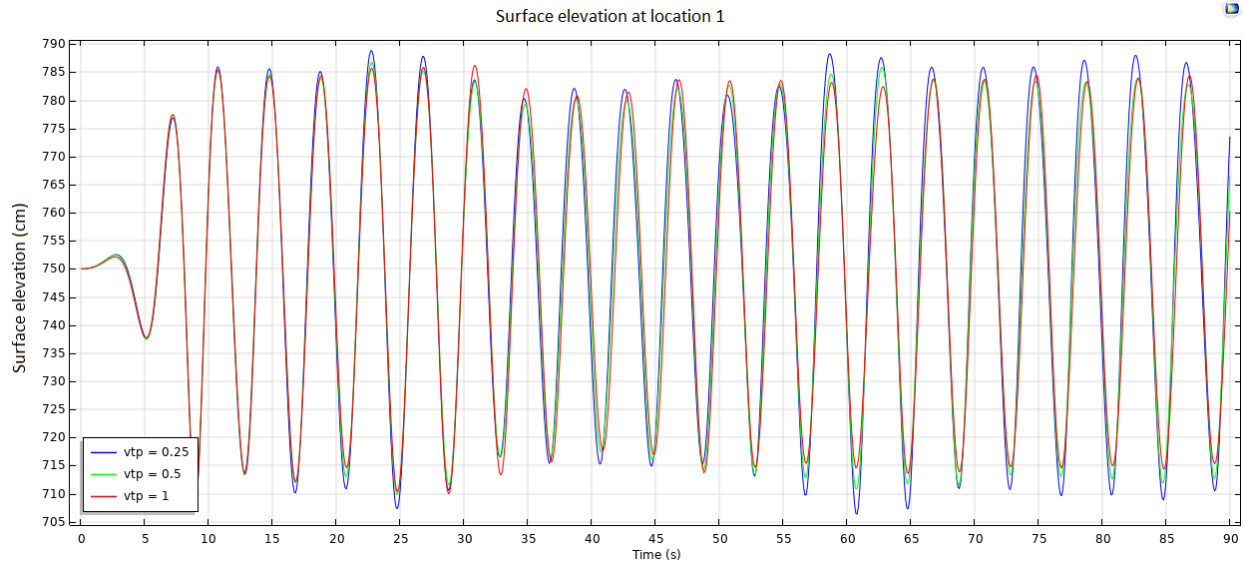
Figure 44: Location 1, x=22.5m. The surface elevation is plotted on the vertical axis. The viscosity tuning parameter is set to 0.25, 0.5 and 1.

From Figure 44, one can see that the viscosity tuning parameter does not play a large role, though an increase in the wave height due to standing waves occurs after about 55 seconds of simulation. The main reason for this that the first fully developed wave arrives at the absorption layer at 25 seconds, whereas the reflection effects also have to 'travel' backward into the domain to affect the locations closer to the wavemaker.
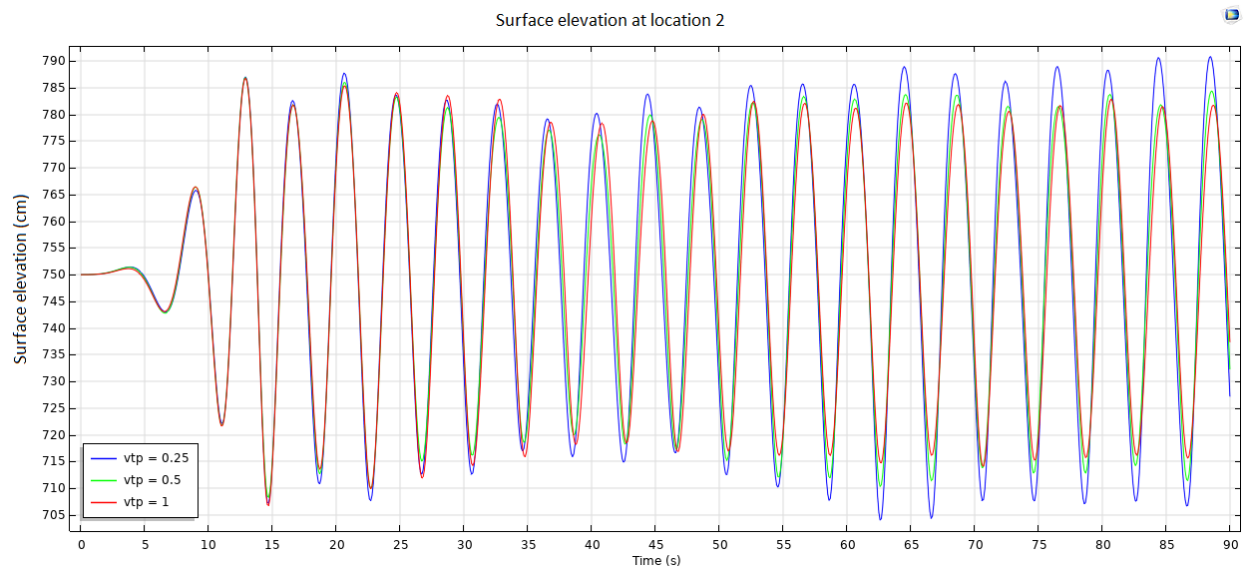
Figure 45: Location 2, x=33.75m. The surface elevation is plotted on the vertical axis. The viscosity tuning parameter is set to 0.25, 0.5 and 1.

In Figure 45 the trend is the same compared to x = 22.5m but the increase in surface elevation over time due to the reflection is more visible and occurs earlier in the simulation since the backward path is shorter, due to its location.
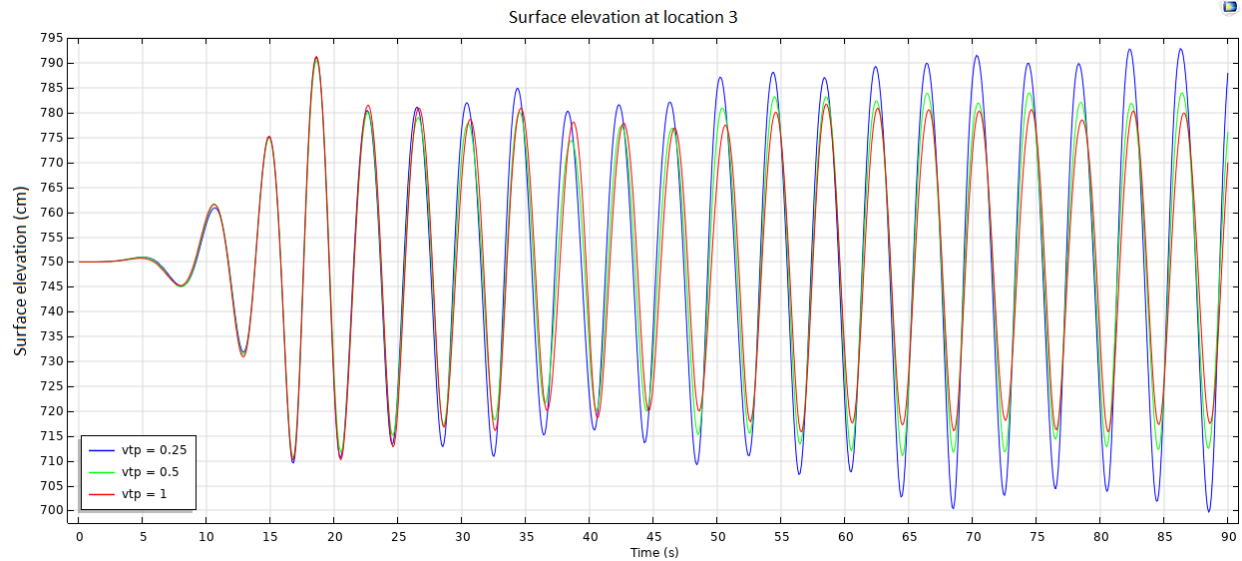
Figure 46: Location 3, x=45m. The surface elevation is plotted on the vertical axis. The viscosity tuning parameter is set to 0.25, 0.5 and 1.

In Figure 46, the trend is the same, but an increase in surface elevation occurs sooner, due to its location. For the furthest location, the results are found in Figure 47.
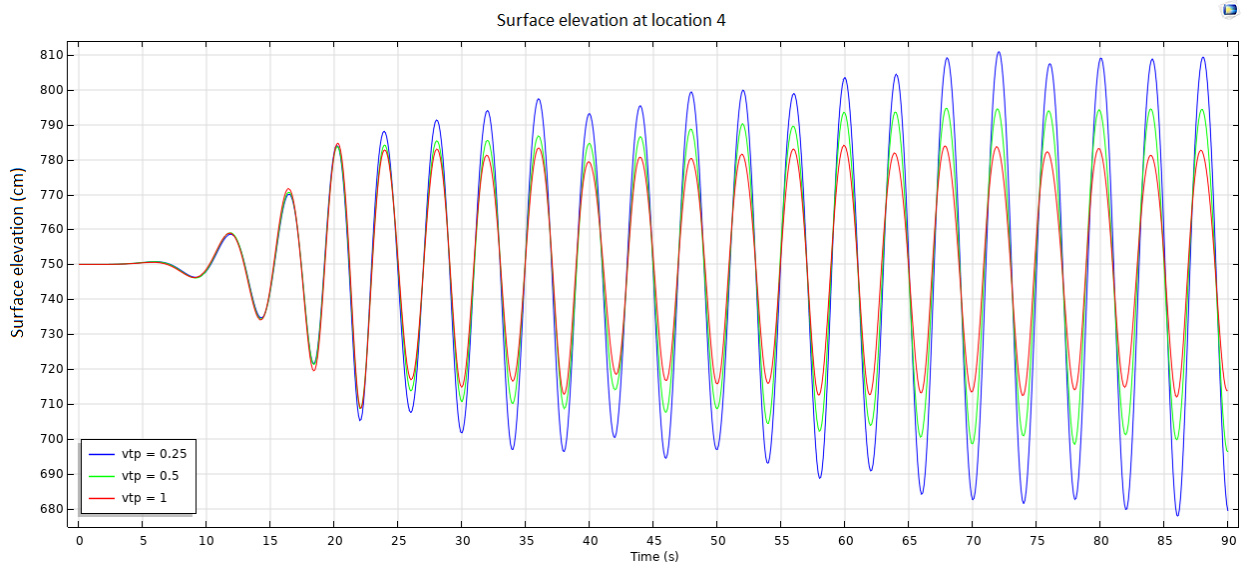
Figure 47: Location 4, x=54m. The surface elevation is plotted on the vertical axis. The viscosity tuning parameter is set to 0.25, 0.5 and 1.

In the final figure where the location is closest to the absorption layer, the effects are most visible. For low values of the viscosity tuning parameter, standing waves occur. For a value of 1, there are no standing waves and there is little to no reflection because the waveheight remains equal before and after the 'back-flow' of the absorption layer.

The main conclusions that can be drawn from the figures are:

1. The reflection effects are stronger at locations close to the absorption layer.

2. A higher viscosity tuning parameter absorbs the wave more effectively compared to lower values.

3. For lower absorption, standing waves are occurring.

4. For a viscosity tuning parameter of 1, the surface elevation is stable for the different locations. The difference in wave height over time remains constant.

The viscosity tuning parameter is set to 1 for the final simulations, since the surface elevation is the most repeatable. Standing waves do not occur for the highest viscosity tuning parameter, since the surface height is stable over time for the different locations. It is not necessary to increase the viscosity tuning parameter further since there is little to no reflection in the domain.

5.4 Analysis of damping for a single floater

In this section, the behavior of the damping coefficient is investigated, to ensure that the damping coefficient and the piece-wise function are working as intended. In Figure 49 below, the damping coefficient and the heave of the floater are plotted. In green, the damping coefficient is plotted (right y-axis), which has a value of either 2,500 kg/s (damping coefficient) or 0, as explained before in Equation 83. In blue (left y-axis), the heave is plotted, measured at the center of mass, since the PTO is connected to the center of mass. For an upwards motion, the damping coefficient is equal to 2,500 kg/s and for a downwards motion, the damping coefficient is equal to 0, as intended.
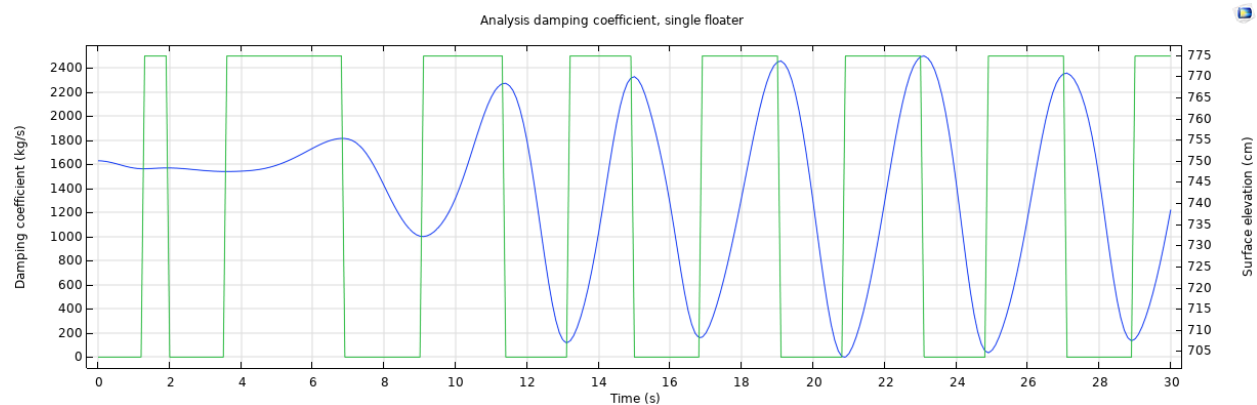
Figure 48: Damping (green) and y-coordinate (blue) of the floater. The left y-axis corresponds to the damping coefficient and the right side y-axis to the y-coordinate of the floater.

5.4.1 Analysis of damping for multiple floaters

For multiple WECs, the damping coefficient becomes more complex. The main reason for this is that each separate floater has a different motion. This implies that each floater has its own damping function, which is based on the velocity of the floater. In Figure 49 and Figure 50, a case with two floaters is presented.
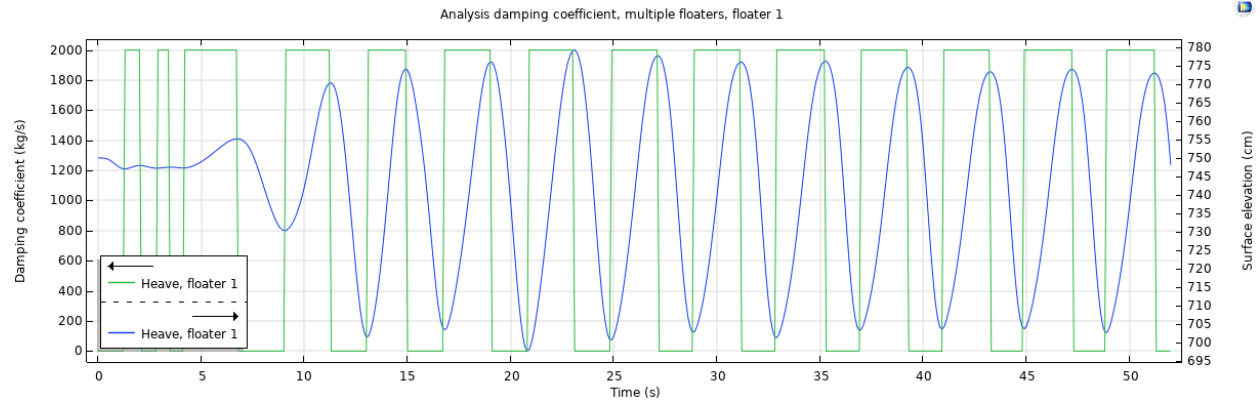
Figure 49: Damping (green) and y-coordinate (blue) of the floater. The left y-axis corresponds to the damping coefficient and the right side y-axis to the y-coordinate of the first floater.
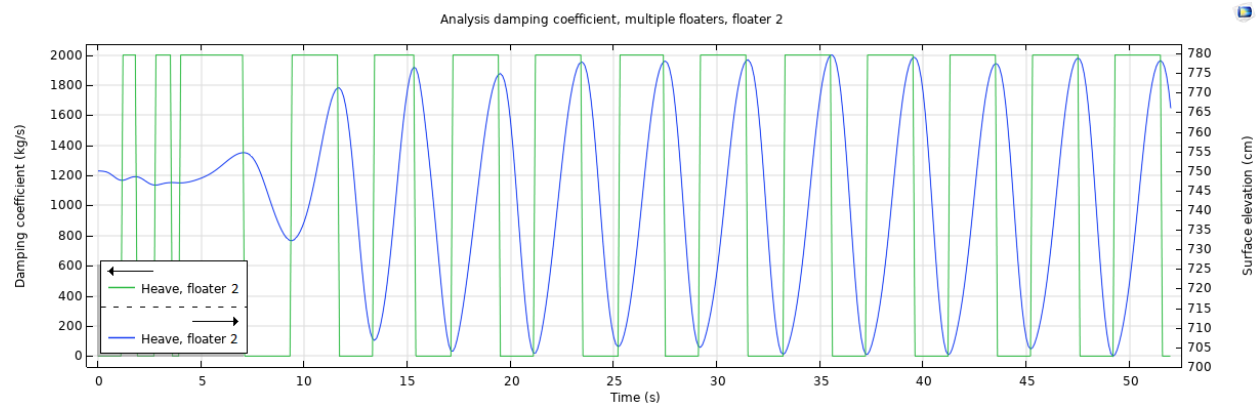
Figure 50: Damping (green) and y-coordinate (blue) of the floater. The left y-axis corresponds to the damping coefficient and the right side y-axis to the y-coordinate of the second floater.

The damping coefficients are in line with the displacements of the respective floater: for an upwards motion (positive velocity), the damping coefficient is increased and for a downwards motion, damping is not applied. In the final simulations, four floaters are present where all the floaters have a different function appling the damping coefficient.

5.5 Mesh refinement study

As mentioned in the model description, a mesh refinement study is an important aspect of CFD, to analyze the trade-off between accuracy and computational time. Besides an analysis of the mesh, it is also important to look for the consistency, or precision of a model, which will be discussed in the following section. Besides precision, the mesh refinement study is discussed in the second section of this chapter.

5.5.1 Precision of the model

To check the precision of the model, a simple test is conducted where the exact same model has been run multiple times, to check for the internal consistency in the model. The main parameters that influence how the solution is computed are the mesh, tolerance and timestep. The mesh has been discussed before where the main focus lies on the density of the mesh. The tolerance controls the allowed error in the solution. If the tolerance is too small, the solution takes unnecessarily long to solve the model, if the tolerance is too high, the

solution might be inaccurate. The timestep is controlled by COMSOL to ensure a CFL value smaller than 0.1.

As one might suspect, the tolerance is the main contributor to the precision of the model, while the mesh size is the main contributor to the accuracy of the solution. The precision of the model was tested alongside the mesh refinement study since both the precision and the mesh refinement study can be analyzed from a single study.

In the first iterations of the model, the model was solved with a difference of 10% in wave height between three separate simulations, which implies a very poor precision. In the first iterations of the model, with low tolerances, the precision was quite low. The main effect is that the results differ, although the model is exactly the same. When the tolerance was reduced, the result is that the model solves with a maximum difference of 0.001%. The tolerance for the final model is set to the value found to ensure that the results are consistent.

5.5.2 Mesh refinement study

For the mesh refinement, the main factor of interest is the number of elements. A general rule of thumb in CFD is to have a minimum of 15 cells per wave height and a minimum of 100 cells in the wavelength [44]. In Figure 51, snapshots of the mesh quality with the high aspect ratio elements are presented, where the element quality is plotted:
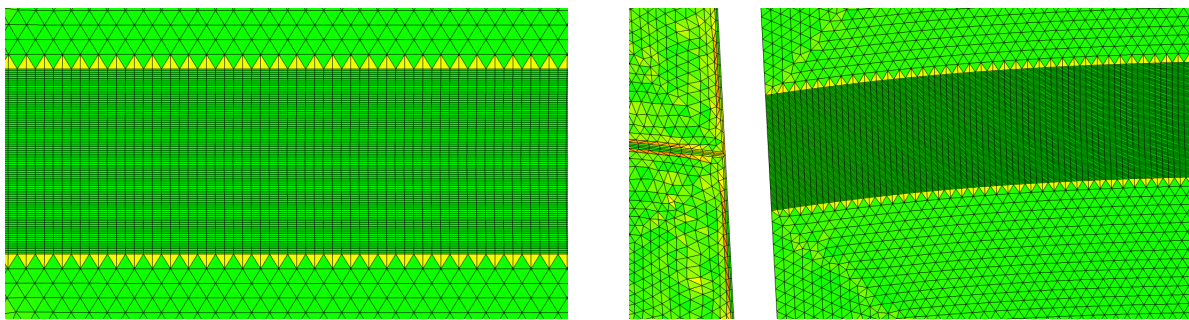
Figure 51: On the left, the mesh quality at t=0 is presented, on the right, the mesh quality at t = 1s is presented, which is the maximum stretch of the mesh.

With a proper mesh, the refinement study can be conducted. The main parameter in the mesh refinement study is the number of elements per wave height. The cells along the wavelength are less crucial since the waves that are generated are quite long and therefore the number of cells in the horizontal direction is always quite high. For the final simulation, the amount of elements per wavelength is 250.

For the mesh refinement study, the rule of thumb for the number of elements per wave height is used as a starting point to acquire accurate results. A parametric sweep is conducted for a different number of elements. The values for the parameter can be found in Table 10.

Parameter mesh	Elements per waveheight	Element height
10	14	5 cm
20	28	2,5 cm
30	42	1,65 cm
40	56	1,25 cm

Table 10: Parameters for the mesh refinement study.

To evaluate the accuracy of the solution, the most important factor of the model is evaluated which, in this case, is the surface elevation. The results for the mesh refinement are presented in Figure 52. The accuracy

is high if the solutions with a different number of elements overlap, where the same results are produced. To choose the final number of elements, the least number of elements for an accurate solution is selected.
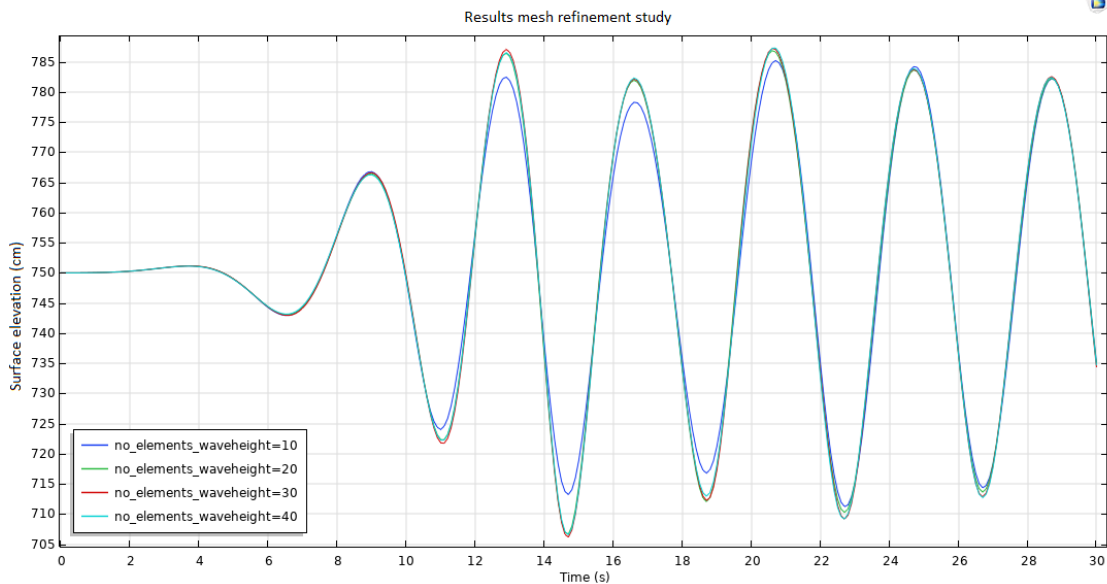
Figure 52: Surface elevation plot for the four different cell heights.

There is a large difference in the solution for 14 cells per wave height compared to the other parameters. Varying the rest of the parameters (28, 42 and 56) yields an almost identical result. In Figure 53 a magnification of the area of interest is presented.
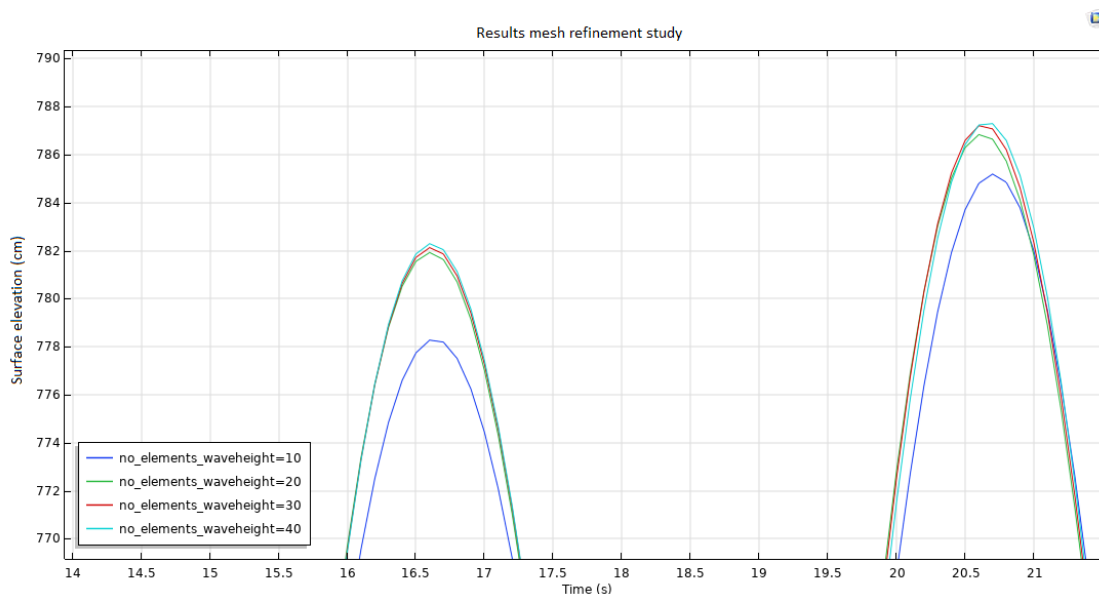
Figure 53: Magnification of the area of interest of Figure 52.

The main conclusion from the mesh refinement study is that for this specific model 14 elements per wave height is not sufficient. At least 28 elements should be present per wave height to obtain a reliable and consistent result. This information is the final piece needed to construct the final model.

6 Results for the damping coefficient

In this section of the results, the damping coefficient is analyzed. The two situations that will be discussed is a scaled floater from a previous study by Y.Wei [45]. In the second case, a large floater is tested, to obtain insight into the effect of different dimensions of the floater.

6.1 Results for the damping coefficient of a scaled floater

In the first section of the results, the results from using different damping coefficients for a scaled floater are discussed. The dimensions of the floater have been scaled from previous papers by Y.Wei and A.Bechlenberg [45] [18]. The properties of the scaled floater can be found in Table 11. The scale of both the floater and the wave is 1:5.

The damping coefficient is an important aspect of WECs. The damping coefficient represents the amount of resistance to the buoy. For a larger damping coefficient, it is harder to move the object, but the energy per velocity is a lot higher. In the end, to obtain the optimal settings for the maximum power production, a trade-off is made between the damping coefficient and the total displacement of the floater.

For the damping coefficient, a few different values have been selected in a trial and error manner, since there is no information about the damping factor in a 2D environment. In initial tests, the damping coefficient was tested for 1,000 kg/s, 10,000 kg/s and 100,000 kg/s. From this first sweep, the results are presented in the table below.

Width	1 m
Height	0.5 m
Density	514 kg/m^3

Table 11: Dimensions and density of the floater.

Damping coefficient	Result
1,000 kg/s	Floater moves with the interface
10,000 kg/s	Floater moves, but is submerged for most of the time.)
100,000 kg/s	Floater does not move

Table 12: Results from the initial sweep.

The range of interest for this parameter varies between 1,000 kg/s and 10,000 kg/s. To obtain a better insight into the results, a parametric sweep is conducted for the following damping coefficients.

Damping coefficient
1.000 kg/s
2.500 kg/s
5.000 kg/s
7.500 kg/s

Table 13: Final selection of the damping coefficients.

6.1.1 Submergence of a scaled floater

As one can expect, when the damping coefficient is too high, the floater might become submerged. Submergence occurs because the damping coefficient is too high compared to the buoyancy of the floater. This is the case for damping coefficient values of 5,000 kg/s and 7,500 kg/s. In Figure 54 below, the position of the floater is shown for different damping coefficients, for t = 23s.
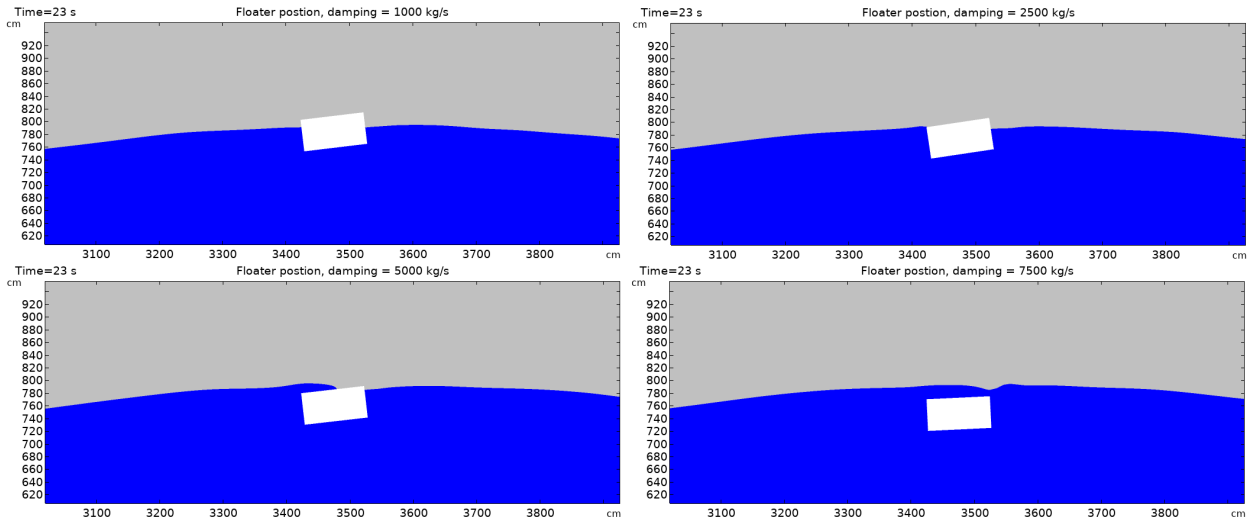
Figure 54: Submergence of the scaled floater, for a damping coefficient of 1,000, 2,500, 5,000 and 7,500 kg/s respectively (upper left, upper right, lower left and lower right).

Submergence of the floater is an undesirable effect for a few reasons, mentioned below.

1. One of the main effects of submergence is slamming, which occurs when the floater re-enters the water after submergence. The hydrodynamic forces caused by slamming are quite high and can lead to material fatigue over time if slamming occurs frequently [46].

2. Besides slamming, the submergence of floaters is an undesired effect since the largest amount of energy is available near the surface, according to linear wave theory. If the floater is submerged, it is located in an area where less energy is available, which reduces the power generated. [47].

3. Finally, to obtain a fully working floater array, where the floaters are connected with mechanical joints, floater submergence would be devastating to the mechanical joints. The main reason for this is that the forces would increase quite a lot if floaters submerge and re-enter the water constantly.

A constraint is added to the damping, where the floater should not be submerged.

6.1.2 Analysis displacement of a scaled floater

The main factor of interest is the displacement of the floater with respect to its damping coefficient. The displacement of the floater should decrease with an increase in the damping coefficient, since the damper absorbs more energy. In Figure 55 below, the displacement of the floater is presented for different damping factors. Please note that the displacement is shown by the current coordinate of the floater. The initial positions are right on the still-water level, at 750 cm.
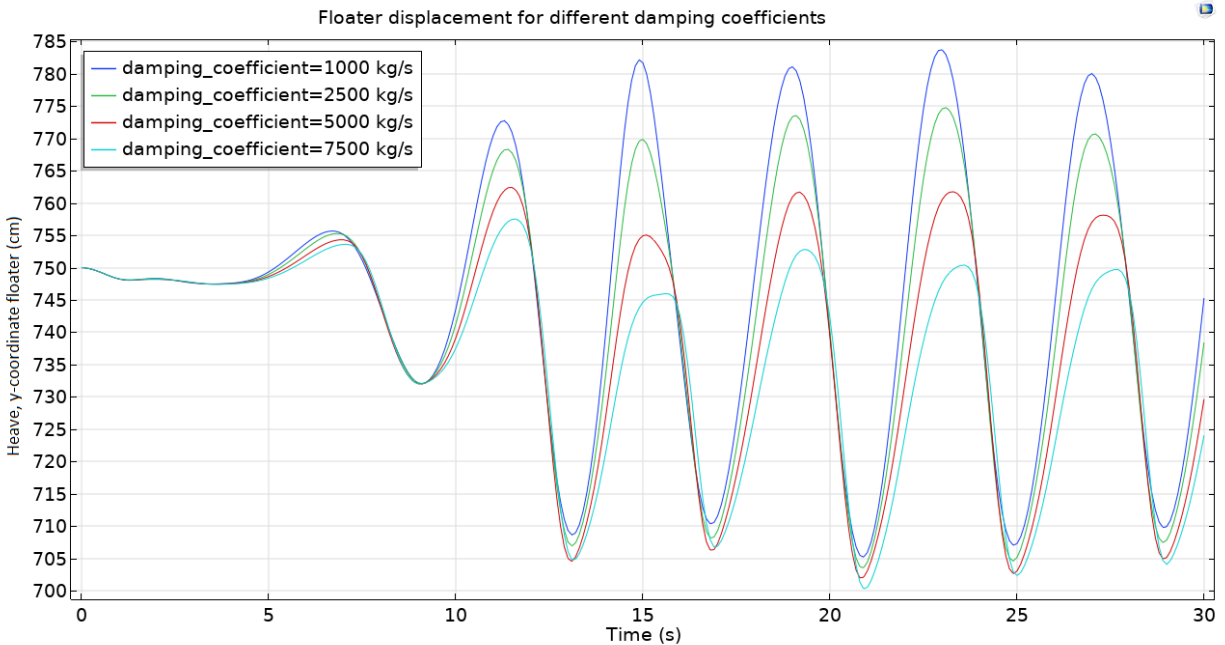
Figure 55: Floater displacement for different damping coefficients.

The results are as expected, where a higher damping coefficient results in a smaller displacement of the floater. With the information from the graph, one can calculate the power generated, which will be discussed in Section 10. Besides the difference in the elevation of the floaters, one can see that there is an inconsistency in the graphs for a damping coefficient of 5,000 kg/s and 7,500 kg/s, where the top of the graphs seems to be flattened and displaced. This effect is caused by the submergence of the floater. For $B_{PTO} = 5,000$ kg/s, the floater is partly submerged and for 7,500 kg/s the floater is fully submerged. For $B_{PTO} = 5,000$ kg/s, the top is only flattened a little, since the submergence has a smaller effect because it is only submerged partially. For the highest damping coefficient, 7,500 kg/s, the top is flattened more, since it is fully submerged. Besides the flattened tops, for the highest damping coefficient, 7,500 kg/s, the period/phase seems to differ a little as well, caused by the submergence. To investigate this change in period, FFT plots of the motion of the floater for different damping coefficients are presented below.
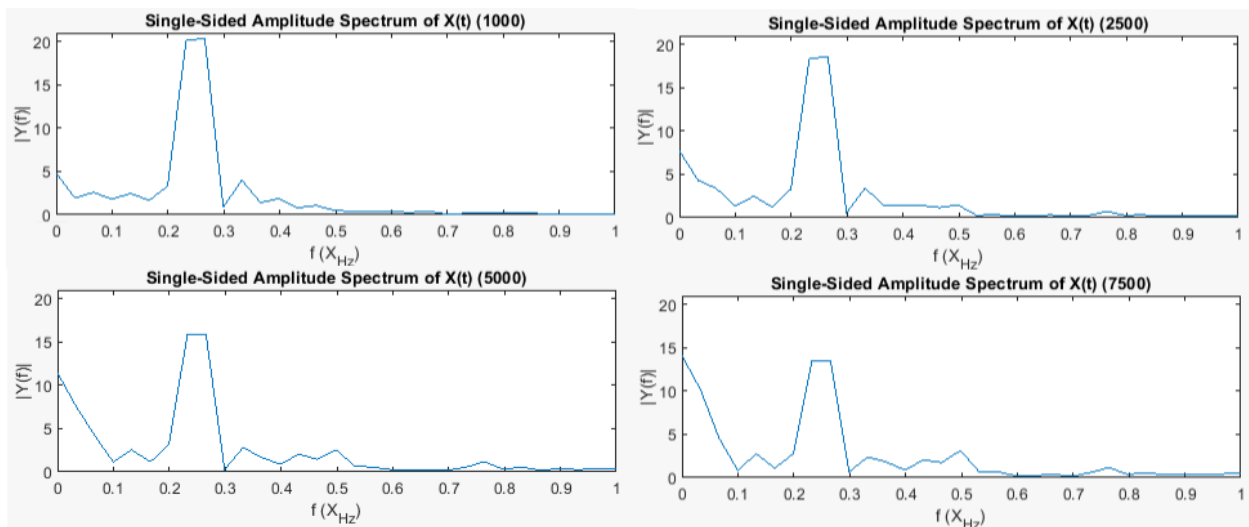
Figure 56: The Fast Fourier transformation of the motion of the floater for different damping coefficients.

From Figure 56 one can see that there is little but notable change in the period. The main point of interest is the decrease in the amplitude of the dominant frequency; more noise occurs if the damping coefficient is higher. The increase in noise is caused by the damping coefficient, which influences the period. Since a phase shift is not visible in an FFT plot, the original figure is used to analyze the phase shift due to damping.
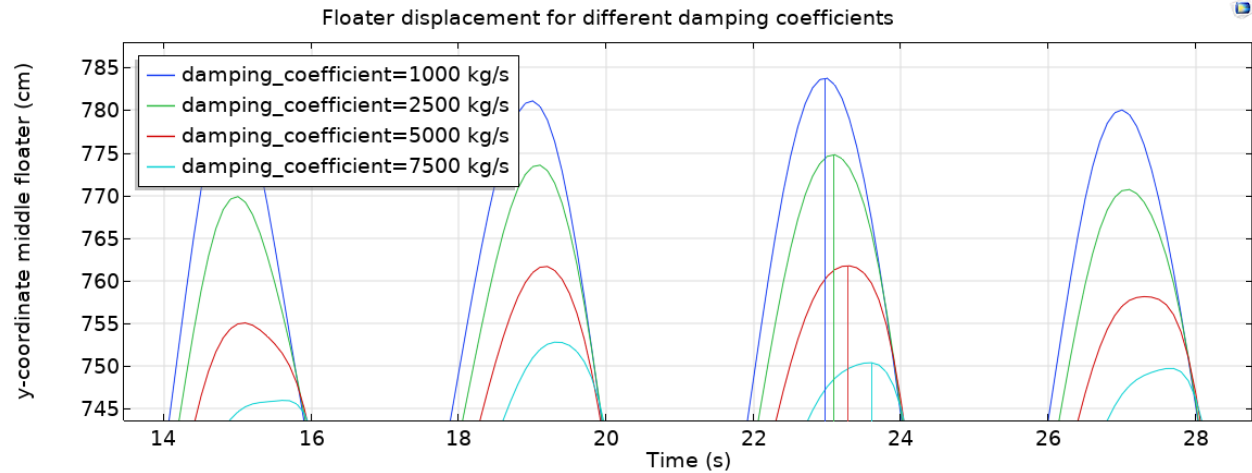
Figure 57: Magnification of Figure 55. The peaks are highlighted by the vertical lines to indicate the maximum heave with respect to time.

In Figure 57, which is a magnification of Figure 55 the tops of the graph are highlighted with the representative color, to highlight that the time of maximum displacement differs. Since for all the damping coefficients the floater is located in the same position, the highest heave should happen at the same time. As one can see, there is a phase shift for the different damping coefficients, especially for the higher values. The main explanation for this is that the damping slows down the motion of the floater, causing a delay in motion. The effect is small and would have little impact in a full-scale system, though it is important to keep this in mind in the final design.

6.1.3 Analysis of the effect of the damping coefficient on wave energy for a scaled floater

In this section, the effect of the damping coefficient on the wave's energy density and behavior is discussed. The wave is measured after the floater has extracted energy, further on in the domain. The main idea here is to investigate the effect of different damping coefficients on the wave after energy is extracted. The behavior of the wave after energy extraction is an important factor when designing a floater array or when multiple floater arrays are present.

From theory, when energy is extracted from a wave, the wave should lose some energy. The energy in a wave is defined by the wave height and/or deformation of the wave. The height of the wave determines the amount of potential energy stored in the wave and therefore provides information on the energy content of the wave. To test this, the results of the damping coefficient are analyzed and used to obtain some insight into the energy left in the wave after extraction. Please note that the partially and fully submerged floaters are also used in this case, $B_{PTO} = 5,000$kg/s and 7,500 kg/s respectively.

To test the wave height after the energy extraction, the surface elevation is measured at a specific location, in this case for x = 50 meters. The location is about 15 meters from the floater. The surface elevation is plotted for the different damping coefficients. The graphs containing this information can be found below.

Since the damping coefficient is not the only factor determining the energy extracted, the energy extracted per floater is presented in Table 14 below. The table will then be used to compare the amount of energy

extracted to the energy left in the wave.

Damping Coefficient	Power generated
1,000 kg/s	150 Watt
2,500 kg/s	330 Watt
5,000 kg/s	460 Watt
7,500 kg/s	N/A

Table 14: The power generated, for $B_{PTO} = 7{,}500$ kg/s there is no data available due to the submergence.
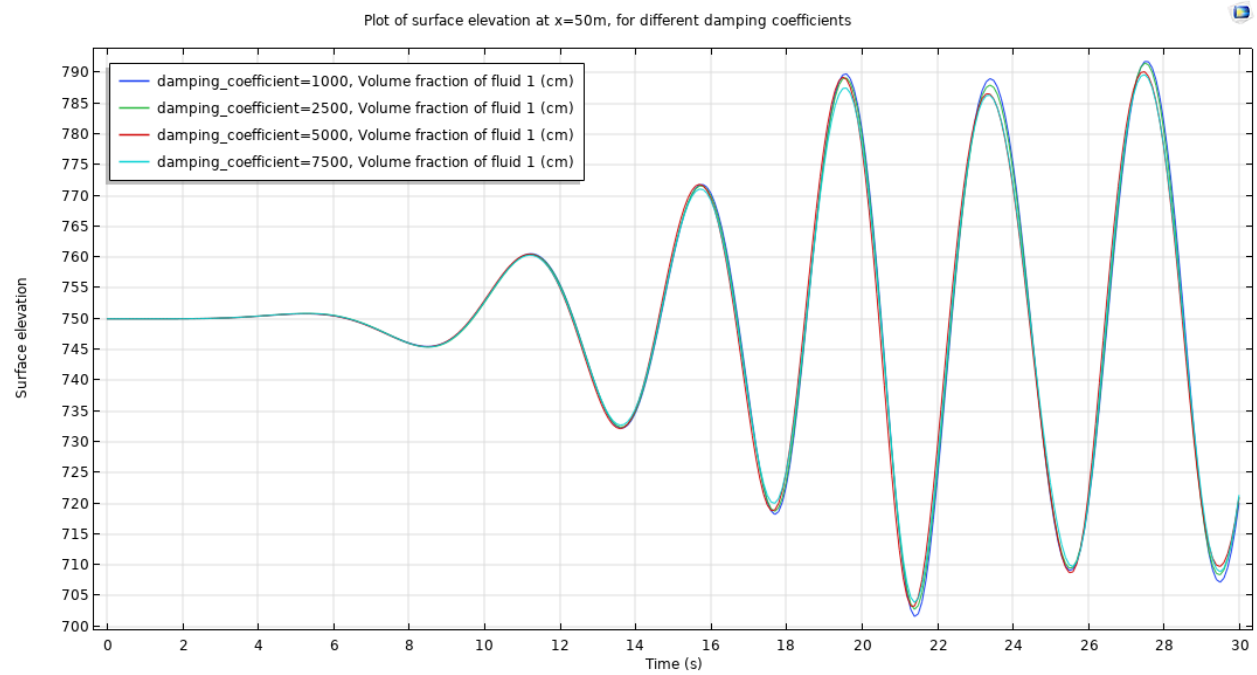
Figure 58: Surface elevation of the wave at x = 50m.

To improve the visibility of the results, a magnification of the tops is presented in Figure 59 below.
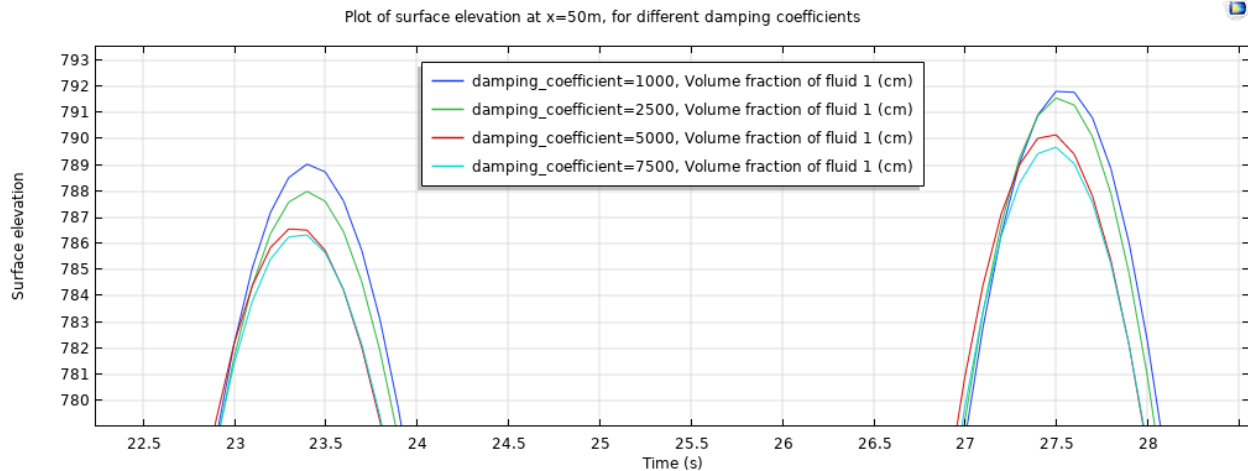
Figure 59: Surface elevation of the wave at x = 50m, magnified.

For increased energy extraction, the surface elevation later on in the domain is smaller. For the first 3 cases, which are either not submerged or partially submerged, the results show that there is a decrease in the surface elevation due to the increase in the damping coefficient and , therefore, the power extracted. For the last case, where the floater is fully submerged, no conclusion can be drawn since the submergence of the floater might impact the wave propagation and therefore change the surface elevation. As one would expect, especially for the first 3 cases, because of the lower surface elevation, the total energy extracted must be higher for a higher damping coefficient [48]. Please note that there are limits to this, since the damping coefficient influences the displacement as well. For example as the damping coefficient tends to infinity, the displacement tends to 0 and so does the power generated. For this specific situation, the 'ceiling' where the energy extracted decreases due to a too high damping coefficient has not been reached. One of the reasons is that the damping coefficient is limited, since submergence is an undesired effect and is therefore not further tested.

As one can see, the hypothesis is correct: higher energy extraction results in a lower surface elevation later on in the domain. The extraction of energy by the PTO affects the wave height and therefore directly the amount of stored energy in the wave.

Another interesting effect is found for the partially and fully submerged floater cases. The period is shifted since the tops of the graph are shifted slightly towards the left. Please note that this effect also occurs with the displacement of the floater, as mentioned in Section 6.1.2. The phase change further on in the domain, might be caused by the energy extraction. The extraction of energy is normally calculated with the height of the wave, which does not represent the total energy present in the wave which also contains potential energy. The wave's potential energy is not only dependent on the wave height, but also on the period, which indicates the wavelength. The length and height of the wave together determine the area that is elevated and therefore the potential energy. In short, the shorter period might be caused because of the lower amount of energy stored in the wave. Secondly, the flow might have been hindered/changed because the floater is submerged, causing the period to change.

6.2   Results for the damping of a larger floater

To obtain a better insight into the effect of the dimensions of a floater on the damping coefficient and the wave energy density after energy extraction, a new model is made with a larger floater. For the larger floater, only the width of the floater is increased to 3 meters. The hypothesis is that the increase in the area increases the total buoyancy force. With the higher buoyancy force, the damping coefficient can be set to a higher value without submerging. To make a direct comparison, the damping coefficients are the same as for the scaled floater.

6.2.1 Submergence of the large floater

For the larger floater, there are no cases of submergence. This can be explained by the increase in the size and therefore the buoyancy. The position of the floater with respect to the interface for different damping coefficients can be found in Figure 60.
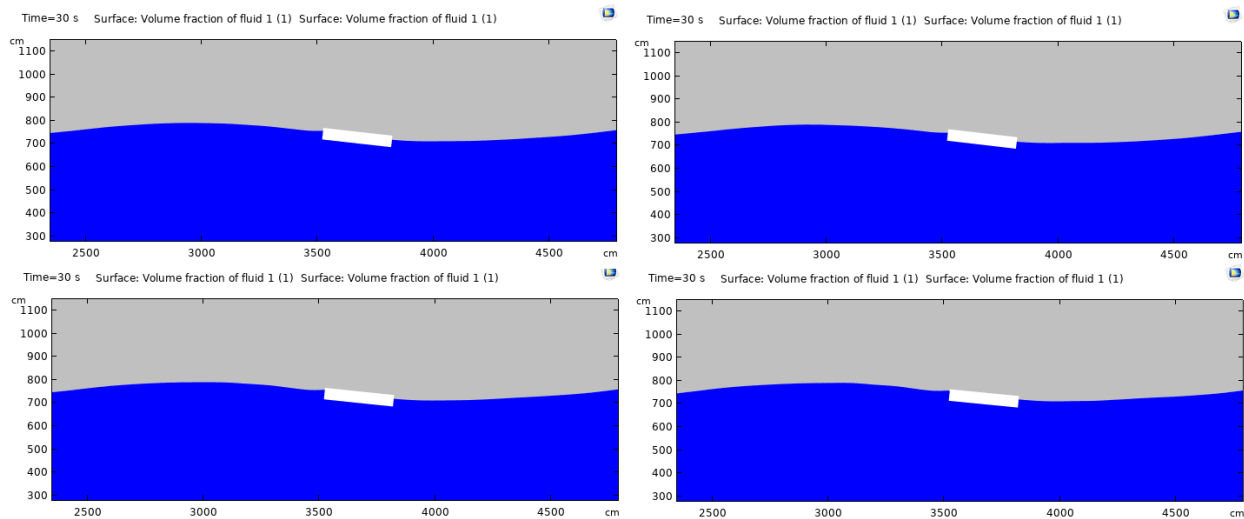
Figure 60: The position of the floater with respect to the interface, for $B_{PTO} = 1000$ kg/s, 2500 kg/s, 5000 kg/s and 7500 kg/s respectively (upper left, upper right, lower left and lower right).

For none of the damping coefficients does the floater submerge. The difference in heave for different damping coefficients is also smaller, compared to the small floater. The difference is smaller because the damping coefficient has a smaller effect on the displacement since the buoyancy is a lot larger.

6.2.2 Analysis displacement of a large floater

The graph for the displacement of the large floater is presented below in Figure 73.
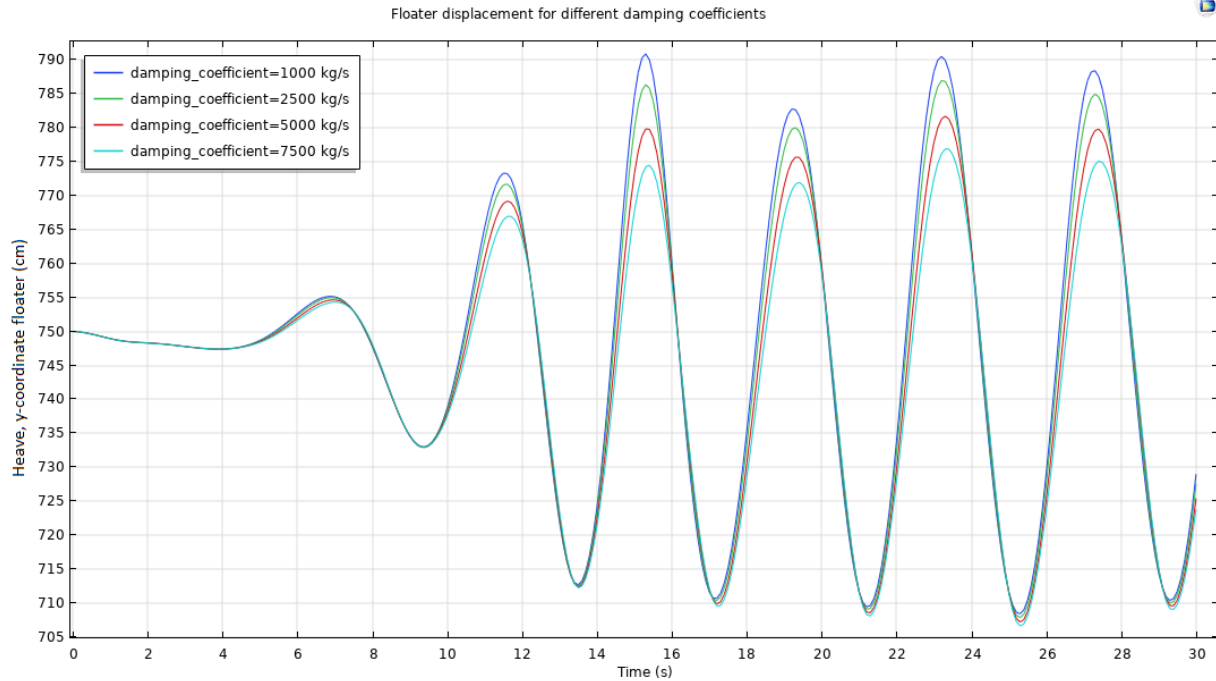
Figure 61: Heave floaters for different damping coefficients.

For the larger floater, the displacement is more constant. There is no change in period or a flattened top, as is the case for the scaled floater. There seems to be a trend, where the difference in displacement for 2,500 kg/s, 5,000 kg/s and 7,500 kg/s seems to be correlated non-linearly since the difference is always around 6 cm in floater elevation for the different settings. The power generated is presented below.

Damping Coefficient	Power generated
1,000 kg/s	195 Watt
2,500 kg/s	451 Watt
5,000 kg/s	810 Watt
7,500 kg/s	1,055 Watt

Table 15: Energy extracted for the large floater case.

6.2.3   Analysis of the effect of damping coefficient on wave energy for a large floater

As with the small floater, the effect of the energy extraction on the wave is analyzed. The strategy is the same, where the wave height at x = 50m is analyzed. For this specific case, because the floater is larger, the difference between the measurement point and the floater is 13 meters. For the scaled floater, the distance was 15 meters. The point of measurement is exactly the same, but due to the increase in the dimension of the floater, the distance is a bit shorter.
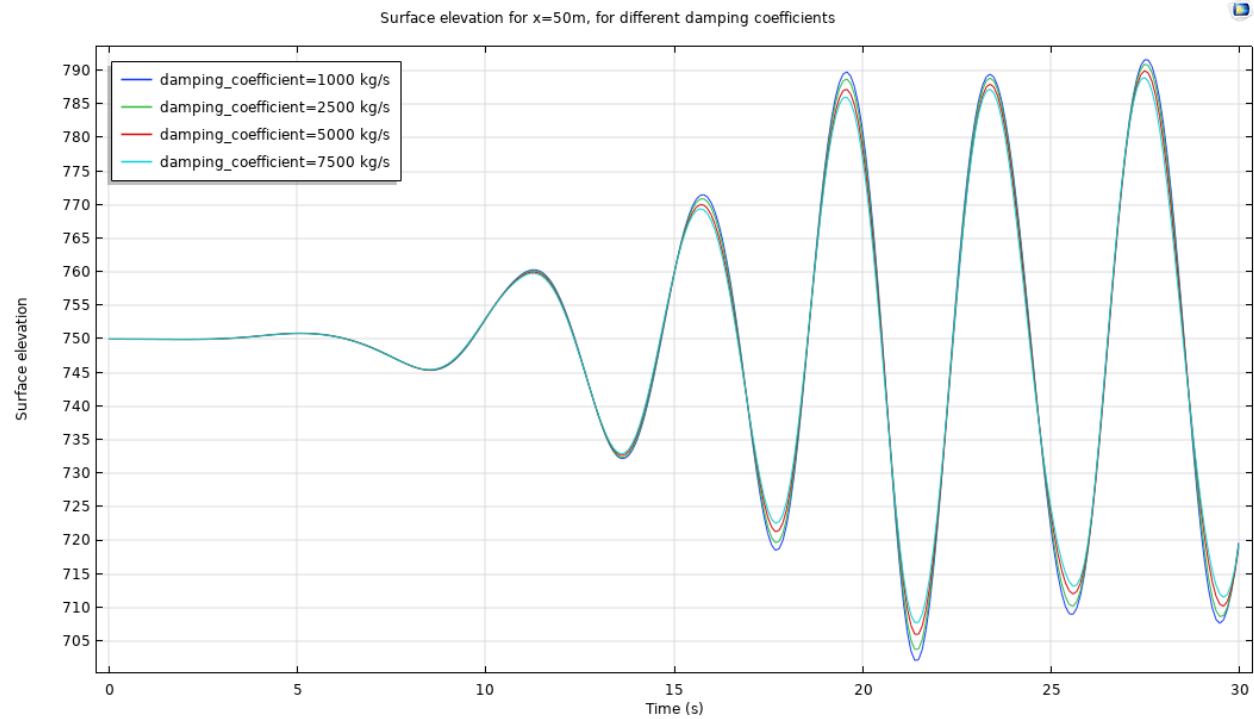
Figure 62: Surface elevation of the wave at x = 50m.
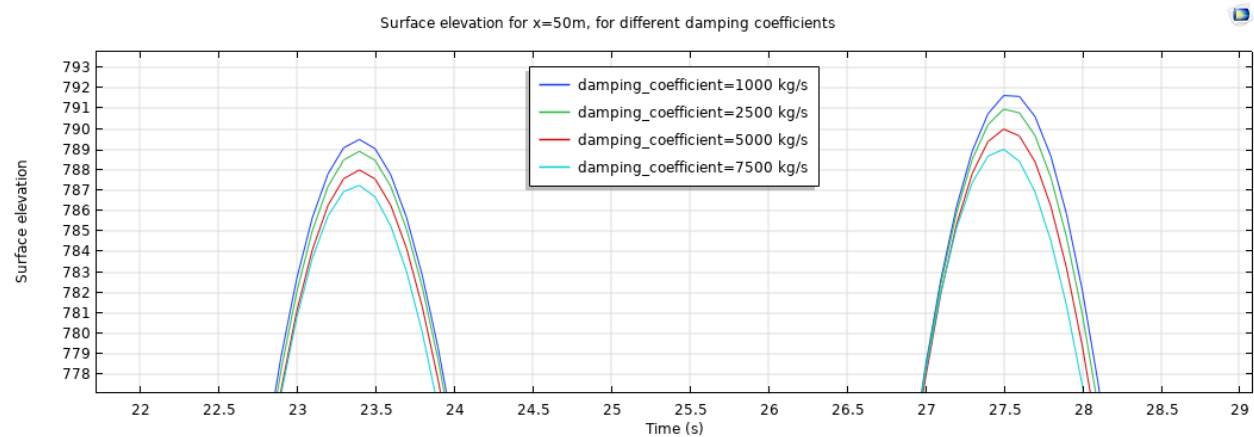
Figure 63: Surface elevation of the wave at x = 50m, magnified.

As with the small floater, there is a decrease in the surface elevation of the wave for higher energy extraction. For the larger floater, the trend can be seen more clearly, since submergence occurs for none of the cases. As with the displacement of the floater, there seems to be a linear relationship between the surface elevation after energy extraction and the damping coefficient. In this case, the difference in surface elevation at x = 50 meters is about 1 cm for damping coefficients.

With the simulation of the big floater, the effects of the damping coefficient on the wave are a lot more clear and consistent. As one can see, the power is not maximized for this floater, since there is still room for a higher damping coefficient. The main conclusions are that the energy extracted is related to the wave height: if more energy is extracted, the wave height is reduced and therefore the total energy available in the wave as well. Besides the wave height, the period also has an effect on the total energy stored in a wave.

66

7   Results for fixed floater array configurations

In this chapter, the floater array is analyzed for different configurations and shapes. For the different configurations, the distance between the floaters is changed, to investigate the effect of different positions. For the shape, a rectangular floater is compared to a conical floater. In the first chapter, all of the buoys are fixed in the surge direction, as was done in previous studies. In the next chapter, the floaters are connected, to investigate a novel approach using multibody dynamics.

In the Table 16 below, the cases are listed.

	Floater shape	Floater distance	Fixed
Case 1	Rectangular	1 [m]	Surge
Case 2	Rectangular	0.5 [m]	Surge
Case 3	Rectangular	2 [m]	Surge
Case 4	Conical	1 [m]	Surge
Case 5	Conical	0.5 [m]	Surge
Case 6	Conical	2 [m]	Surge

Table 16: The cases that will be discussed for the fixed floaters.

An example is given for case one, to illustrate the distances and shapes. The black dots represent the connection to the PTO and the fixed point, where $u_x = 0$.

Figure 64: Example for case 1 where the black dots represent the center of mass, connection to the PTO and most importantly the fixed point, to fix the floaters in surge.

Besides the shape and distance, all other parameters are kept as constant as possible. For example, the area and density for both shapes are equal, to ensure that the buoyancy of the rectangular and conical floater is the same. The damping coefficient for the floater array is set to 2,000 kg/s. 2,000 kg/s is the optimal setting for the floaters, where the damping coefficient is maximized and submergence does not occur. Please note that for the single floater, the damping coefficient was higher. Higher damping might lead to higher power output, but due to the constraint with submergence, this is not an option.

7.1   Result for surge-fixed rectangular floaters (cases 1, 2 and 3)

In this section, the heave of the floaters is discussed, heave is the key performance indicator for WECs. First, the elevation plots of the different floaters are presented, where the floaters are numbered from left to right. In this section, the rectangular floaters are considered, where only the distance between the floaters is changed. The floaters are fixed in surge.

7.1.1   Results for a surge-fixed rectangular floater array, case 1

The floater elevation for case 1 is presented in Figure 65 below. The elevation is measured from the center of mass since the damping system is connected to the center of mass of the floater. The total dataset has been reduced with respect to time and only the last four periods are used. The system reaches a quasi steady state around 25 seconds. The main reason is that the system is never fully stable, where the are small differences in the heave motion.

Figure 65: Heave of the rectangular floaters, distance = 1m, for t=34s until t=50s.

As one can see in Figure 65, there is a significant difference in the heave of the different floaters. The second floater has the largest displacement in heave. The first floater has the second-largest heave displacement, followed by the third and last floater, respectively. One might expect that the first floater has the largest displacement in heave, since the full energy of the wave is available for the displacement. For the other floaters, less energy is available in the wave due to the extraction of energy by previous floaters. On the other hand, the radiation of the other floaters affects the displacement of the floater as well. The second floater has the highest elevation due to the radiation effects of the other floaters.

To obtain insight into the behavior of the floaters, the motion response with respect to heave is presented, where the original wave without floaters is compared to the wave with the floater array present. The wave height without floaters is 75 cm. The displacement is calculated with an average of the last 4 periods. Normally the response amplitude operator (RAO) is used for motion response of floating objects. The RAO is useful for irregular waves. In this study, only regular waves are considered and it is therefore unnecessary to use the RAO, since the incident wave has the same characteristics for every period.

	Displacement (heave)	Response amplitude
Floater 1	70.830 [cm]	0.944
Floater 2	74.918[cm]	0.999
Floater 3	68.288 [cm]	0.911
Floater 4	51.176 [cm]	0.682
Average	66.303 [cm]	0.884

Table 17: Motion response with respect to the original wave, distance = 1m.

From the motion responses in Table 17, the second floater has the highest motion response of almost 1. A value higher than 1 would imply that the floater's displacement is larger than the wave height, which is not uncommon due to the radiation effects.

7.1.2   Results for a surge-fixed rectangular floater array, case 2

For the second case, the distance between the floaters is 0.5 meters. The displacement plot in heave is presented in Figure 66 below.
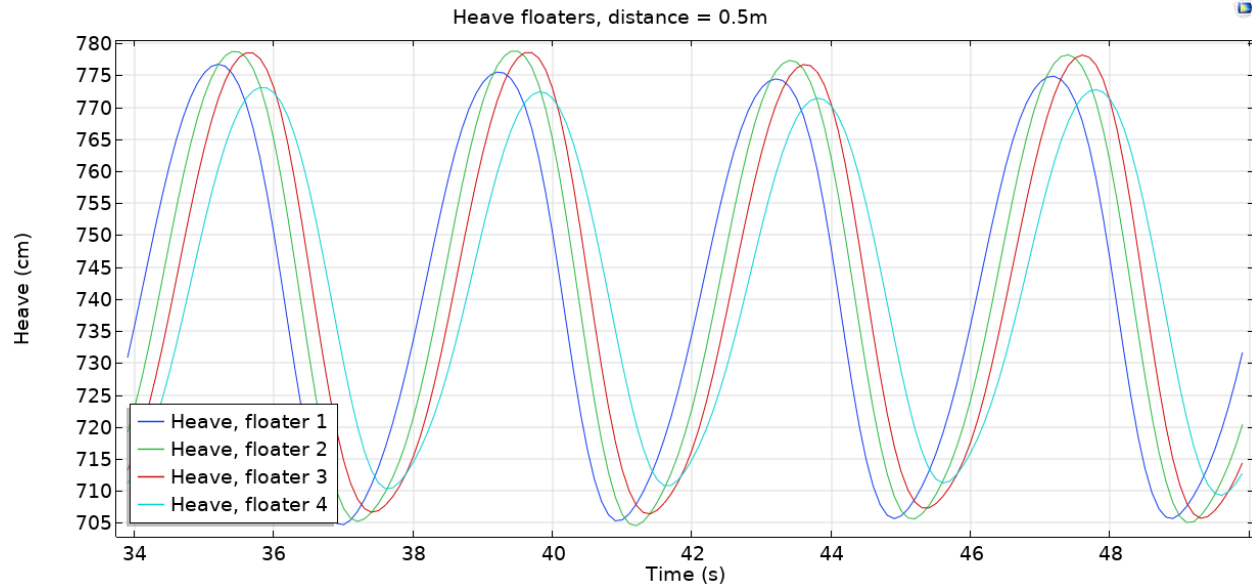
Figure 66: Heave of the rectangular floaters, distance = 0.5m, for t=34s until t=50s.

For case 2, the trend is equal to case 1. The main difference is that the displacement of the different floaters differs less, as the variability is lower. The fourth floater still performs the worst, but not as badly as in the first case. The motion response is presented below.

	Displacement (heave)	Response amplitude
Floater 1	70.061 [cm]	0.934
Floater 2	73.164[cm]	0.976
Floater 3	71.474 [cm]	0.953
Floater 4	62.028 [cm]	0.827
Average	69.181 [cm]	0.922

Table 18: Motion response with respect to the original wave, distance = 0.5m.

Using the motion response, the same conclusions are drawn, where the variability in heave among the floaters is less. A more dense array results in the floaters' heave being more constant, which can be an advantage for designs that require as little variability between the floaters heave as possible. Besides lower variance in heave, the overall performance is better compared to a less dense floater array. The average heave for case 2 is 4.3% higher compared to case 1. The main reason for this is that the more dense array makes better use of the radiation forces. This is because the distance between the floaters is shorter and the waves created by radiation are less damped, containing more energy. Bold conclusions cannot be drawn, since the sample in this study does fully cover the maxima. An even more dense or sparse array might produce different results, which are not discussed in this research.

7.1.3   Results for a surge-fixed rectangular floater array, case 3

For case 3, the distance between the floaters is increased to 2 meters. This is quite a large distance for the floaters to be apart from one another, but it should give an insight into the performance of the array if the radiation effects are minimized, due to the longer distance in between the floaters. In Figure 67 the results for the heave displacement are presented.
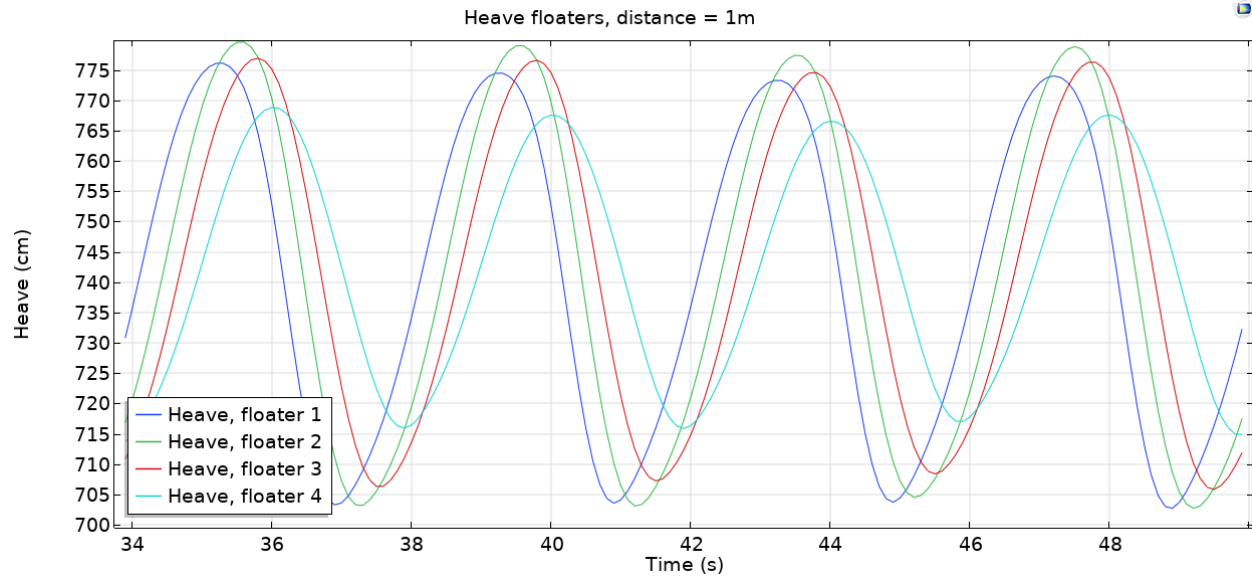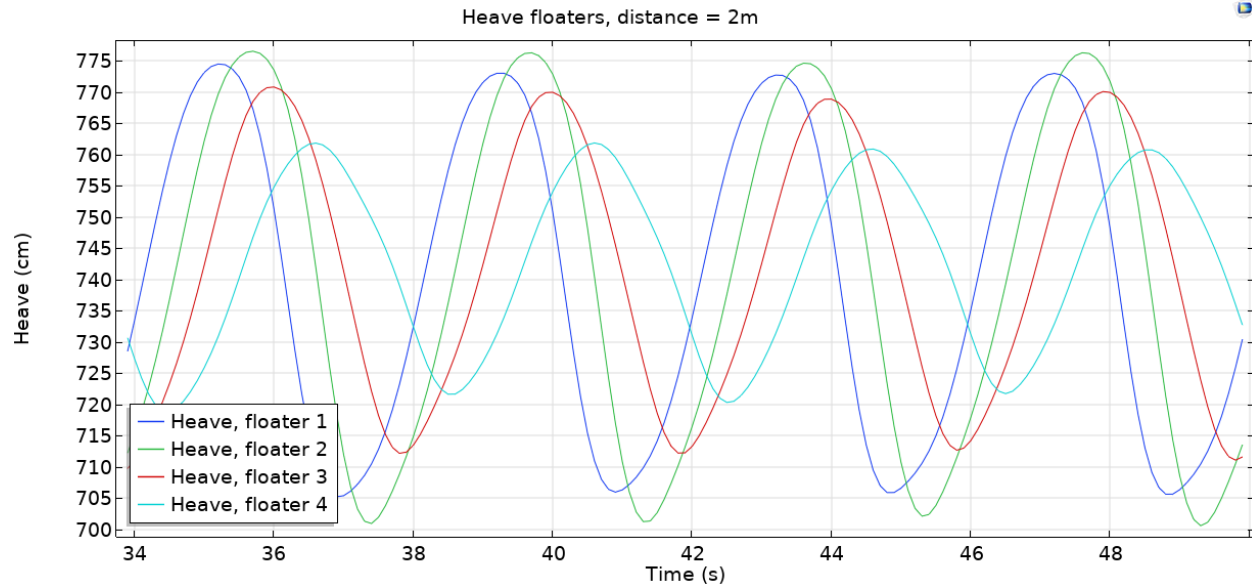
Figure 67: Heave of the rectangular floaters, distance = 2m, for t=34s until t=50s.

As one can see in Figure 67, there is large variability in the elevation of the different floaters. The second floater has the largest displacement of all floaters, as was found for cases 1 and 2. From the graph, it seems that the second floater's displacement is quite a bit larger with respect to the other floaters, compared to case 1 and 2. The motion response is presented in Table 19 below.

	Displacement (heave)	Response amplitude
Floater 1	67.399 [cm]	0.899
Floater 2	74.280[cm]	0.990
Floater 3	71.501 [cm]	0.767
Floater 4	40.317 [cm]	0.538
Average	59.874 [cm]	0.798

Table 19: Motion response with respect to the original wave, distance = 2m.

The variance in elevation for the different floaters is the largest for the last case. The second floater has a motion response of almost 1 and performs the best. The first floater performs second best and the third and final floater perform the worst. The average heave and the motion response are the lowest for this case, mainly due to the large distance since the radiation effects have less impact on the displacement in heave.

7.2   Results for a surge-fixed conical floater array (case 4, 5 and 6)

In this section, cases 4, 5 and 6 are presented and discussed shortly. In this section, the shape of the floaters is conical. The main idea for a conical floater is that the incoming fluid is 'guided' along the lower sides, which could result in a higher vertical motion and less disturbance of the flow field. The area and density are equal to the previous cases. As with the previous cases, the floaters are fixed in surge.

7.2.1   Results for a surge-fixed conical floater array, case 4

In case 4, the distance between the conical floaters is 1 meter. As mentioned before, the parameters are kept as equal as possible to the previous section, to make a direct comparison between different shapes. The results are presented in Figure 68.
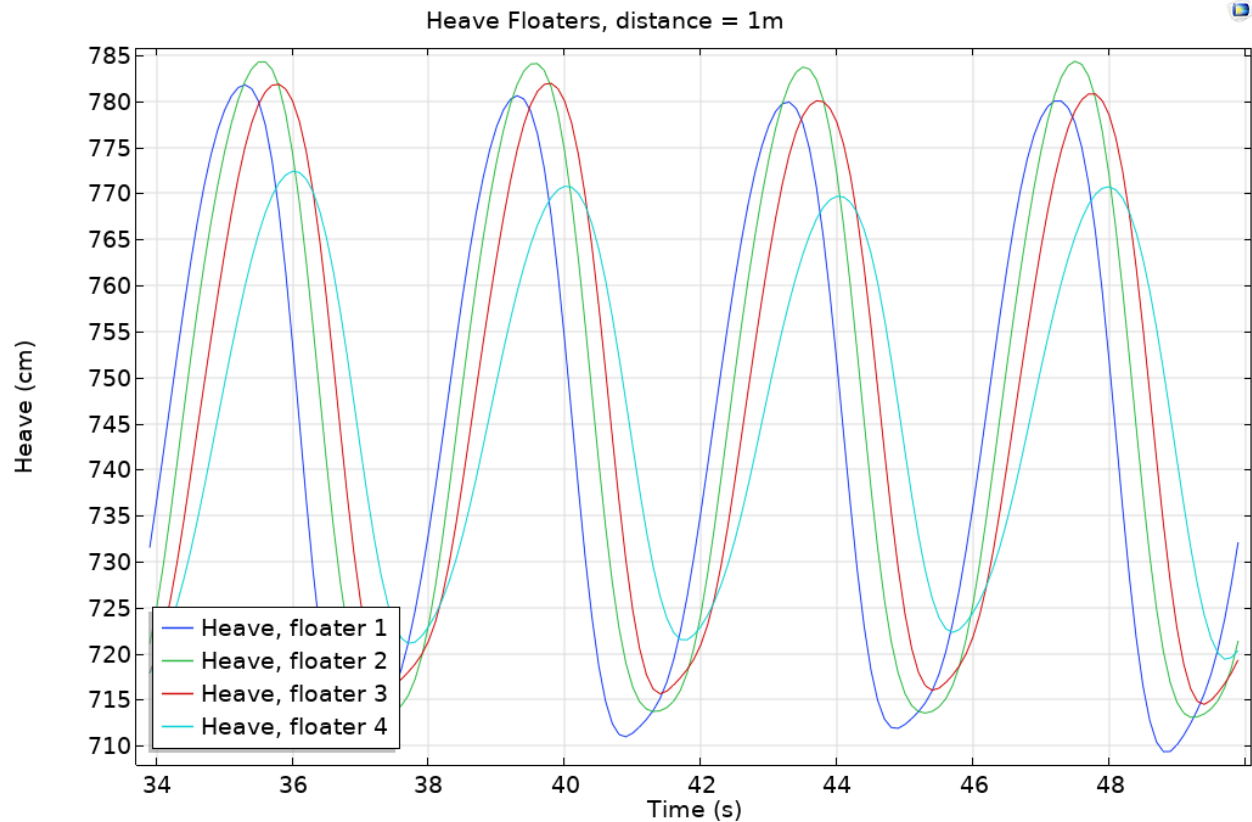
Figure 68: Heave of the conical floaters, distance = 1m, for t=34s until t=50s.

The same trend as with the rectangular floaters seems to be present, where the second floater has the largest elevation, which is caused by the radiation effects of the other floaters. The last floater performs the worst, with a significant difference in heave.

At the lowest point, just before the upwards motion, the graph is a bit flattened. This flattening is caused by the shape, where the total submerged area of the floater is smaller during early surface elevations and the submerged area increases with increased surface elevation. This results in the fact that the floater's response to the surface elevation is a bit delayed since the total submerged area is smaller and therefore the buoyancy force is smaller. In Figure 69 ,below, this effect is visualized. For the rectangular floaters, this effect was not found since the submerged area does not change with floater positions.
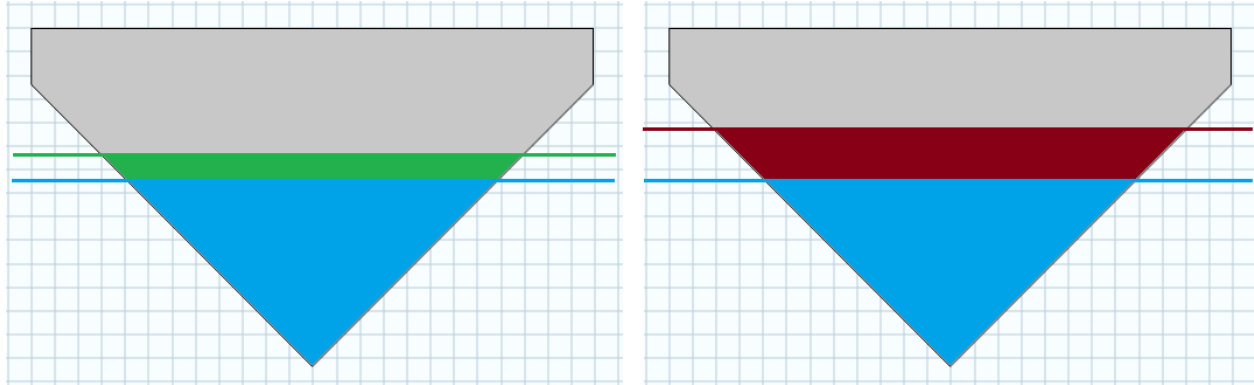
Figure 69: Visualisation of the effect of an increase of the surface elevation on the total submerged area. The blue line represents the still water level. Green and red represent an increase in surface elevation and therefore the total area submerged.

The conical floater has higher rotation compared to the rectangular floaters, due to the less stable geometry. Because of the rotation and the shape, the floater rotates before moving upwards, to cope with the surface elevation of the wave. After a short time, the floater starts to move in the heave direction, since it is not able to cope with the surface elevation by rotation only. This also causes a delay in the response to the surface elevation.

The difference in the rotation is presented in Figure 70 below for case 1 and case 4. As one can see, the conical floater has a higher value for rotation. For the rotation matrix, a positive change implies a counterclockwise rotation and a negative change denotes clockwise rotation.
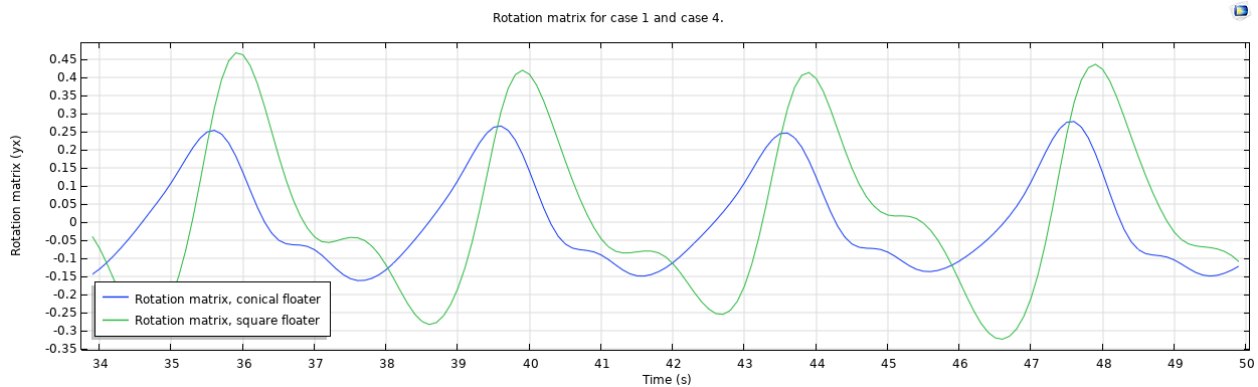
Figure 70: Rotation matrices for a rectangular and a conical floater.

The motion response for case 4 is presented in Table 20 below.

	Displacement (heave)	Response amplitude
Floater 1	73.105 [cm]	0.975
Floater 2	74.599 [cm]	0.995
Floater 3	64.637 [cm]	0.862
Floater 4	41.863 [cm]	0.558
Average	63.549 [cm]	0.847

Table 20: Motion response with respect to the original wave, distance = 1m.

7.2.2   Results surge-fixed conical floater array, case 5

For case 5, the distance between the floaters is reduced to 0.5 meters. The heave of the floaters is presented in Figure 71 and the motion response in Table 21.
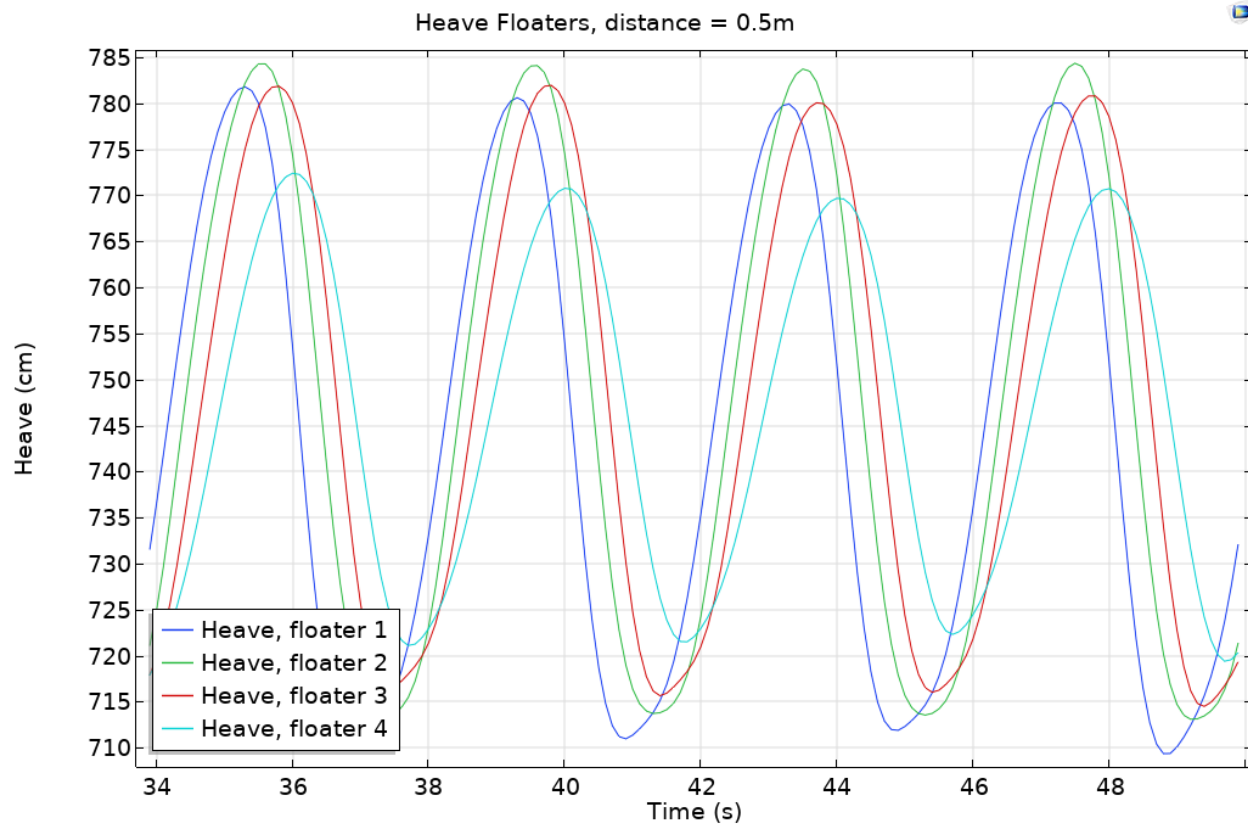
Figure 71: Heave of the conical floaters, distance = 0.5m, for t=34s until t=50s.

	Displacement (heave)	Response amplitude
Floater 1	69.529 [cm]	0.927
Floater 2	70.523 [cm]	0.940
Floater 3	65.174 [cm]	0.867
Floater 4	49.257 [cm]	0.657
Average	63.621 [cm]	0.848

Table 21: Motion response with respect to the original wave, distance = 0.5m.

The second floater has the highest heave, though the total displacement of the first and the second floater does not differ much; the variability is low. The highest elevation of the second floater is higher compared to the first floater, but the lowest point is also higher, resulting in a comparable displacement of the floaters. This is an interesting result, where the displacement is almost equal, but the positions differ for the first two floaters.

For a dense array of conical floaters, the trend is quite different compared to the rectangular floaters. For the conical floaters, a more dense formation (from 1 meters distance to 0.5 meters distance) barely increases the total displacement and therefore the energy produced. The main difference between cases 4 and 5 is that the displacement among the floaters differs less. For 1 meter distance, the first and second floater have significantly higher heave compared to 0.5 meters distance. The third floater performs almost the same for

both cases. The fourth floater has the largest difference for case 4 and 5. In the end, the total displacement is comparable for case 4 and 5. The difference in heave with respect to the average heave (variability)is presented below. The variability is calculated by the difference in total displacement over four periods.

Case 4	Variance (heave)
Floater 1	15.0 %
Floater 2	17.4 %
Floater 3	1.7 %
Floater 4	- 34.1 %

Table 22: Variability heave for case 4.

Case 5	Variance (heave)
Floater 1	9.2 %
Floater 2	10.8 %
Floater 3	2.4 %
Floater 4	- 22.6 %

Table 23: Variability heave for case 5.

7.2.3   Results for a surge-fixed conical floater array, case 6

For case 6, the distance is 2 meters. The graphs of the heave and the motion response table can be found in Figure 72 and Table 24.
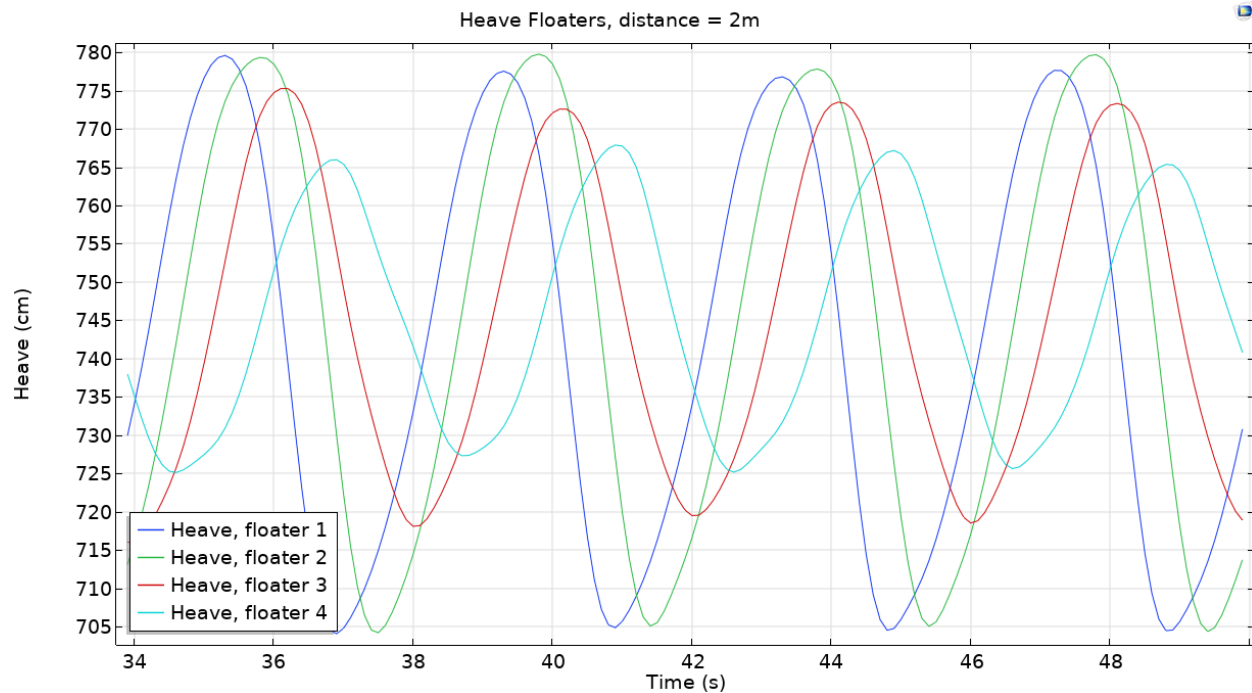
Figure 72: Heave of the conical floaters, distance = 2m, from t=34s until t=50s.

The first observation from the plot is that the first and second floater have the exact same lowest point. For the other configurations, the first floater's lowest position is lower compared to the second floaters, which is not the case for a distance of 2 meters. Since the highest elevation of the second floater is still higher compared to the first floater, the total displacement of the second floater is larger, which results in a higher motion response of the second floater.

	Displacement (heave)	Response amplitude
Floater 1	73.531 [cm]	0.980
Floater 2	74.348 [cm]	0.991
Floater 3	55.003 [cm]	0.733
Floater 4	40.778 [cm]	0.544
Average	60.915 [cm]	0.812

Table 24: Motion response with respect to the original wave, distance = 2m.

From the motion responses, another conclusion is that the third floater performs worse compared to case 4 and case 5. The radiation has less of an impact due to the larger distances between the floaters. The last floater performs the worst with the largest distance between the floaters, as was found for the rectangular floaters.

7.3   Comparison fixed floater arrays

In this chapter, a comparison between the different fixed-floater arrays is presented. First, the average motion responses are presented in Table 25 for the first 6 cases. The average displacement is used to measure the performance of the floater arrays. Please note that the displacement is directly related to the power generation, since the damping coefficient and the angular velocity are equal.

	Average displacement (heave)
Case 1	66.303 [cm]
Case 2	69.181 [cm]
Case 3	59.874 [cm]
Case 4	63.549 [cm]
Case 5	63.621 [cm]
Case 6	60.915 [cm]

Table 25: The average heave for the different floater arrays.

From the table, there are a few conclusions that can be drawn.

1. Firstly, the best performing array is the rectangular array with the smallest distance between the floaters. The main reason for this array outperforming the other arrays is due to the radiation effects of the floaters. As mentioned before, since the maxima are not found, no bold conclusions can be made.

2. Secondly, for the rectangular floaters, the distance between the floaters does have a big impact on the output, whereas for conical floaters, the distance has a smaller influence.

3. Thirdly, the second floater has the best performance for all the floater arrays and the fourth floater has the worst performance. The main reason for this is that the second floater benefits from the radiation the most. For the last floater, the energy in the wave is the least and it benefits less from the radiation compared to the second and third floater.

4. The variance in displacement for different floaters is smaller for a more dense array. A smaller variance is a desired effect, since it allows for a more simple design.

5. The main difference in performance for the different floaters lies with the performance of the last floater, which performs worse with larger distances between the floaters.

The reason why the conical floater arrays do not perform as expected might be explained by the fact that the conical shape is designed for 3D, so that the fluid can flow around and beneath the floater to disturb the flow as little as possible. Unfortunately, this does not work as effectively for the 2D as it does for the 3D case, which is discussed further in Section 9.

8 Results connected floater array configurations

In this chapter, the results of the addition of multibody dynamics are discussed. In the following cases, the floaters are connected with a distance joint, where the specified distance is kept at all times. The inclusion of the multibody dynamics changes the motion of the floaters quite a lot since the floaters can move in the surge direction. Furthermore, the displacement and rotation of the floaters affect each other. The floaters are connected at the sides, where the connection point is located 5 cm from the side. For more information, please consult Section 4.8.2. To ensure that the floater arrays stay in place, the first floater is fixed in the surge motion, as in cases 1-6.

	Floater shape	Floater distance	Constraints
Case 7	Rectangular	1 [m]	Distance joint
Case 8	Rectangular	0.5 [m]	Distance joint
Case 9	Rectangular	2 [m]	Distance joint
Case 10	Conical	1 [m]	Distance joint
Case 11	Conical	0.5 [m]	Distance joint
Case 12	Conical	2 [m]	Distance joint

Table 26: The cases that will be discussed for the connected floaters.
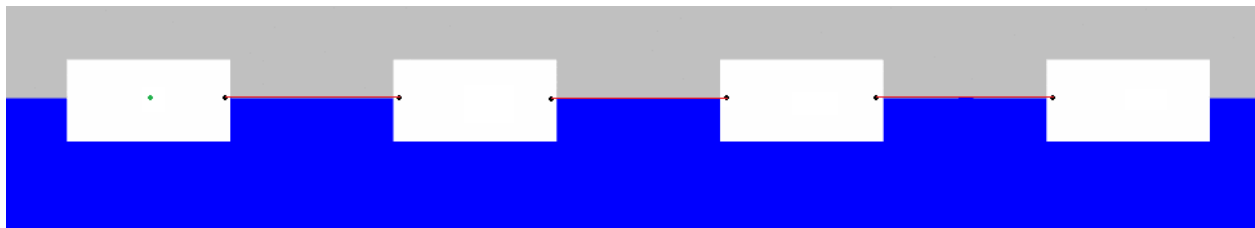
Figure 73: An example for case 7: the green dot on the first floater represents the fixation of the array, where $u_X = 0$. The black dots near the side represent the connection points and the red line the rod connecting the floaters.

8.1 Results for connected rectangular floater arrays (cases 7, 8 and 9)

In the following section, the results are presented for the rectangular, connected floaters.

8.1.1 Results for a connected rectangular floater array, case 7

The results are not as consistent as those for the fixed arrays; this is caused by the interactions of the floaters. Both the rotation and displacement of a floater affect other floaters. For the fixed floater, there was a clear dominant floater with the highest heave, but for the connected array, this differs per period.
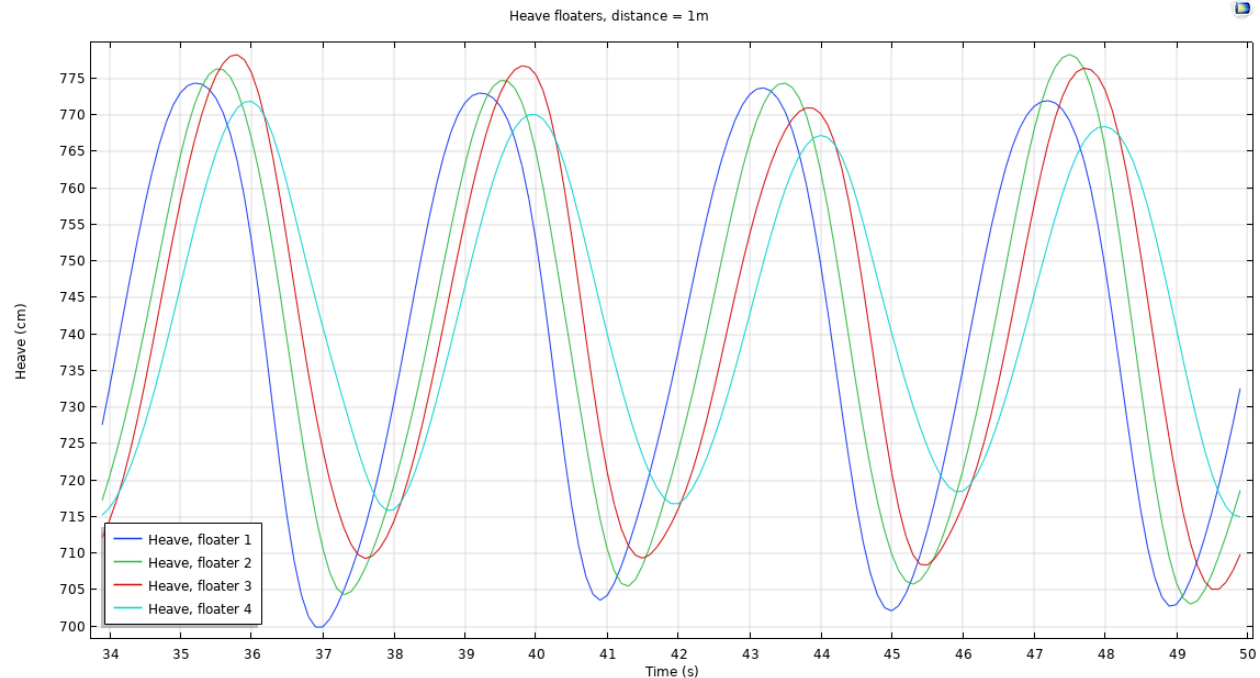
Figure 74: Heave of the different floaters, distance = 1m, for t=34s until t=50s.

The first and the final floater seem to be quite constant in heave. The main reason for this is that the outer floaters are only connected to a single floater, whereas the middle floaters are connected to two floaters. Although the response to the original wave differs quite a lot per period, it is still useful to look into the average motion response to obtain an insight into the performance of the different floater arrays.

	Displacement (heave)	Response amplitude
Floater 1	71.402 [cm]	0.952
Floater 2	70.716 [cm]	0.943
Floater 3	66.588 [cm]	0.888
Floater 4	52.364 [cm]	0.698
Average	65.267 [cm]	0.870

Table 27: Motion response with respect to the original wave, distance = 1m.

From the motion response, one can see that the first floater has the largest heave, closely followed by the second floater. Please note that the first floater is fixed in surge, which might influence the results. As with the fixed array, the fourth floater performs the worst, though the variance is lower compared to the fixed case.

8.1.2   Results for a connected rectangular floater array, case 8

For case 8, there are some complications because the bodies come into contact during the simulation. This causes the simulation to crash since boundary interactions are not allowed in the model. Besides the problem with the simulation, in a real-life context, a collision of floaters is an unwanted effect, since it could damage the floaters over time.

The contact is caused by the force of the incoming wave on the second, third and fourth floater. Due to the impact of the flow on these floaters, the floaters are pushed towards the first buoy. As explained before, during the trough of the wave, the direction of the flow field is opposite to the wave propagation, causing the

floater to move to the opposite direction of the wave propagation. In this specific case, the second floater is in a downwards motion, where the first floater is in an upwards motion. Because of the opposite motions, combined with the effect of the flow field, the second floater is pushed towards the first floater. Due to the restriction of the connection, the floater is forced underwater, where it submerges under the first floater (see Figure 75. For this specific case, the distance is short and the floaters are rectangular, hence the contact occurs sooner compared to other cases. For example, in case 11, where the floater distance is equal but the floaters have a a different shape, there is no collision.
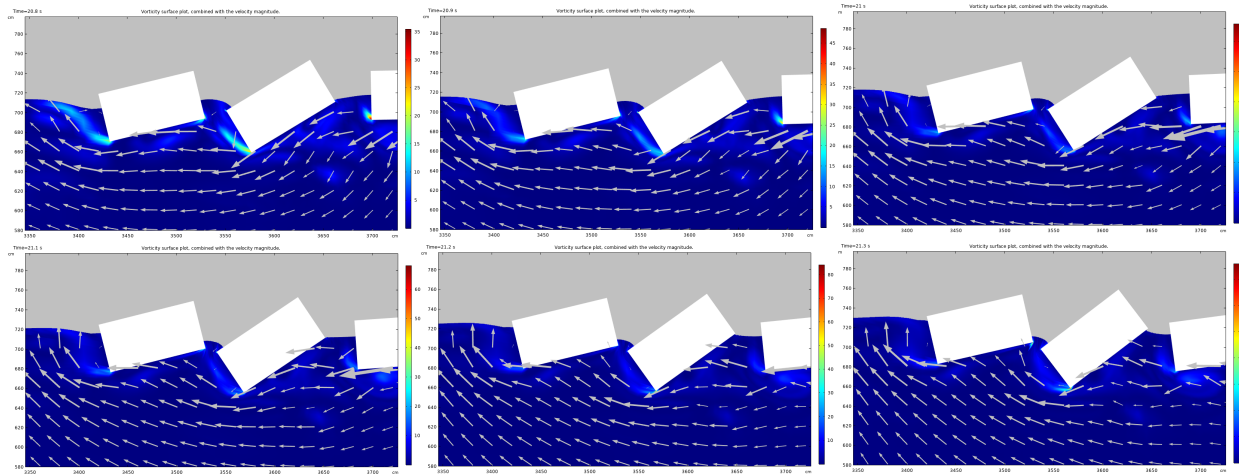
Figure 75: Visualisation of the second floater's collision with the first floater. The flow field is shown to understand the motion of the second floater and its submergence at times t = 20.8, 20.9, 21, 21.1, 21.2 and 21.3 from left to right, up and down respectively.

The collision only occurs when the wave is at its lowest point near the second floater, where the flow field direction is opposite to the wave propagation. The collision does not occur when at the highest point, since the direction of the flow is in line with the wave propagation, while the second third and last floater are pushed away from the first floater.

In short, the collision occurs due to the fact that the first floater is fixed, while the third and last floater push the second floater below the first floater, due to the direction of the flow which is opposite to the propagation of the wave. This is an interesting finding, which is important to keep in mind when designing a floater array.

Because this case would be promising since, for the fixed floaters the heave was the largest for a rectangular floater with a distance of 0.5m, a special case was designed. In this case, the corners were removed and the size increased, to keep an equal area. The result from this case was the same, where the bodies contact each other because the first floater is fixed and the connections are rather short.
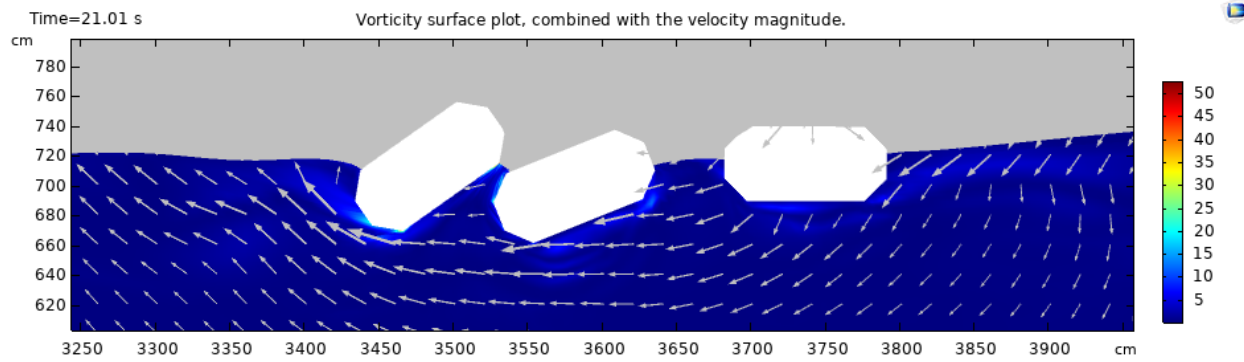
Figure 76: Visualisation of the second floater's collision with the first floater for the special case.

8.1.3   Results for a connected rectangular floater array, case 9

For the final rectangular, connected array case, the results from the heave are presented in Figure 78 below.
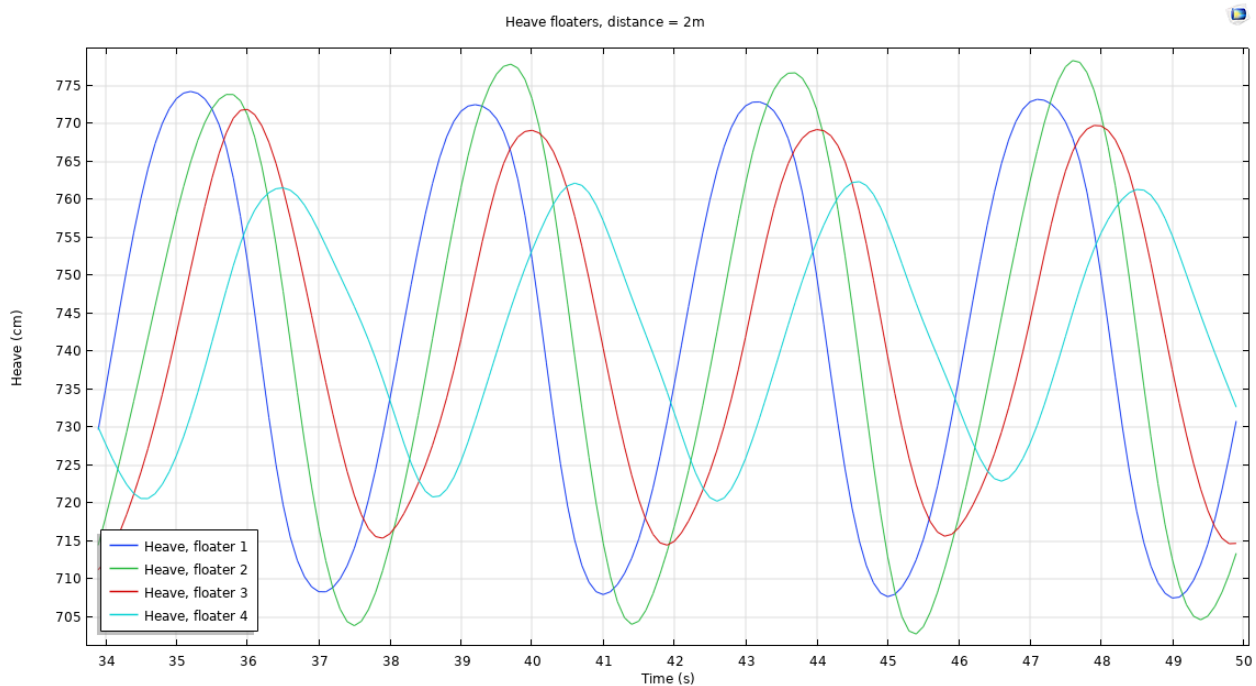
Figure 77: Heave of the different floaters, distance = 2m, for t=34s until t=50s.

As one can see, the results are a lot more consistent compared to case 7. The main reason for this is that the length of the connection is larger, where the floaters have less impact on each other. Not only are the peaks of the graphs very consistent, but the minimum elevation is consistent as well. The motion response is presented in Table 28 below.

	Displacement (heave)	Response amplitude
Floater 1	65.243 [cm]	0.870
Floater 2	73.150 [cm]	0.975
Floater 3	54.849 [cm]	0.731
Floater 4	40.537 [cm]	0.540
Average	58.445 [cm]	0.780

Table 28: Motion response with respect to the original wave, distance = 2m.

From the graph and the motion response, one can see that the second floater performs best, followed by the first, third and fourth floater, respectively. This is in line with the results from the fixed floaters.

8.2   Results for connected conical floater array (case 10, 11 and 12)

In this section, the results are presented for the conical floaters including multibody dynamics. As shown before, the connections are placed near the top of the conical floaters. Please note that only three floaters are present since COMSOL was not able to converge with four floaters, due to the complexity of the model.

8.2.1   Results for a connected conical floater array, case 10

The results for case 10 are presented below. Please note that the time on the x-axis differs from the previous cases, the simulation was stopped at 42 seconds due to computational time and convergence issues. This does not decrease the accuracy of the results, since the system is in a quasi-steady state already.
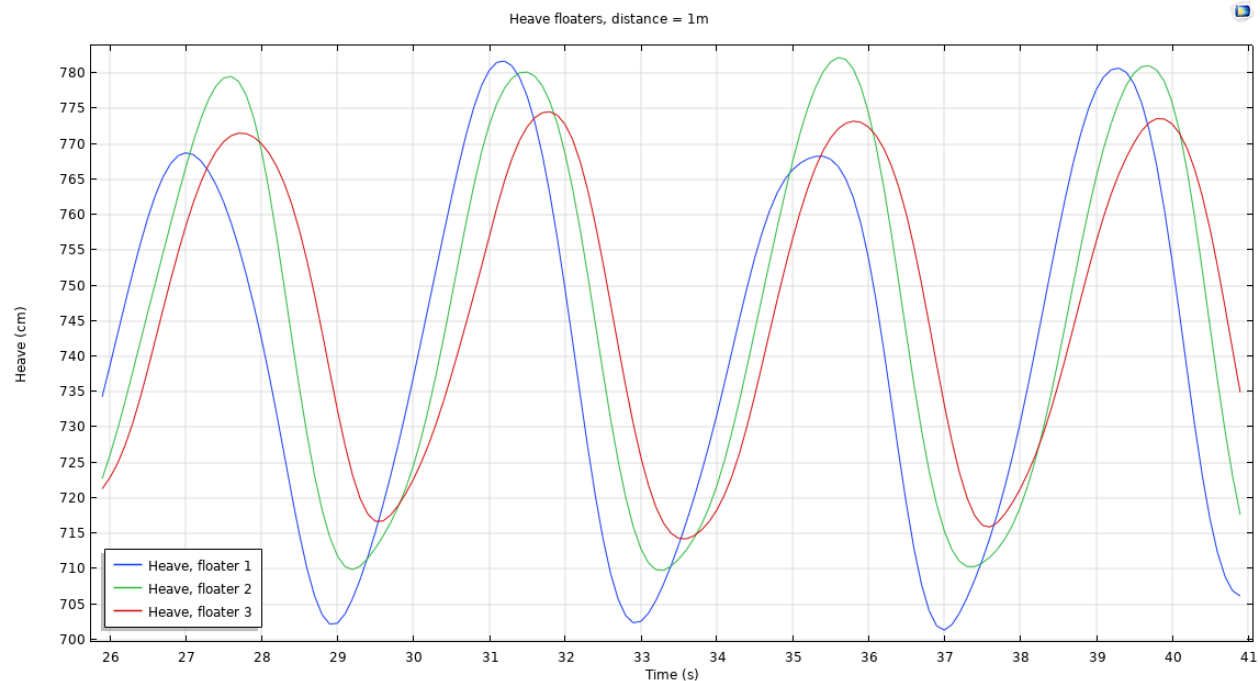
Figure 78: Heave of the different floaters, distance = 1m, for t=26s until t=41s.

Something interesting is the change in profile for the first floater, where for each period the heave changes from a higher elevation to a lower elevation. The main reason for this is the rotation of the neighboring floaters. During counterclockwise rotation, the first floater is pushed down a bit by the other floaters, in the same manner as in case 8; for clockwise rotation, the floater is pushed up a bit. The rotation changes each period, generating an interesting trend in the elevation. As with case 8, the change is caused by the fact that the first floater is fixed in surge, where the rotations are more influential since the first floater cannot

80

move in surge. Because the first floater is fixed in surge, the only option to deal with the displacement is rotation.

	Displacement (heave)	Response amplitude
Floater 1	72.894 [cm]	0.972
Floater 2	70.747[cm]	0.943
Floater 3	57.611[cm]	0.768
Average	67.084 [cm]	0.894

Table 29: Motion response with respect to the original wave, distance = 1m.

The motion response is not that useful for the first floater, since it is an average of two extremes. For the counterclockwise rotation, peak 1 and 3, the displacement is 66.503 cm and for the second and fourth peak, the displacement is 79.363 cm, which results in a motion response of 0.887 and 1.058 respectively. In general, the motion response is not in line with the other results, where the first floater has the highest elevation followed by the second and third floater.

8.2.2   Results for a connected conical floater array, case 11

The results for the heave of case 11 is presented below in Figure 79 and Table 30.
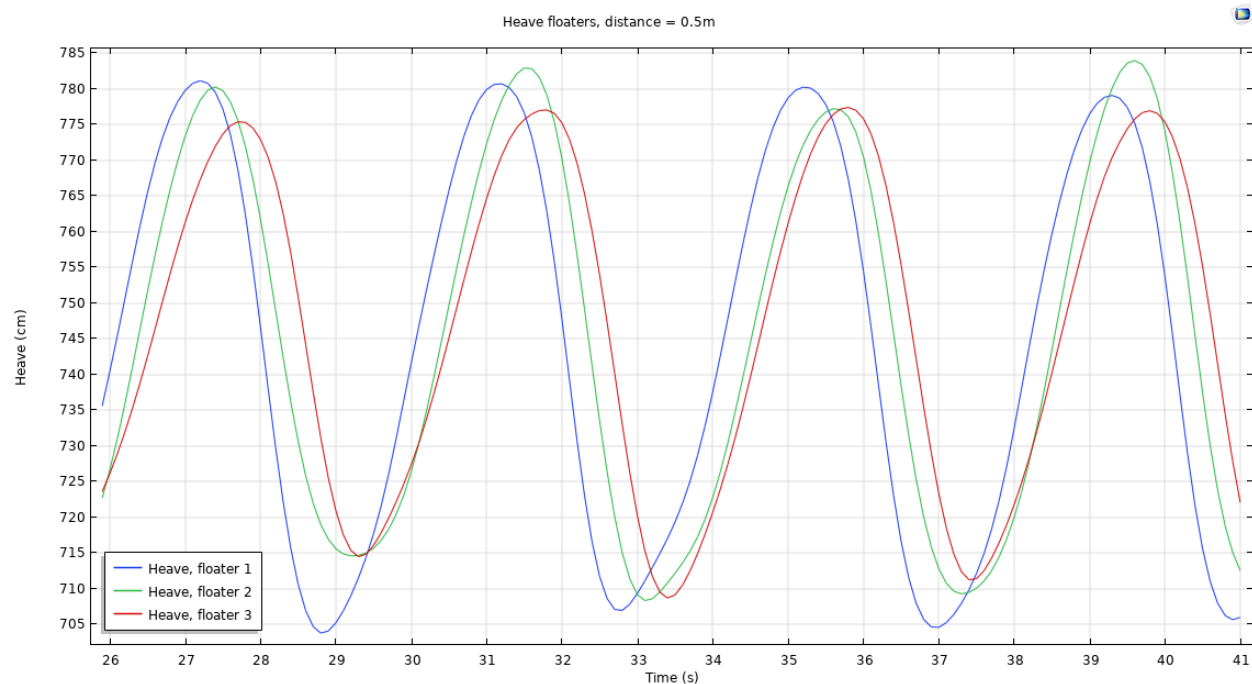
Figure 79: Heave of the different floaters, distance = 0.5m, from t=26s until t=42s.

In case 11, it seems that the heave of the first floater is more constant over different periods. On the other hand, there is some inconsistency for the second floater, caused by the rotation. For case 8, which had the same settings but a rectangular floater, there was contact between the floaters, which is not not case for the conical floaters. The main reason is the shape of the floater and a different connection point.

	Displacement (heave)	Response amplitude
Floater 1	75.170 [cm]	1.002
Floater 2	70.342 [cm]	0.939
Floater 3	65.211[cm]	0.869
Average	70.241 [cm]	0.937

Table 30: Motion response with respect to the original wave, distance = 1m.

The overall motion response is quite high in this case, where the first floater has the largest displacement, which is in contrast to the fixed situation, where the second floater has the largest displacement. The motions response is larger than 1, implying that the heave of the floater is larger than the original wave. This is explained by the radiation and interactions of the connected floaters.

8.2.3 Results for a connected conical floater array, case 12

For case 12, the results are presented in Figure 80 and Table 31.
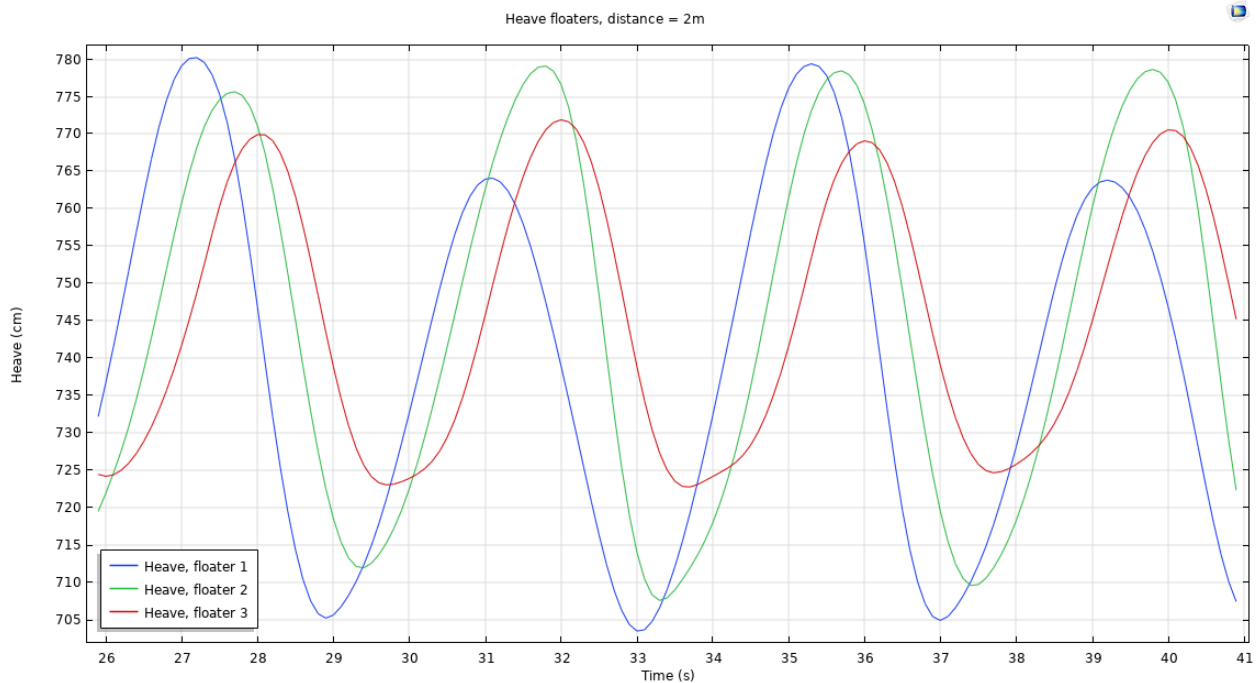
Figure 80: Heave of the different floaters, distance = 2m, for t=26s until t=42s.

For case 12, the same trend occurs compared to case 10, where the displacement of the first floater is dependent on the period due to the rotation and interactions of the floaters. For the third floater, the curve seems to be a bit flattened near the minimum heave. The main reason for this is that the floater rotates itself instead of moving in heave, due to the motion of the second floater, which is pushed to the right. As with the fixed cases, the flattening of the curves is also partially due to the conical shape of the floaters.

	Displacement (heave)	Response amplitude
Floater 1	67.390 [cm]	0.899
Floater 2	68.303[cm]	0.911
Floater 3	46.899[cm]	0.625
Average	60.864 [cm]	0.812

Table 31: Motion response with respect to the original wave, distance = 2m.

For case 12, the second floater has the highest heave, followed by the first floater. The third floater performs the worst, as expected.

8.3   Comparison of connected floater arrays

In this section, a comparison is made between the different floater arrays, cases 7-12, including multibody dynamics. The average motion response for the different configurations is shown below.

	Average displacement (heave)
Case 7	65.267 [cm]
Case 8	N/A
Case 9	58.445 [cm]
Case 10	67.084 [cm]
Case 11	70.241 [cm]
Case 12	60.864 [cm]

Table 32: Average displacement in heave for the final 6 cases.

The results for case 8 are not usable, due to the collision of the floaters. For the conical cases, 10, 11 and 12, three floaters were investigated instead of four due to computational problems. From the table, the more dense arrays outperform the less dense arrays, which is in line with the fixed cases.

For the connected floaters, the variance is smaller for the more dense array, as was the case for the fixed floaters. The results are less constant, and there is a larger variance in a single floaters motion during different periods.

8.3.1   Comparison of fixed arrays versus connected arrays

An effect of the inclusion of the connections between the floaters is that the array performs slightly worse on average. The only cases that can be compared are case 1 with case 7 and case 3 with case 9. For the conical floaters, only three floaters are present due to numerical complications and cannot be compared. The results are shown in the table below.

	Average displacement (heave)		Average displacement (heave)
Case 1	66.303 [cm]	Case 7	65.267 [cm]
Case 3	59.874 [cm]	Case 9	58.445 [cm]

Table 33: Final results for the relevant cases.

In general, the mechanical interconnections decrease the heave and therefore their performance is slightly lower compared to the fixed cases. This is only valid for the rectangular floaters since it is not possible to make a comparison for the conical floaters due to the reduction in the number of floaters. This is in line with theory, as some of the energy is lost to both surge displacement and rotation of floaters. The interaction might also have some positive effects, for example when one of the floaters is in a higher elevation, pulling up the other floaters. An example is that the variance of the first and the last floater are lower when interactions are included. The reason for this is that the first and second floater's heave is supported by the middle floaters, 'pulling' the floaters upwards. Overall, the variance is lower for the connected floater arrays, though the difference is not as large as expected. In general, the interactions between the floaters have a negative effect on heave.

For the fixed case, the floaters are pushed upwards more, since they have to are not able to move in surge. For the multibody dynamics, the floater can compensate for some of the incoming waves with surge motions, which might explain why the heave is larger for the fixed arrays. In short, if the floaters are fixed, the flow

is forced upon the floater, where the connected arrays can move in surge slightly.

For the conical floaters, the results cannot be compared directly. The main reason for this is that the number of floaters for the conical case has been reduced to three floaters. The result of the comparison is that the connected array performs a lot better. The reason for this is that there are only three floaters present.

8.4   Motion (surge, pitch) of rectangular floater arrays

In this chapter, the surge and pitch motion of the floater array is discussed, including the rotation and displacement in the surge direction. Case 7 (rectangular) and 10 (conical) will be used to illustrate the interactions of the bodies. These cases are selected since the effect of the connections is larger for smaller distances. Unfortunately, for a distance of 0.5 meters, there is no data available for the connected arrays, due to collision. Please note that the displacement in surge is measured at the center of mass. In the first section, the surge of the rectangular floater array is discussed. In the second section, the pitch (rotation) of the rectangular floater array is discussed. In the third and fourth sections, the conical floater surge and pitch are discussed, respectively.

8.4.1   Motion rectangular floater array, surge.

The surge of the connected floaters (case 7) is shown in Figure 81.
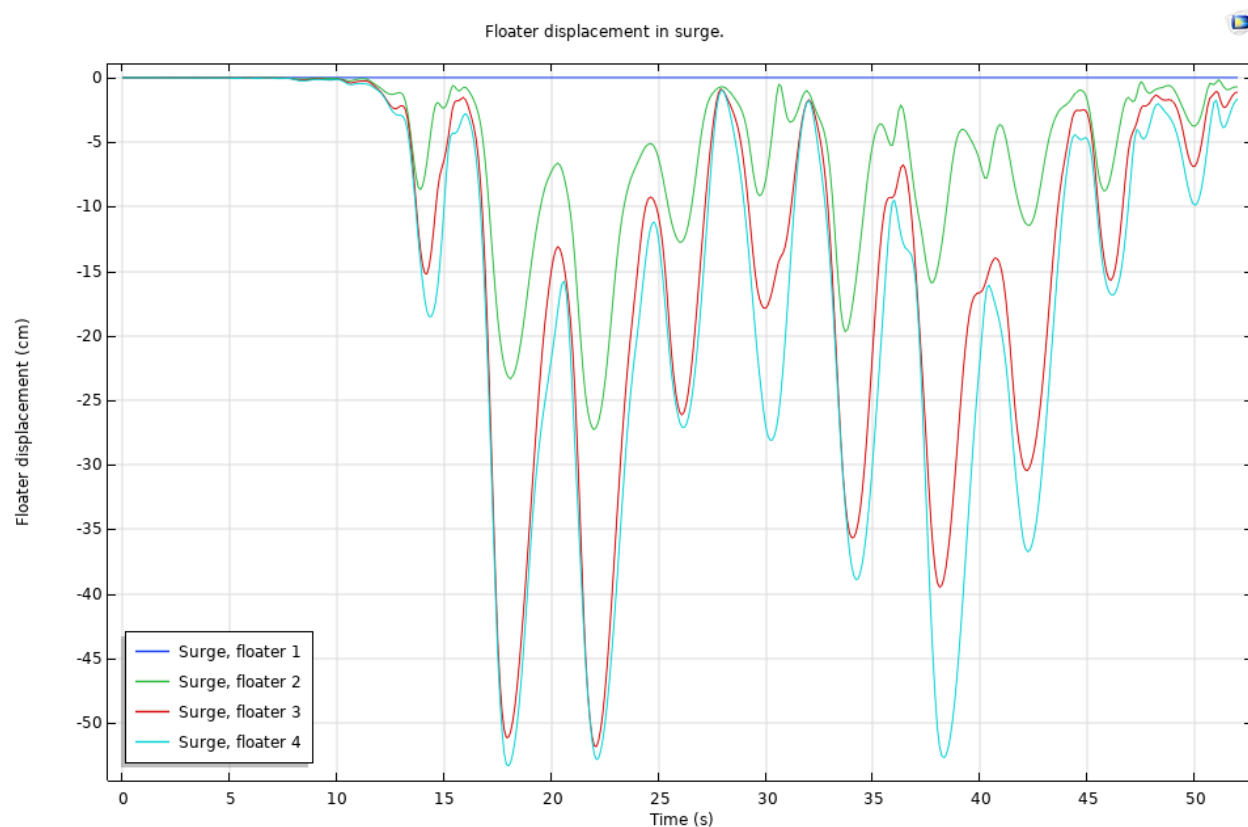
Figure 81: Surge of the floaters for case 7, with respect to the initial position.

The first floater is fixed and therefore does not move. In the initial condition, the position of the floaters is at maximum, since the straight formation results in the 'longest' array. In the graph, one can see that the floater displacement is never positive since the displacement is measured with respect to the initial position. Besides surge, the rotation should be zero as well to achieve zero displacement. For the floaters, the surge

direction is dependent on the period of the wave, since the lowest and highest point in the graph occurs every 4 seconds. This is explained by the flow field, which changes direction twice per period.

The displacement with respect to the initial position is smallest during the crest of the wave, where the flow field is in the same direction as the wave propagation. This causes the floater array to be stretched, where the distance between the floaters is the largest. The largest displacement with respect to the initial position, where the floaters are closest to each other occurs during the trough of the wave, since the flow field is opposite to the wave propagation, 'compressing' the floater array. During the trough, the third and fourth floaters push towards to the first floater, shown in Figure 82.
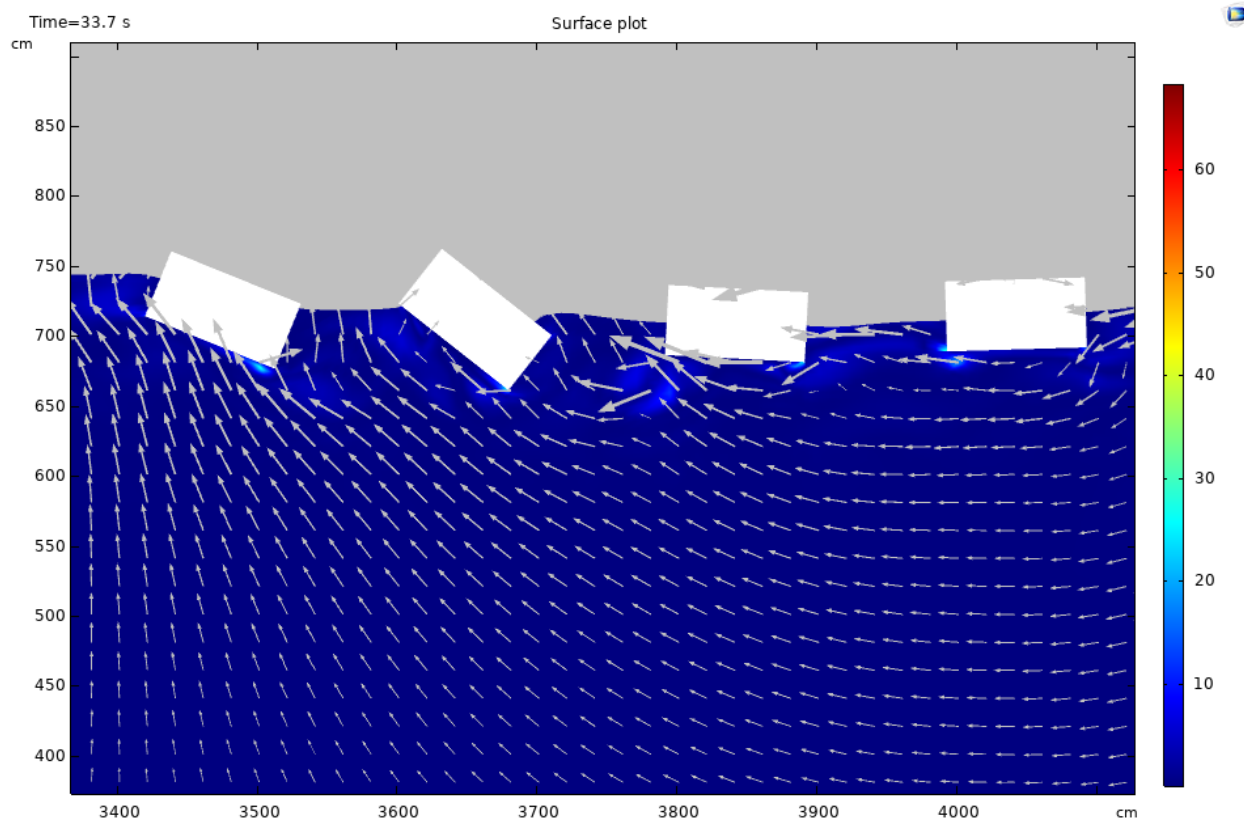
Figure 82: Floater positions during the trough, where floater 3 and 4 push towards the first floater, resulting in rotation of the second floater. This effect occurs every period, during the trough of the wave, where the flow field is opposite to the wave propagation.

This statement is supported by the graph as well, where the third and fourth floater have the largest displacement towards the first floater, causing the second floater to 'deal' with the shorter distance, causing rotation. Please note that this effect is large due to the fact that the model is in 2D. In a 3D case, the flow is able to go around the floaters instead of pushing them towards other floaters. Secondly, in a real situation, the first floater is not fixed and is able to move slightly.

8.4.2   Motion of a rectangular floater array, pitch.

First, the effect of rotation on displacement will be discussed. To obtain insight into the effect of rotation on the displacement, a model was constructed with 2 floaters, to see the interaction of two floaters. If plotted with four floaters, noise is added to the signal due to the interactions of the other floaters. In the example, the rotation of the first floater is compared to the displacement of the second floater.

In Figure 83, the rotation matrix (xy) of the first floater is plotted on the left axis and the surge of the second floater on the right axis. For the rotation matrix, a positive change implies a counterclockwise rotation and a negative change clockwise rotation. If the rotation in the xy plane is zero, the floater is in its original orientation. For the displacement in the surge direction, the values are with respect to the original position.
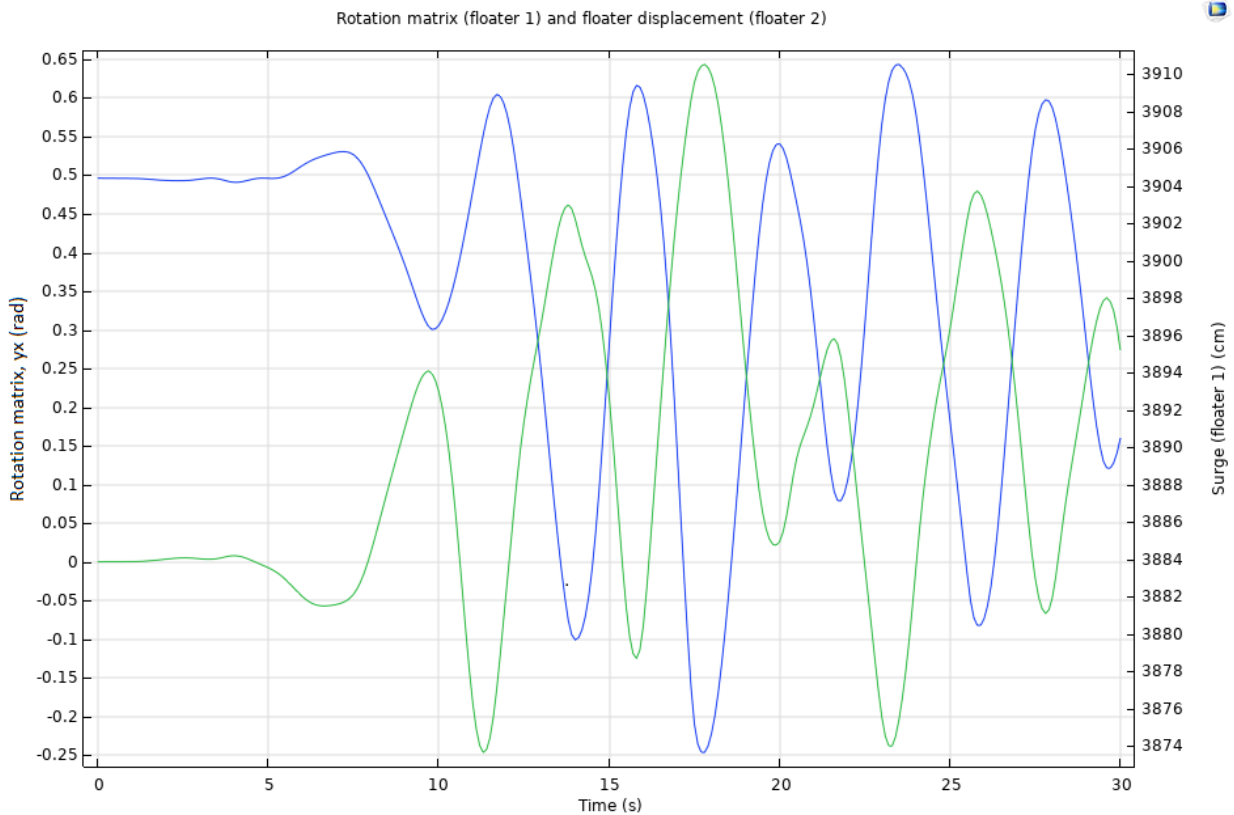
Figure 83: Rotation of the first floater compared to the displacement of the second floater.

In Figure 83, the effect of rotation on displacement is clear. The rotation of the first floater causes a change in the x-position of the connection point, pulling the second floater towards it to ensure that the connection distance is kept.

For an array with 4 floaters, the trend was the same, but a bit harder to identify due to the noise added by the interactions of multiple floaters.

8.4.3   Motion of a conical floater array, surge

The displacement for the conical floaters is a bit more complex compared to the rectangular case. The main reason is that the floaters are connected near the top. One effect of this is that the floater array can 'stretch' longer compared to the initial position, Since the connection points are not at the same height as the rotation points. This implies that, due to rotation, the array can increase in length, since the motion is measured at the center of mass (also center of rotation). In Figure 86 below, the displacement of the floaters is presented in the same manner as in the previous chapter.
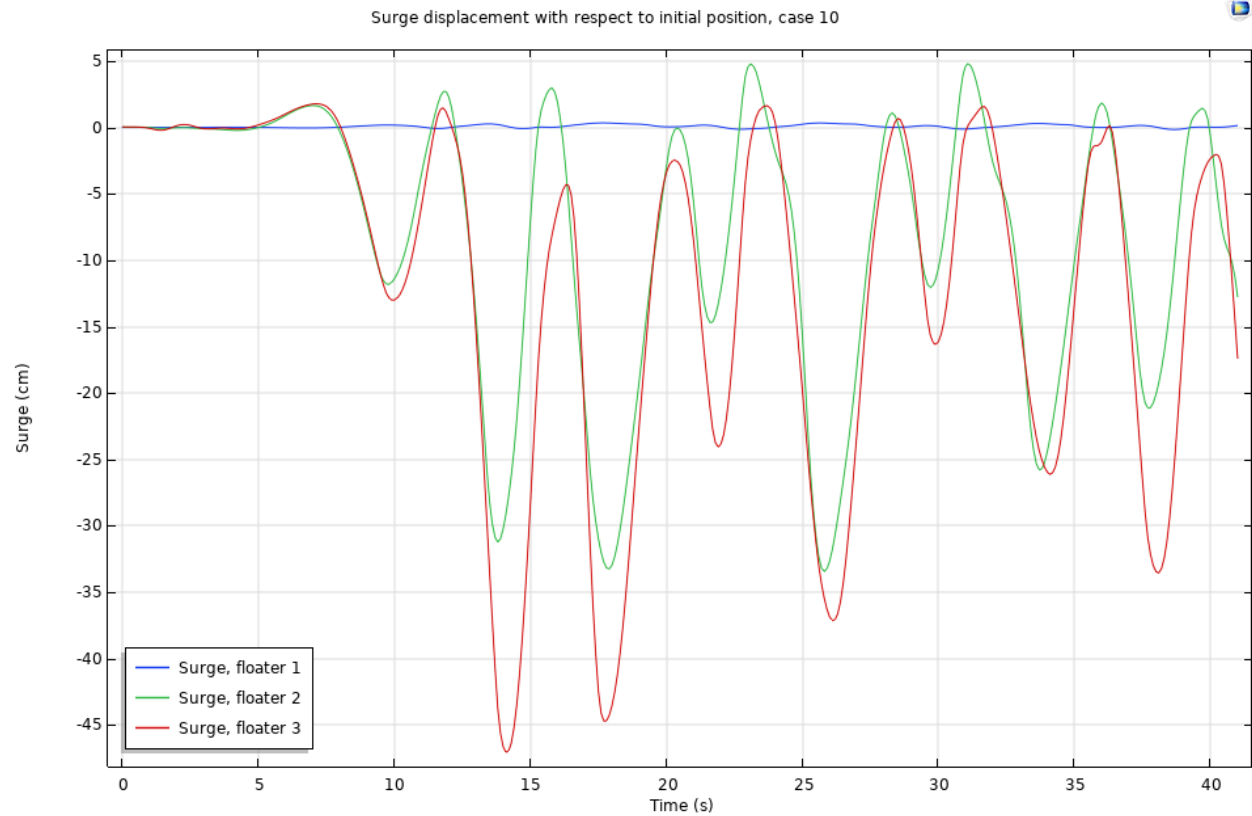
Figure 84: Surge motion of the floaters with respect to the initial position.

As one can see, the displacement is indeed positive on some occasions, for example at 23.3s. At this moment, the array is 'stretched' due to the direction of the flow field, which is in line with the wave propagation. The first floater is rotated clockwise, whilst the last floater is rotated counterclockwise, creating the largest distance. The main reason for the positive displacement is that the distance is measured from the center of mass of the floater.
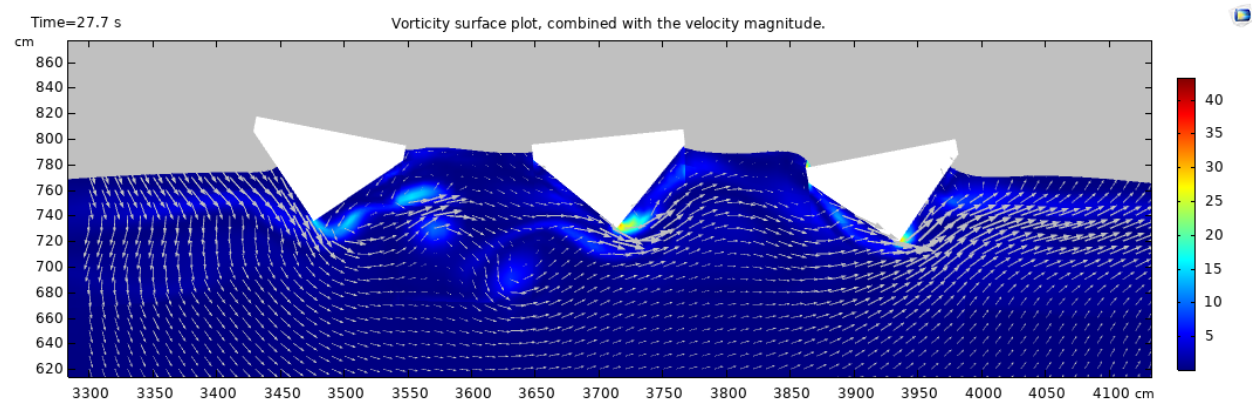
Figure 85: Maximal displacement, where the array is 'stretched' due to the direction of the flow field.

As with the rectangular floaters, if the flow direction is opposite with respect to the wave propagation, the array is 'compressed', which occurs at 27.7s, for example, taken from the graph. As one would expect, the floaters are rotated in the opposite direction, to form the smallest distance.

87
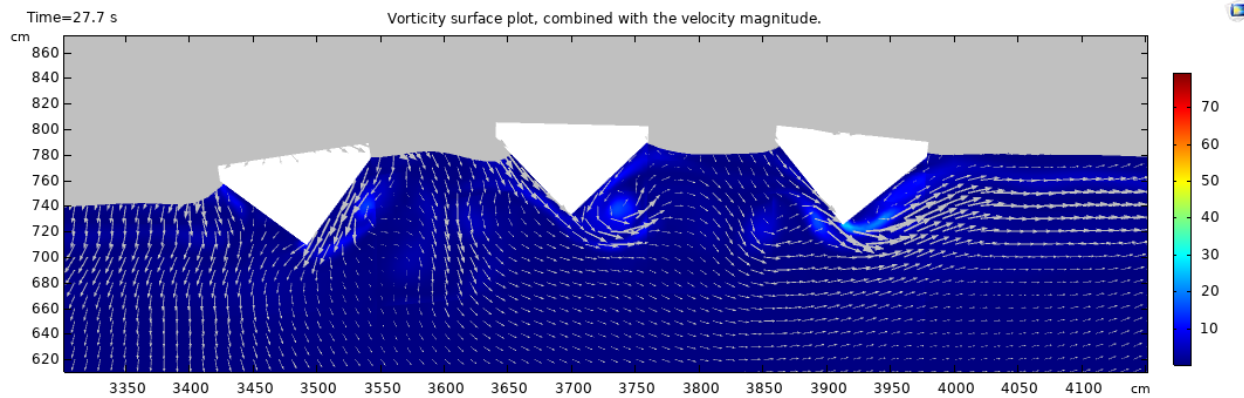
Figure 86: Minimum displacement, where the array is 'compressed' due to the direction of the flow field.

In short, because the connection points for the conical floater are not at the same height as the center of rotation, the array can 'stretch' longer with respect to its initial position. For the rectangular floaters, this is not the case, since the connection points are on the same height as the centers of rotation.

9   Flow field analysis

In the following section, the flow field is analyzed for the different situations. The flow fields are presented by the gray arrow representing both the velocity magnitude and direction. The surface plot represents the vorticity of the fluid. Some of the subjects that will be discussed are the disturbance of the flow and the effect of the motions of floaters on the flow. Finally, the different arrays and different shapes are discussed. Please keep in mind that the model is 2D and therefore the flow has to pass above or below the floater and cannot go around the floater since a third dimension is not included. This implies that the fluid is forced to act upon the object.

9.1   Disturbance of the flow

There are a few ways in which the floater affects the flow field. One of the main effects is the disturbance of the flow because of an object in the flow regime.

The main effect of the floater on the flow field occurs when the incoming fluid meets the object. The flow is forced around the object, resulting in a larger velocity magnitude around the object, due to Bernoulli's law, where a smaller area increases the flow velocity. The reduction in the area for the flow is caused by the object. As one can see, the increase in velocity around the floater causes vorticity, where the fluid's particles move in a rotational trajectory. The vorticity can be seen in Figure 87, at the lower-left corner of the floaters.
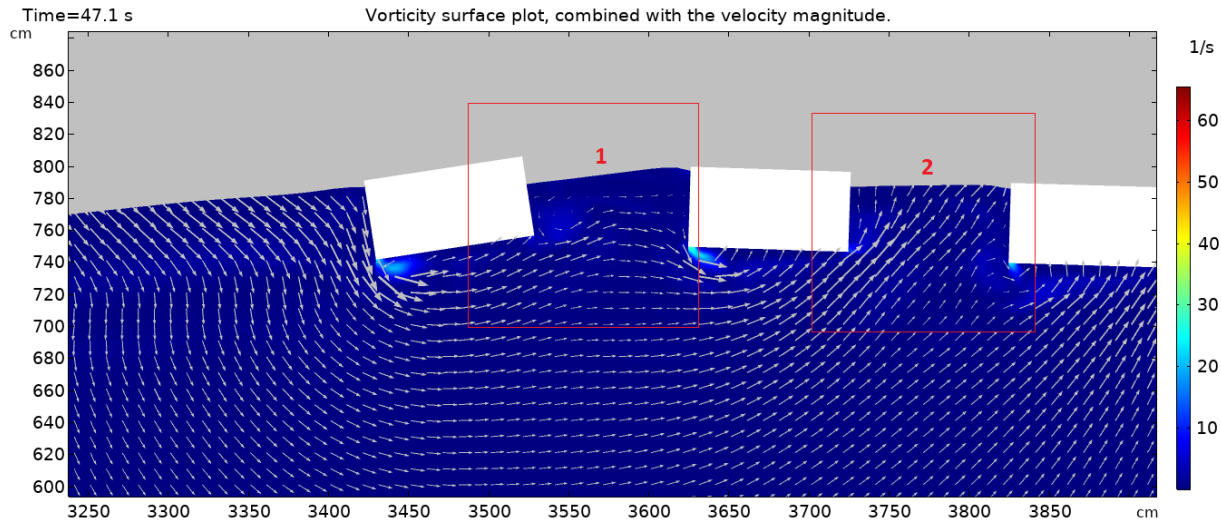
Figure 87: Flow disturbance for two different regions for case 1. The first three floaters are presented.

In Figure 87, two regions are identified to explain the difference in the flow field behind the floaters. The reason for the difference in the regions is due to the circular motion of the particles, where the velocity field rotates 360 degrees every period. In the first region, the flow is disturbed quite a lot. Indicators for this are inconsistencies with the rest of the flow field, such as velocity magnitudes in a circular pattern and small velocity magnitudes. This is caused by the disturbance of the incoming flow due to the object, where the fluid is forced underneath the floater, causing an increase in velocity due to pressure. Because of the re-direction of the velocity, little energy is transferred to the area in between the floaters because of the direction of the velocity profile. For the second region, a case is presented where the flow field is not disturbed. In the second region, the direction of the velocity profile is different from the first region since the floater is not directly located in the direction of the flow. The result is that the energy in region two is larger.

Whether the regions between the floaters have a high-velocity profile or not is therefore dependent on the current direction of the flow, which rotates by 360 degrees every period. If the velocity profile is larger in a region, the area has a higher local energy density.

As discussed before, the increase in energy density might explain some of the floater behavior, where regions with a high energy density result in a larger floater displacement. This is mainly caused by the local surface elevation since the water is trapped between the floaters due to the 2D approach. The rotation of floaters is also magnified by the difference in high and low energy dense areas, due to a difference in local surface elevation.

9.2   Effect of the motion of floaters on the flow

Besides the floater acting as an object in a flow, the motion of the floaters also has an impact on the flow. The up and downwards motions have the highest impact on the flow; the flow field during the upwards motion is presented in Figure 88.
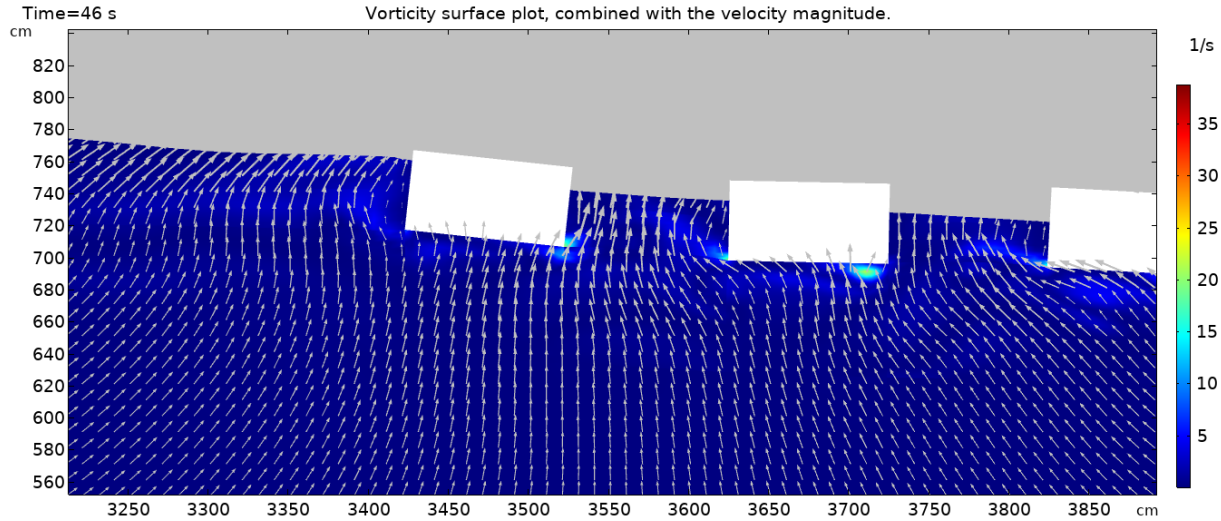
Figure 88: Flow disturbance for a upwards motion of the floater in case 1 for t = 46s. The first three floaters are presented.

During the upwards motion of the floater, the disturbance of the flow is small, since the motion of the floater is in line with the direction of the flow field. The only disturbance is some small increase in vorticity due to the corners of the floater, where the velocity magnitude of the fluid is larger than the upwards velocity of the floater. For the downwards motion of the floater, the flow field is presented in Figure 89. As an example, the region between the first two floaters has a high energy density, since the velocity is quite large.
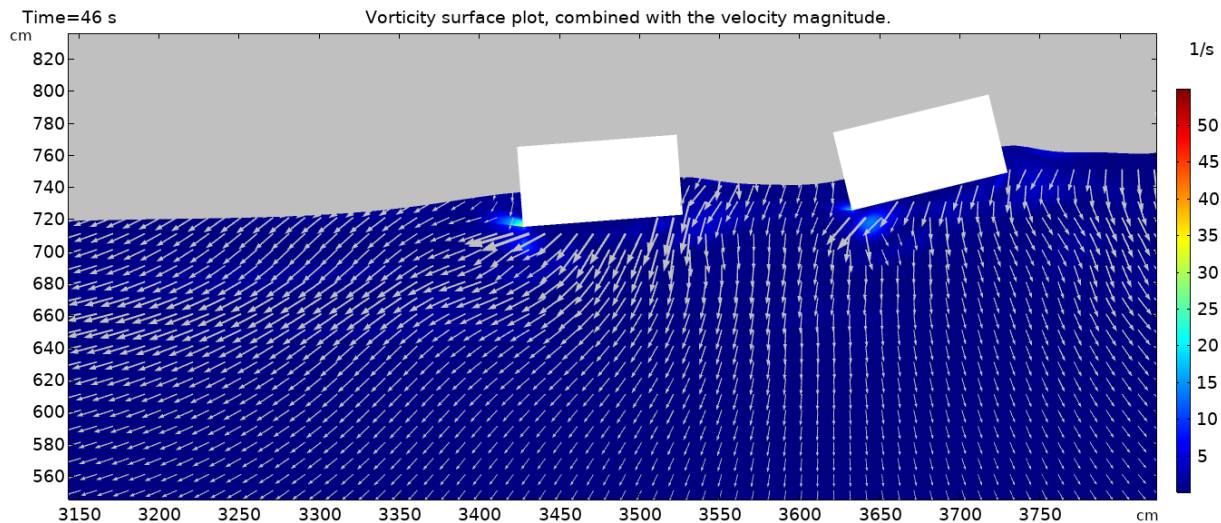
Figure 89: Flow disturbance for a downwards motion of the floater in case 1 for t = 46s. The first two floaters are presented.

For the downwards motion, there is little influence of the floater on the flow. The main reason for this is again the motion of the floater which is aligned with the direction of the flow field. One effect that can be seen is that the velocity around the floater is larger compared to rest of the field. This is caused by the inertial force of the floater, which is 'pulled' down, accelerating the fluid around the floater. For this specific floater, the downwards velocity is larger compared to the flow field, causing the acceleration.

Another effect that is important is that the flow field is quite dominant. What is meant is that the flow is

able to adjust the disturbances quite quickly. This implies that the effects of the disturbance will not really increase over period, since the flow adjusts quite quickly.

9.3   Rotation of the floaters

The floaters tend to rotate quite a lot, partially due to the 2D approach. The main reason is that all the incoming flow has to be either absorbed in the form of elevation of the floater, redirected beneath the floater or change direction completely. In a 3D model, the flow would also be able to go around the floater. The rotation of the floaters can partially be described by the flow of the fluid. In the figure below, an example is given for a rectangular floater, where the time is 46.6, 46.7, 46.8 and 46.9, respectively. Floater 1 of case 1 is presented.
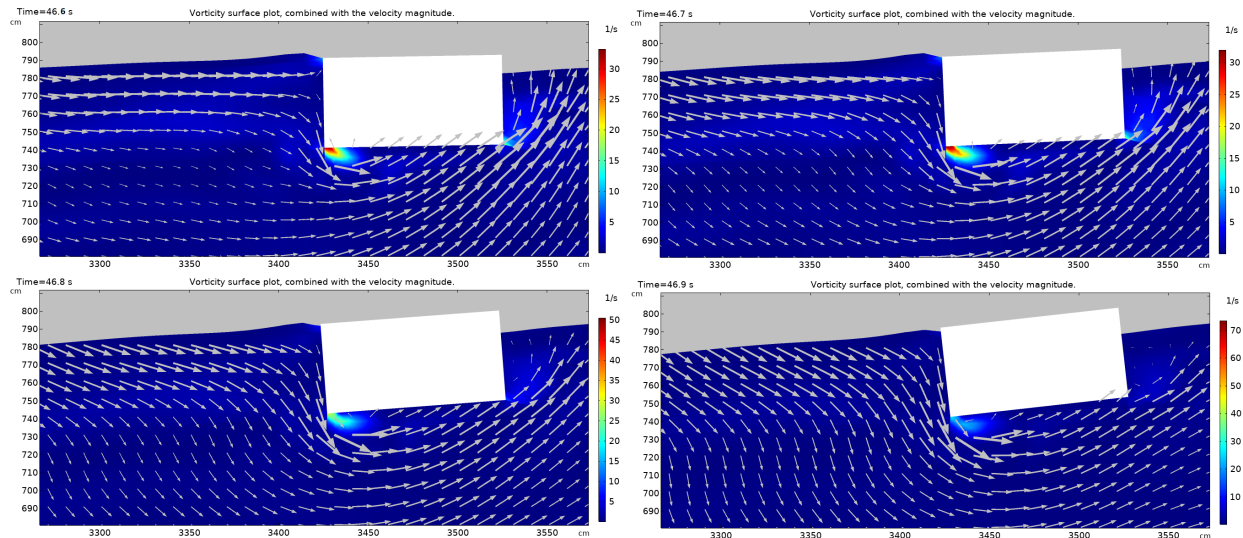
Figure 90: The flow field around the first rectangular floater for the first case, t = 46.6, 46.7, 46.8 and 46.9s.

In the top left figure, one can see that the direction of the flow is directed towards the floater, which is right before the maximum elevation of the floater. The vorticity is quite high near the corner of the floater since the flow is re-directed beneath the floater, creating vorticity. Because of this incoming flow and redirection, the lower side of the floater is 'pushed' to the right, resulting in a counterclockwise rotation. In the next two figures (top right and bottom left), the vorticity is still rather high because of the redirection of the flow. In the final figure (bottom right) the result is a slightly tilted floater, with high velocities near the bottom left corner and a low-velocity field behind the floater.

9.4   Poor performance of the fourth floater

As mentioned before, the last floater has the worst performance for all configurations, with a significant difference. The main reason for this is that the energy density is lower, due to the energy extraction of previous floaters.

There is another effect that influences the heave of the last floater. Which is explained in the next chapter, the flow is forced to either pass above or below the floater. Figure 91 is used to illustrate the effect.

Figure 91: The flow field for the first case around the first and second floater, t = 47.1s.

In Figure 91, the flow field is presented for the third and last floater, for a rectangular floater with a distance of 1 meter. As one can see, the flow field velocity between the floaters is not hindered by the floaters. The velocity is rather high near the surface, which causes a 'local' surface elevation since the water is trapped between the two floaters. Because of the higher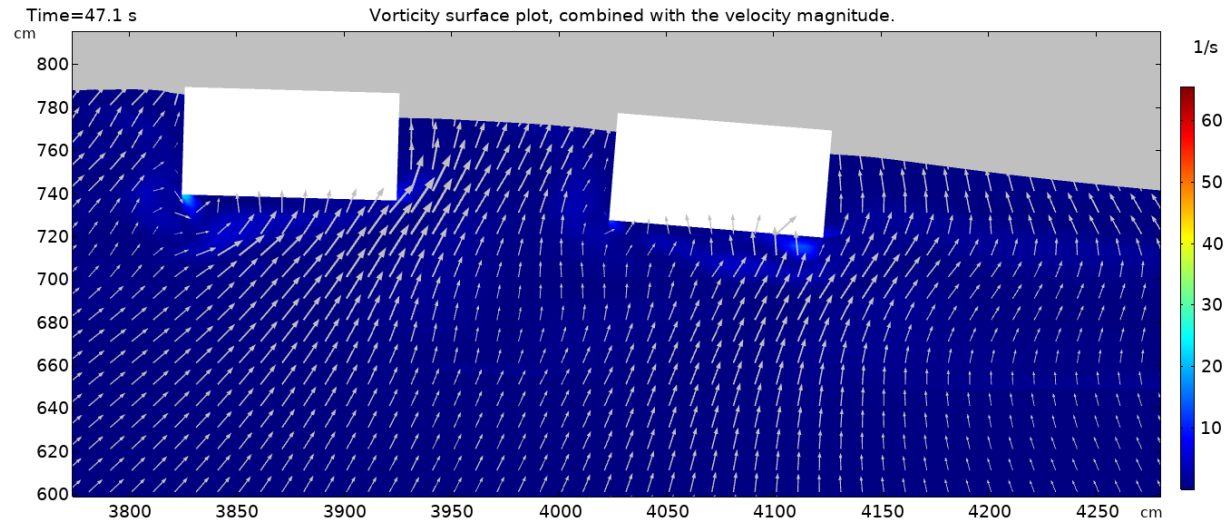 local surface elevation, the total submerged area is larger and therefore the heave displacement will be larger for the third floater. On the other hand, for the last floater, the local surface elevation is only found for the left side. The combination of the low energy available due to extraction of the previous floaters combined with the lack of 'local' surface elevation leads to poor performance. In a 3D environment, this would be different, since the water will not be trapped in between the floaters. The larger the distance between the floaters is, the larger the 'reservoir' is and the less effect it has, which is in line with the results from the different distances.

Besides the local increase in surface elevation due to the direction of the flow field, the radiation effects are also larger due to the 2D approach.

9.5   Differences between floater arrays

The flow field differs for different arrays. An example is the second case, where the velocity is almost 0, as presented in Figure 92. The region between the first and the second floater has barely any velocity. This is due to the small area between the floaters. There are two reasons for this. First, because of the small area, there is no chance for the flow to develop between the floaters, since it cannot be 'reached' by the underlying layers. Secondly, the flow field beneath the floater is perfectly in line with the wave propagation and has no incentive to move upwards.
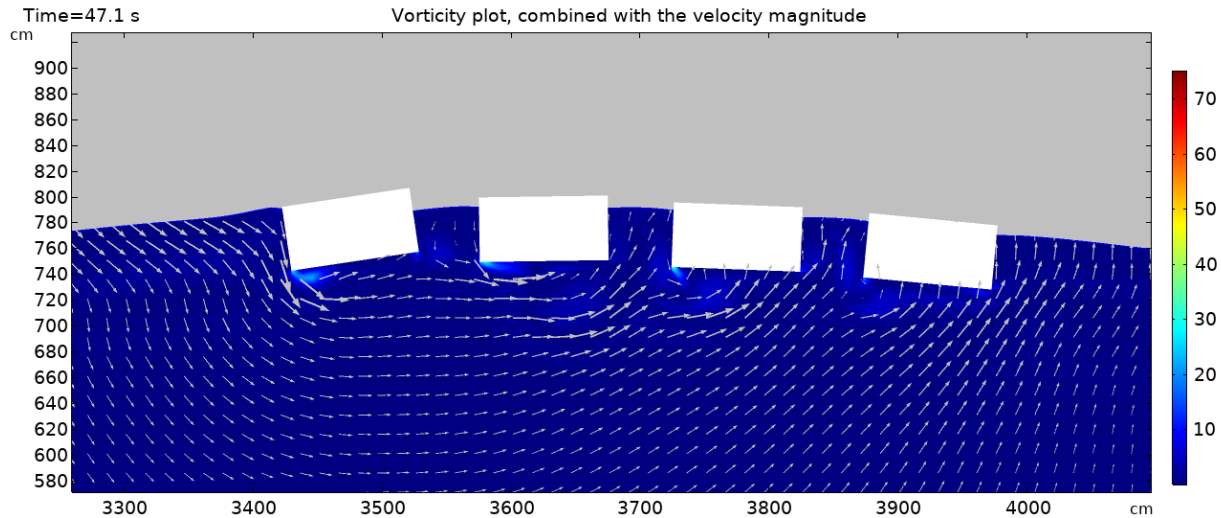
Figure 92: The flow field for case 2, where distance = 0.5 meter, t = 47.1s.

On the contrary, for the third case, with a distance of 2 meters, the flow between the floaters is in line with the rest of the flow field. There is also less rotation of the flow. The cause for this effect is that the flow has more 'time' to stabilize, since there is more space between the floaters. Besides this, in the lower parts, the velocities' directions are partially upwards, giving the flow an incentive to travel upwards. This can be seen in Figure 93.
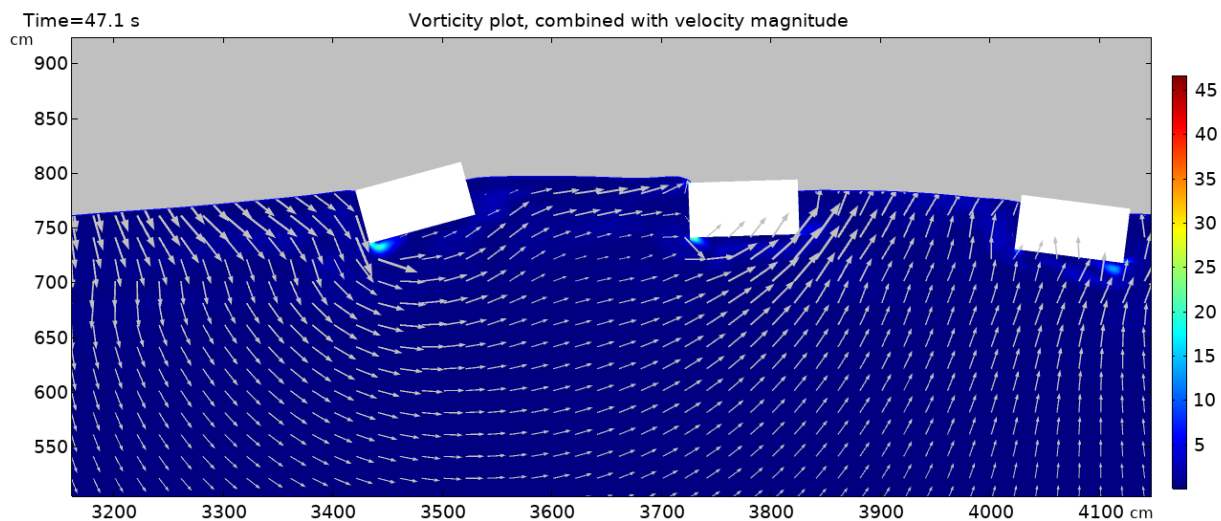
Figure 93: The flow field for case 3, where distance = 2 meter, t = 47.1s for the first three floaters.

In short, for case 2, there is little space but the flow is not trapped in the space between the floaters as much as in case 1. For case 3, there is enough space for the flow to adjust to the original pattern.

9.6   Effect of the conical shape on the flow field

In this section, the conical shape is investigated, to analyze the effect on the flow and compare it to the rectangular floater. Please note that the conical floaters have a lot more rotation compared to the rectangular floaters, due to a less stable geometry. The idea for this geometry is that the flow will not 'bump' into the floater, as is the case with the rectangular floater, but the sloping sides help the floater to deflect the flow

downwards, causing an upwards motion for the floater. Besides the upwards motion, the incoming flow is no longer perpendicular to the floater. This reduces the direct impact of the flow on the floater. In Figure 94, the flow field is presented for an incident wave.
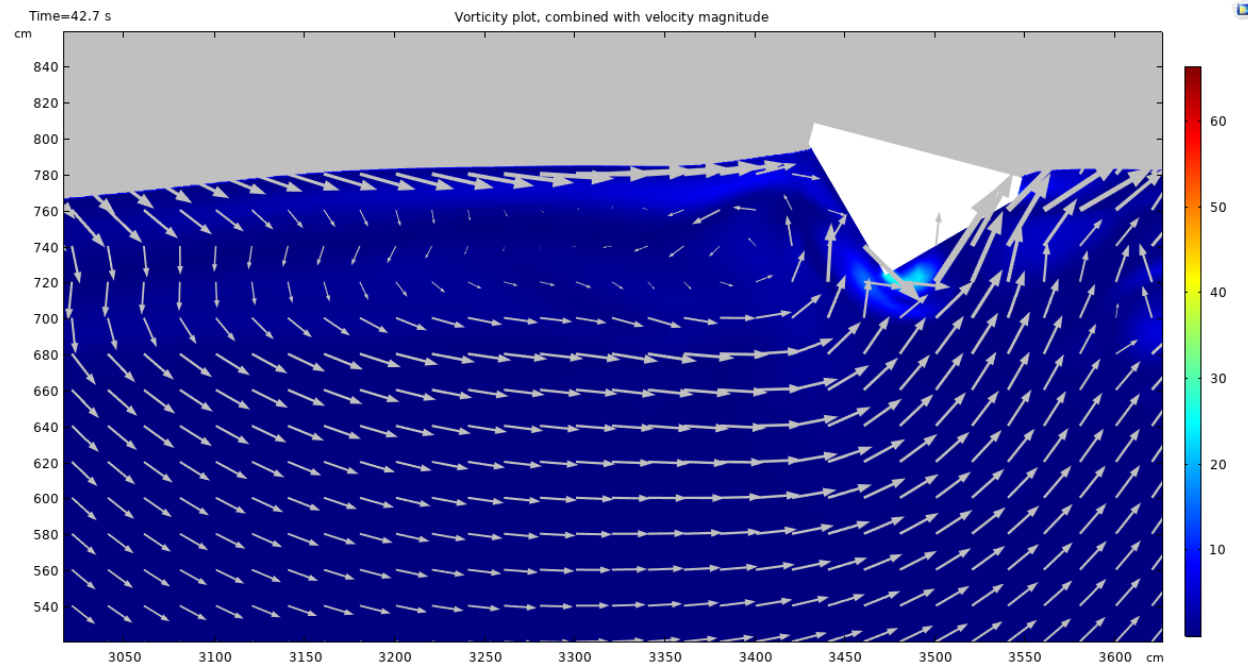
Figure 94: The flow field for case 4, t = 44.2 s.

The behavior of the flow field is quite different from that of the rectangular floaters. For the rectangular floater, the flow arrives and is redirected beneath the floater, causing an increase in velocity and some vorticity. For the conical floater, the flow is disturbed before it reaches the floater. This can be seen by the inconsistent direction of the velocity magnitude and the rotation of the flow left of the floater. This disturbed, low-velocity field is one of the reasons for the rotation, where on the right side of the floater the velocity is still high, causing a counterclockwise rotation.
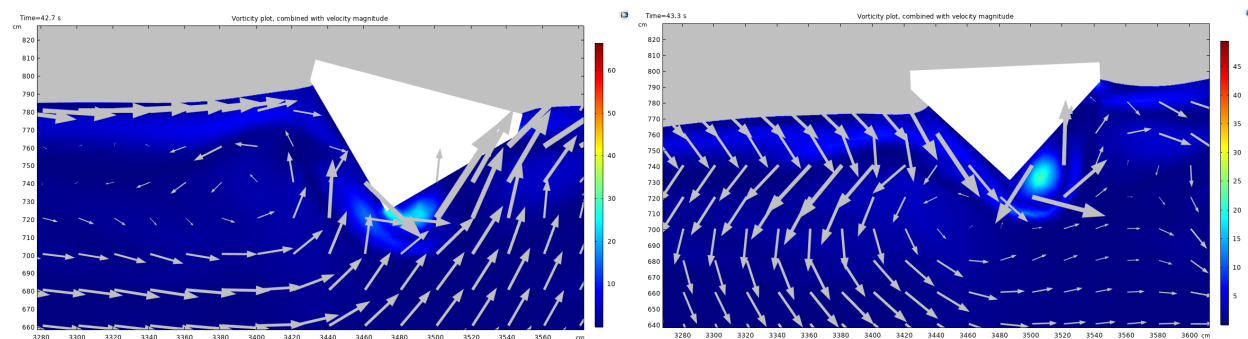
Figure 95: The flow field for case 4, rotation of the first floater due to the incoming flow.

In Figure 95, in the left figure, the flow field during the maximum heave is shown. In the picture on the right, the minimum heave is shown. For the lowest point of the floater (right figure), which is half a period later compared to the left figure, quite some disturbance is found. For the right figure, the disturbance occurs behind the floater instead of before the floater. This is because in the right picture, the direction of the velocity field is opposite to that of the wave propagation. The effect is the same, where the flow is

disturbed quite a lot, but since the direction of the flow is from the other side, the disturbance occurs behind the floater instead of before the floater.

9.6.1   Effect of the motion of the floater on the flow.

For the conical shape, the flow field is a bit different for the up and downwards motion of the floater. For the upwards motion (see Figure 96), the flow seems to split between the two sloping sides. There is some vorticity near the left sides of the floater.
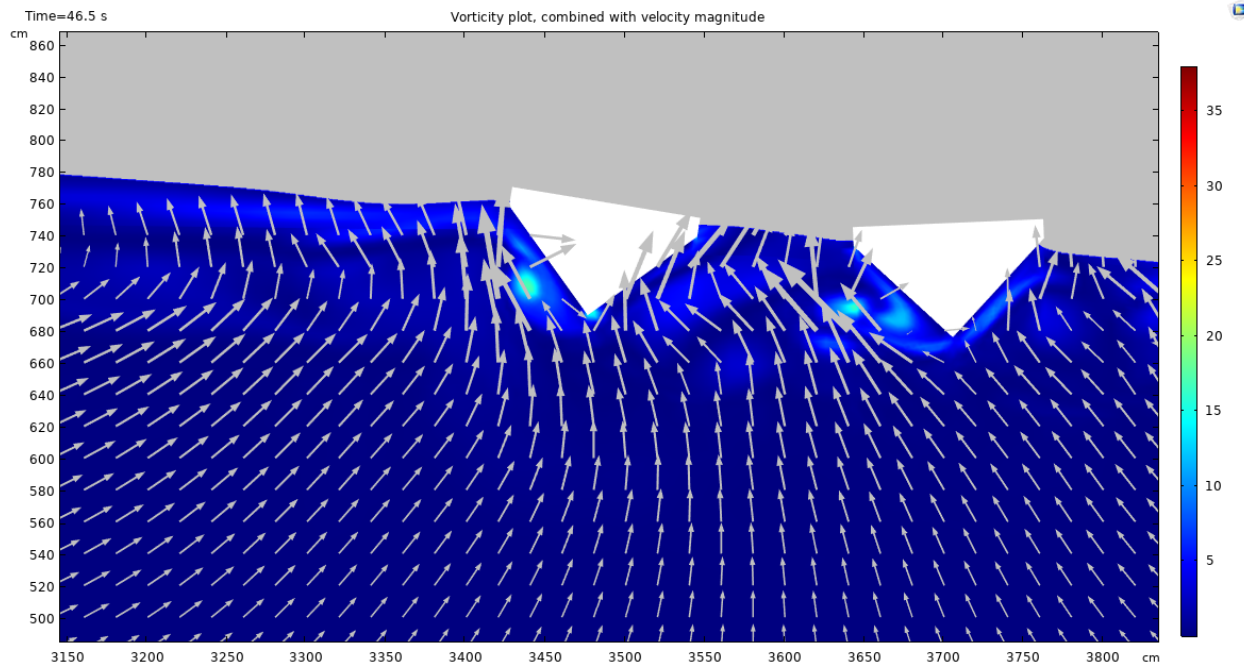
Figure 96: The flow field for case 4, t = 46.5 s

During the downwards motion (see Figure 97), the floater is rotated counterclockwise with respect to the initial position. For every period this rotation is the same. Due to the rotation, the left sloping side pushes on the fluid. Due to the downwards motion, the fluid is pushed away, mostly to the left side. On the right side, the flow is also pushed down but less impactfully since the area is smaller because of the rotation. As with the rectangular floater, the downwards velocity of the floater is larger compared to the flow field, causing radiation.
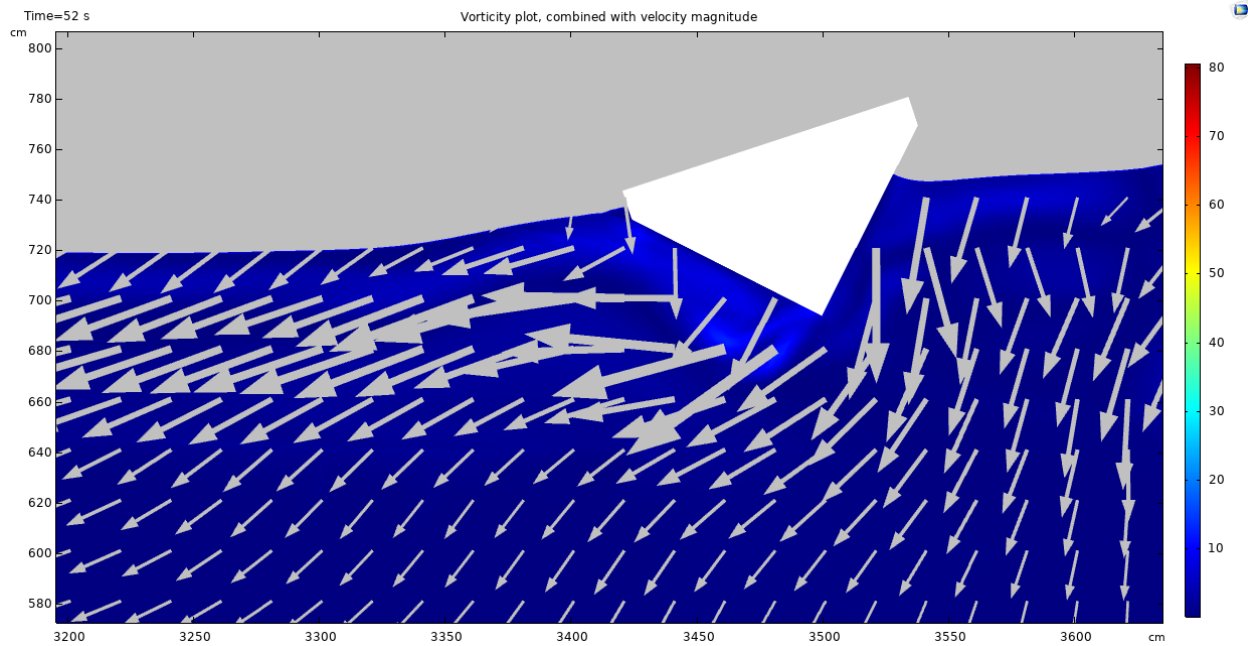
Figure 97: The flow field for case 4, t = 44.2 s. The first floater is presented.

9.7   Flow field after energy extraction

In this section, the flow field after energy extraction is discussed, to obtain some insight into the effects of energy extraction on the flow field. The main reason to investigate this is that multiple arrays will be used, so it might be necessary to include some space to allow the flow to stabilize again.

An example is given for case 1, where some inconsistency can be found in the flow, right after the floater array. The effect of flow disruption after the floater array can be compared to the wake effect of wind turbines.
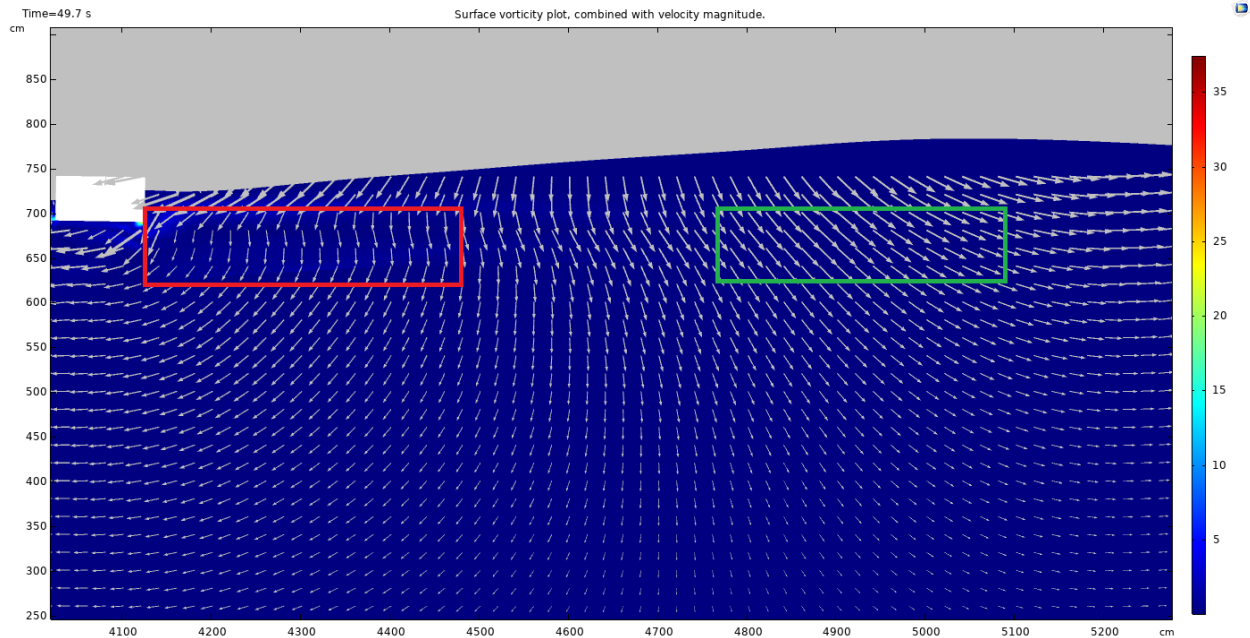
Figure 98: Effect of energy extraction on the flow field.

In the red box of Figure 98, there seems to be some disruption in the flow, caused by the floaters. The direction of the velocity field is not in line with the lower and upper flow field directions. In the green box, which is located about 3 meters behind the red box, the flow seems to have stabilized itself, where the local flow field is in line with the rest of the flow field. A little vorticity can be found as well, which indicates that the motion of the particles is different from the rest of the flow field. The effect seems to be rather small, where the wave returns to its original profile quite quickly.

As was concluded before, the flow field stabilizes quite quickly. This is a nice result, since this also implies that small distances are needed between arrays to allow the flow field to stabilize. The flow field stabilizes quite quickly, which is a beneficial effect and might increase the heave of floaters. Besides this, the radiation effects are larger when the flow is fully developed, compared to disturbed flow. To find the optimal spacing, a balance must be found between the development of the flow and the radiation effects of the floaters.

10   Results on power production

In this chapter, power production will be discussed briefly. A comparison will also be made to A.Bechlenberg's study from 2018, using a time-domain model.

10.1   Comparison to A. Bechlenberg (2018)

The power produced can be calculated with the displacement, damping coefficient and angular velocity of the wave, as mentioned in the theoretical section. The output is the power generated per wave period. For a system where the damping and the frequency of the wave are equal, the power generated is determined by the displacement of the floater. A comparison is made to A. Bechlenberg's thesis [32], where a study is conducted for different shapes and arrays, starting with a single floater. The floater in this study has dimensions of 7x7x2 meters. For the comparison with the current model, the floater is scaled 1:5. The resulting dimensions of the rectangular floater are 1.4x1.4x0.4 meters. Since the model is in 2D, the dimensions are 1.4x0.4 meters.

For the current study, for a single floater, the damping coefficient is 2,500 kg/s, the angular velocity 1.56 rad/s and the displacement 67.5 cm. This results in a power production of 346.5 Watt, for the 1:5 model.

Since the model is in 2D model, the default depth is per meter, whereas the floater depth should be 1.4 meter. The power produced is therefore multiplied by 1.4, since all the properties remain the same due to 2D. The result is a power production of 485.1 Watt.

To obtain the value for the full-size model, the model is scaled to the original dimensions. Froude's scaling factors are used to scale the power. Power scales with $s^{3.5}$, where s is the scaling, which is 0.2 since the model is 1:5 of the original model. In the final model, both the floater and the wave are scaled 1:5. The final result for the power produced for a full-scale model is 135,828 Watt.

The results from Bechlenberg's [32] study are analyzed for different frequencies. To identify the correct angular velocity from Figure 99, the full-scale angular velocity is used. For the original, full-scale wave, the period is 9s and therefore has an angular velocity of 0.69 rad/s. From Figure 99, the power produced for this specific frequency is about 64,000 Watt.
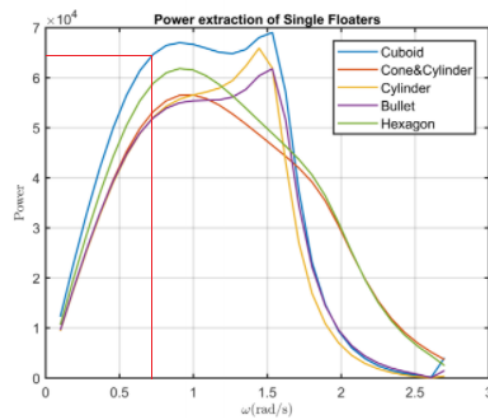
Figure 99: Power generated graph from A.Bechlenberg's study [18].

There is a large difference between these studies, which can be explained by a few considerations.

- The main difference lies in the approach of the study, where the calculations in the time-domain are three-dimensional and for the current study only two dimensions are considered. The main drawback of the current study is that the water cannot flow around the floater. The result of this is that the damping coefficient is a lot higher compared to Bechlenberg's study. In Bechlenberg's study, the damping coefficient is 41.788 kg/s for the full-scale model. For the current study, the full-scale damping coefficient can be calculated with Froude's scaling factors as well, where the scaling factor is $s^2.5$, resulting in a damping coefficient of 111,803 kg/s which is 2.7 times larger compared to Bechlenberg's study.

- There is a very long list of assumptions for the time-domain model. For the current model, there are also some assumptions, therefore a direct comparison is almost impossible to make. An example of an assumption for the time-domain model is that the submerged area of a floater is always half of the total area, which does not make sense in comparison to the results from the current study, where the submerged area differs a lot, even during a single period.

To eliminate the main difference, the 2D vs the 3D approach, the damping coefficient from Bechlenberg's study is used for the current model. The results are a full-scale power production of 67,076 Watt, which is very comparable. In short, the comparison to a time-domain model is quite hard since both approaches are completely different, although the results are in line with each other, especially when one reduces the damping coefficient to a realistic value to create a more comparable situation. The current model over-estimates the power production, since the damping coefficient is too high because of the 2D approach, forcing the fluid to act on the floater instead of flowing around the floater.

10.2 Power generation

As mentioned before, the power produced is calculated per period. To obtain some insight into power production over time, the instantaneous power is presented in Figure 100. Along with the instantaneous power, the floater heave is presented as well, to obtain some insight into the power production during a period.
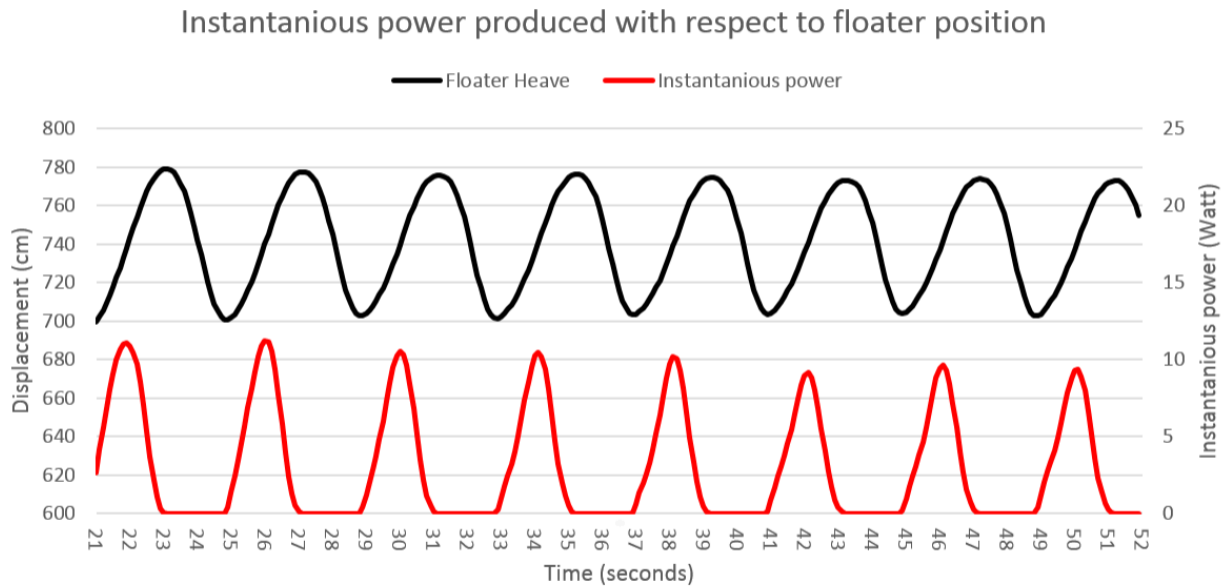
Figure 100: Instantaneous power generated, per 0.1s.

Power is only produced when the floater is in an upwards motion, as expected. Furthermore, there seems to be a trend where the power generated differs quite a lot during a single upwards motion. The instantaneous power is at largest when the floater is about halfway to its maximum heave. The lowest amount of instantaneous power is produced near the beginning and the end of the upwards motion. The main reason for this is the velocity of the floater. As one can expect, when the displacement per time unit is higher, more power is generated. The velocity of the floater follows a similar profile, where the velocity is the largest when the floater is about halfway to its maximum heave. The trend is clear and in line with the rest of the results.

For the different shapes, arrays and connections it does not make sense to evaluate the power, since the angular frequency and damping coefficient are equal, where the heave solely determines the power production.

11   Discussion

The discussion consists of two sections. In the first section, the results of the model are discussed. In the second section, the model itself is discussed.

11.1   Discussion of results

For the preliminary results, the viscosity tuning parameter has been investigated. The result is that for a viscosity tuning parameter of 1, almost all the reflection was absorbed. The reflection is absorbed because of the increase in viscosity. The increase in viscosity dampens the wave quite effectively because the velocity/energy of the wave is reduced when entering the absorption layer [42]. For smaller values, standing waves were found, which implies that there is not enough damping. The effects of reflection are larger for locations further from the wavemaker, since the absorption layer is closer. The further the location from the absorption layer, the lesser the reflection that was found. This is because the reflected waves are partially diffused during the propagation. The main drawback of using this type of absorption is that it is non-physical and cannot be tested empirically.

The mesh refinement study provides valuable information on the minimum size of the mesh. The minimum number of elements per wave height was found. A drawback of the mesh is the difference in element size near the floaters. The size of the elements is quite different, due to the chosen mesh. This is not necessarily bad, but it might influence the solution because of the different shapes and sizes. Concerning the moving mesh, the element quality remains high during the transient study and inversion of elements did not occur.

The damping coefficient is maximized for the incident wave to maximize power production. The maximum damping coefficient is found where the floater has the highest damping coefficient without submergence. Whether a floater submerges is dependent on the total area and mass of the floater. Besides floater properties, the damping coefficient is also dependent on the period of the wave. The main reason is that the resistance of the damping is higher for a higher velocity of the floater. If the period is smaller, the upwards velocity is larger and the damping coefficient should therefore be decreased.

The main result for the scaled floater is that for damping coefficients higher than 2,500kg/s, the floater submerges. For the large floater, there was no case of submergence, caused by the increase in area and thus the buoyancy of the floater.

The damping coefficient in the current study is higher compared to a previous study, conducted in a time-domain model. The main reason for this is because the model is 2D. For 2D, the fluid flow is forced to act on the floater. For a 3D model, the flow can go around the floater. It is important to keep in mind that for a 2D simulation, the damping coefficient is overestimated.

From the instantaneous power produced, it was concluded that during heave, the velocities differ quite a lot. The damping coefficient is dependent on the velocity of the floater. In an ideal case, the damping coefficient changes during heave, to adapt to the velocity of the floater to maximize power extraction. In a real-life context, this would be quite hard, since the damping coefficient is regulated by changing pumps, with different properties (e.g a larger area and thus a larger mass). For the model, on the other hand, the piece-wise function of the damping coefficient could have been smoothed, to adapt to the velocity of the floater.

In this study, a relation between the amount of energy extracted and the wave height after energy extraction is found. If more energy is extracted, the wave height further in the domain is lower. A lower wave height implies that the energy present in the wave is lower since less potential energy is stored. This is logical since energy cannot be created or destroyed. The energy extraction reduces the energy present in the waves.

For the rectangular fixed floater array, the second floater has the highest response. This is caused by the radiation effects of the neighboring floaters. The denser the array is, the higher the total heave is. The main

reason for this is that a denser floater array makes better use of the radiation effects. For a more sparse array, the radiation effects are less dominant, due to the diffusion of the wave because of the longer distance. The effect of spacing on the radiation in this study is that for a more sparse array, the radiation effects are smaller. As discussed before, an increase in the distance might increase the radiation effects, if the flow is fully developed between the floaters. The fourth floater performs the worst in all cases, since the energy available in the wave is reduced by previous floaters and there is little influence of radiation.

For the conical shape, the main finding is that the total heave is less compared to the rectangular floaters. The flow field is disturbed before reaching the floater, losing energy. Besides this, due to the shape, the floaters' response is delayed. The performance is worse than expected, mainly because the conical floater is designed for a 3D environment, so the flow can develop around the floater. Conical floaters are not an efficient shape for 2D simulations.

Overall, the connected array performs a bit worse compared to the fixed array. The main reason is that rotation occurs more often, because of the floaters' surge motion. The surge motion pushes the floaters towards each other, hence the distance joint causes rotation. Both the rotation and surge motion is a 'waste' of energy, causing the slightly worse performance. In extreme situations, collisions might occur, because the second floater is forced underwater because of the constraints in combination with the 'pushing' floaters. Please note that this is only the case for this simulations, since the first floater is fixed. In a real-life system the first floater is connected to a rigid pole and is able to move slightly. It is still important to keep the floaters' surge motions in control.

Another effect of the rectangular, connected arrays is that the variance of the floaters' heave is less. This implies that the difference in heave for the four floaters is smaller. This is logical since the floaters are connected and influence each other's motion. From a design perspective, this is a desirable effect. If the floaters' variance is lower, the damping coefficient can be tuned easier and the system is easier to design since the motions are more equal. On the other hand, for the connected conical arrays, the variance per single floater is higher. This implies that a floater has different elevation profiles for different periods. This is caused by the rotation of the floater and the interaction with neighboring floaters. This is an undesirable effect since it decreases the predictability and consistency of the motion. For the rectangular floaters, the variance per floater is low, resulting in a predictable and constant motion.

To decrease the rotation of the floaters a suggestion is to change the connection points between floater. Currently, for both the rectangular and the conical floater, the PTO is connected to the center of mass, reinforcing rotations. To reduce the rotation, the PTO could be connected to the lower boundary of the floater. To reduce the rotation of the floater. Besides changing the connection of the PTO, the connections between the floaters could be changed as well. An example is that, in previous iterations of the model, the floaters were connected at the center of mass, which resulted in even larger rotation. Because of the large rotations, it was decided to connect to floaters at the sides.

The effect of rotation and displacement (surge) was identified. The surge is caused by the direction of the flow field. Because the flow field rotates direction twice per period, the floater moves to the left and the right once per period. This motion must be considered when designing a floater array. Interactions like the surge motion have not been identified in previous models and is an important finding of this study.

11.2   Discussion of the model

In this section, the model and its assumptions are discussed.

11.2.1   CFD

Overall, the CFD approach is very useful. The current CFD study adds a lot of knowledge to the previous models. The most important aspects are the behavior of the floaters and the flow field. Besides this, the energy balances are correct and therefore conservation of energy is satisfied. CFD proves to be useful and

is therefore recommended for further studies on wave energy converters as well. The main drawback as mentioned before is the extensive calculation time.

11.2.2 Discussion of 2D approach

As mentioned before in this report, the 2D approach is the major drawback of this study. The most important effect is that the fluid cannot flow around an object, but is forced to act upon the object which results in:

- The damping coefficient being larger compared to a previous study.

- The rotation of the floaters being larger than expected.

- The surge motion of the floaters being stronger than expected.

The overestimation of the damping coefficient was discussed before. The rotation is also stronger than expected. The main reason for the rotation is the same as for the damping coefficient since the flow is forced to act upon the floater. Because of this, the floaters rotate a lot, to cope with the large incoming forces/velocities due to the 2D approach. The surge motion is also a lot stronger. The surge motion is caused by the direction of the flow field, which forces the floaters to move. In a 3D situation, the floater would displace less, since the flow would go around the floaters. An extreme example is a situation where floaters are submerged due to the surge motions of other floaters, pushing the floater downwards. This would not occur in a 3D situation since the flow is not forced to act upon the object but would change direction.

Overall, the effect of the 2D approach does have a large impact on the results and is difficult to compare to a 3D model directly. On the other hand, the 2D approach contains useful information; an example is a previous design of the Ocean Grazer. In the original design, the Ocean Grazer 1.0 (see Figure 101), the waves are directed through channels.
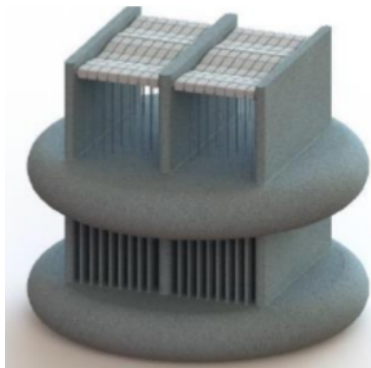

Figure 101: A previous iteration of the Ocean Grazer, where the waves are directed through a channel [42].

For this specific design, a 2D approach is a realistic approach and the results from the model are directly applicable. The results are quite useful since the damping coefficient and therefore the energy produced can be higher if the waves are directed through a channel. If such a design is created, it is important to keep in mind that not only the damping coefficient increases but so do the rotation and displacement. The major drawback of such a design is the increase in wall resistance, because of the channels. In this study, it was found that the damping coefficient is 2.7 times larger in a 2D case, which outweighs the effects of boundary layer formation on the channels easily.

Though the 2D model cannot be directly compared to the 3D model, the results are still quite useful and applicable to 3D situations. The main message here is to keep the 2D effects into account while interpreting/using the results from such a study.

11.3   Fixation of the first floater in connected arrays

One of the main assumptions made in the model for the connected arrays is that the first floater is fixed in surge. In a real system, this would not exactly be the case, as the first floater would be connected to a wind turbine or some other construction. The difference is then that in the real system, the array is able to move when the connection to the wind turbine would become slack, compressing the array. The effect of the fixation of the first floater is quite large as explained before. Because of the fixed floater, the array is 'compressed' and 'stretched', instead of the first floater moving with the flow, causing rotations and collisions. The recommendation is to connect the first floater to a defined point in space. This has been developed in COMSOL, but the model did not converge for any of the settings.

11.4   Scaling effects

Froude's scaling factors do not take the viscosity and surface tension into account, causing come scaling effects. The viscosity does have an impact on the waves since the waves are also partially damped by the viscosity of the water [49]. Besides viscosity, the surface tension is not scaled either. The scaling of surface tension has an effect on small-scale models, if the wavelength is smaller than 2 meters [50]. In the current study, the wavelength is about 20 meters and the scaling effects from surface tension are negligible. Overall, it is not expected that the scaling effects have an impact on the results, mainly because the model is only scaled 1:5. The dimensions, damping coefficient, displacement and accordingly power produced do not have scaling effects, since all the factors are taken into account using Froude's scaling factors.

11.5   Number of floaters

Another drawback of this study is that for cases 10, 11 and 12, the number of floaters was reduced to 3. The reason for this is convergence issues due to the increased complexity. The main issue with the reduction in the number of floaters is that it is harder to make a comparison between the fixed and connected array.

11.6   COMSOL

In general, COMSOL was a proper tool for this research. However, it comes with a few limitations found during the development of the model, which are listed below:

- 3D: The main shortcoming of COMSOL is that during this research, it was not possible to obtain a working 3D model. The main issue lies with the phase field module, which does not work well in 3D.

- Phase field: Besides problems in 3D, another problem with the phase field module occurred. The main problem is that the interface thickness is still relatively large, which can cause some inaccuracies for the floaters movement.

- Convergence: For some of the more complex models, the solver is not able to converge during the initial time step. The main cause for this is that the initial solution, found by the stationary solver, differs a lot from the first timestep of the transient solver. Convergence issues were only found for the initial time step.

- Contact pairs: Another drawback is the fact that for the current model, COMSOL is not able to deal with contact between two floaters. Secondly, due to the same reason, it is not possible to use the boundary as a wavemaker, which would have reduced the computational resources significantly.

- Licenses: Since COMSOL is commercial software, licenses have to be purchased to use the software. Besides the purchase of a license, it is not possible to run multiple calculations in parallel, since each session needs a separate license.

11.7   Recommendations

In this section, the recommendations for further research are discussed.

11.7.1 OpenFOAM/ComFLOW (3D)

The main recommendation is to conduct a similar study in a different software environment. OpenFOAM would be the first choice, mainly due to the wide availability of packages and add-ons. It is recommended to construct a 3D model, mainly to compare to the 2D model in the current study. A 3D model would be possible in OpenFOAM since it is a CFD specialized package. OpenFOAM is also free to use and calculations can run in parallel, saving a lot of computational resources. ComFLOW might be an option as well since it focuses on offshore marine structures.

11.7.2 Different frequencies and irregular waves.

In the current study, the wave properties do not change. The wave height and period are the same for each simulation. Changing the wave parameters would be interesting, to see what the effects of different frequencies are. The addition of irregular waves would be insightful. The current model can create irregular waves, but due to time restrictions, irregular waves are not considered.

The model is currently fully modular, designed so it can be used for different parameters. Due to the time restrictions of the project, only a small subset of parameters were changed to identify the effects. It is recommended to further investigate the model. Suggestions are the wave properties, the inclusion of regular waves, different floater shapes and more complex arrays. Concerning the damping coefficient, this could be changed for each timestep, to adapt to the velocity of the floater and maximize the power generation.

11.8 Full scale model

To truly ensure that there are no scaling effects, a full-scale model should be developed to investigate the effect of scaling. This would be possible by changing the dimensions of the current model but it would take a long time to compute. The estimated time to compute the model is about 480 hours.

12 Conclusion

In this chapter, the conclusions for the research are given.

12.1 Conclusion on the damping coefficient

To obtain insight into the effect of the damping coefficient, a comparison is made between a smaller scaled floater and a large floater. For the small floater, the effect of the damping coefficient was clear, where a too high damping coefficient results in submergence of the floater, which is an undesirable effect. For a single small floater, the optimal damping coefficient is 2,500 kg/s. For higher damping coefficients, besides submergence, the period of the motion changes as well. The change in period is caused by the damping factor, slowing down the motion of the floater. In extreme cases, the floater is out of phase, due to the high damping coefficient. In the end, the damping coefficient is dominated by heave because the term is squared to calculate the power produced.

The damping coefficient has a large impact on the energy density of the wave after the energy extraction of the floaters. For higher damping coefficients, more power is produced, and the surface elevation of the wave further in the domain is lower. This is logical since extraction of energy is directly related to the energy left in the wave. The surface elevation is not the only factor determining the energy in the wave, since the period is also important. It is therefore not accurate to calculate the energy in a wave solely from the surface elevation, although it does indicate the energy present.

For a larger floater, the total buoyancy force is higher, resulting in a higher damping coefficient without submergence. The main reason for this is the increase in area. The big floater is not optimized, since there have been no cases of submergence. For the large floater, the effect of the floater's energy extraction on the wave is easier to identify. As with the small floater, a decrease in the surface elevation further in the domain was identified for higher energy extraction.

12.2 Conclusion for fixed arrays

For the different fixed arrays, some differences have been found. For the rectangular floater array, a more dense array performs better; the gain with respect to worst case, case 3 (distance 2m) is 12.0 % and 10.7% for the first and second case respectively. Besides the total average displacement, the variance for the displacement of the different floaters differs quite a lot. For a more dense array, the variance is lower. This is quite important for the design of floater arrays since it is desirable to have low variance. The main reason for this is that it is easier to tune the floaters, but also concerns their performance.

For all the cases, the second floater has the largest displacement in heave. The main reason is the radiation effects of other floaters. Besides the radiation, due to the 2D approach, the larger displacements for the second and third floater might be caused by a higher local surface elevation between the floaters, due to water being 'trapped' between floaters. The fourth floater performs the worst for all the cases since it benefits little from radiation effects and the energy in the wave is low for the fourth floater.

For the conical floaters, the performance is lower compared to that of the rectangular array. The worst performing array for the conical floaters is with a distance of 2 meters. The gain for cases 4 and 5 with respect to case 6, the worst case, is 4.4 % and 4.3 %, respectively. The trend is the same as for the rectangular floaters, where a more dense array outperforms a sparse array, but the difference is smaller. As with the rectangular floaters, the variance is lower for a denser array, which is beneficial.

The rotation of the conical floaters is higher, which is undesirable since rotation is a waste of energy and disturbs the flow field. The main reason for the increase in the rotation is the unstable geometry. Besides this, the conical floaters have a delayed response to the surface elevation. This is caused by the shape, where

the submerged area increases with the height of the floater.

In general, for the fixed floaters, the rectangular floaters outperform the conical floaters. The distance between the floaters has a more dominant effect on the rectangular floaters compared to the conical floaters. The largest difference with the average heave is found by the fourth floater, which performs the worst in all cases.

12.3   Conclusion for connected arrays

For the final six cases, multibody dynamics have been introduced, to connect the floaters to each other. The main reason for this is to find the effect of the connection and the interactions of the bodies. For case 8, the floaters collide, which is undesirable and left out of the results. For the connected floaters, the average heave is in line with the fixed bodies, whereas the connected bodies perform a little worse, mainly due to rotations and surge motions.

The variance in heave per period per floater is higher for the connected arrays. This implies that the heave differs per period for any of the floaters. This effect was not found for the fixed cases. The main cause for this is due to the rotation of the bodies, caused by surge motions. The surge motion of a floater causes the rotation of other floaters, due to the connection. Large variances occurred for case 10: during the first and third period the elevation for the first floater was 66.5 cm and for the second and fourth period 79.3 cm. Overall, the connected bodies perform a bit worse.

Where the variance of a floater per period is worse, the variance between the heave of the different floaters is better. Overall, for the connected floaters, the variance was less between floaters. The main reason for this is because the floaters are connected and can 'support' each other. For longer distances between the floaters, the variance is higher compared to dense arrays.

Besides heave, for the connected array, surge is also an important motion. The surge of the floaters is in line with the direction of the flow field. During the crest, the direction of the flow field is in line with the wave propagation. This causes the array to be 'stretched'. On the other hand, during the trough, the direction of the flow field is opposite to the wave propagation, causing the array to 'compress'. From the surge motion plots, this effect can be seen clearly, where the maximum and minimum displacement with respect to the initial position occurs twice per period.

The rotation of connected floaters affects the displacement of other floaters. The main reason for this is that the connection points are located at the sides of the floaters. A rotation changes the position of the connection and therefore the floater pulls the neighboring floater towards it.
This also goes the other way, where the displacement of a floater forces neighboring floaters to react, by either rotation or displacement.

12.4   Conclusion of the flow field analysis

The flow field is influenced by the presence of the floaters. The areas that are affected the most are the areas between floaters. The main reason for this is that it is difficult for the flow to stabilize between the floaters since the area can only be reached when the direction of the flow field is upwards, which occurs once per period. For the rest of the period, there is barely any velocity present between the floaters, causing a low energy density between the floaters. Due to the 2D approach, this effect is larger, because the fluid is 'trapped' between the floaters.

The flow is least disturbed during the up and downwards motion of the floaters. The main reason for this is that the direction of the flow field is in line with the direction of the floaters. For downwards motions, the fluid beneath the floater is accelerated, since the floaters' velocity is larger compared to the velocity of the

fluid. This also causes radiation effects. For the conical floater, the flow is not directly up or downwards, but more to the side due to the geometry.

For the conical floater, the redirection of the flow is not as expected. Because of the shape, the flow is already disturbed before it reaches the floater. The hypothesis for the conical floater was that due to the shape, the heave would increase, since the fluid is directed downwards because of the sloped side.

The disturbance between the floaters is different for the different arrays. For a more dense array, the area between the floaters is smaller. Because of the smaller area, it is harder for the flow to develop. This is partially due to the shape of the floaters (it is not the case for conical floaters). Another reason is that the window of opportunity for the flow to reach the area is smaller. This is caused by the changing direction of the flow. For less dense arrays, the flow field between the floaters is able to stabilize and follow the rest of the flow field.

The disturbance of the flow field behind the floater array is visible as well. For a small region, the flow field is not in line with the rest of the field. As mentioned before, the flow is able to stabilize very quickly overall. In short, the effect of energy extraction is visible in the flow field further in the domain.

12.5 Conclusion for energy extraction

A comparison is made to Bechlenberg's (2018) study. This study used a three dimensional time-domain model. The model parameters where matched as close as possible to those of Bechlenberg's thesis. The result is that the current model produces double the amount of energy compared to the previous study. The main explanation for this is due to the 2D approach. In 2D, the flow is forced to act on the floater; in 3D, the flow can go around the floater. The high power generation is caused by a high damping coefficient, due to the 2D approach. For a better comparison, the damping coefficient used in Bechlenberg's study was used. Using this damping coefficient, the results are very comparable. The conclusion is that the 2D model overestimates the damping coefficient and therefore the power generated.

The instantaneous power differs over a period. The main reason for this is that the velocity of the floater is not equal during the upwards motions. The instantaneous power generated is smallest at the start and end of the heave motion.

12.6 Overall conclusion

The model works quite well, and most of the behavior is physical. The model created is useful for the analysis of different shapes and floater arrays. Besides this, the flow field analysis proves quite useful for the explanation of some of the behavior of the floaters and fluids. The main drawback of the model is the 2D approach.

A   Froude's scaling factors

Quantity	Scaling
Wave height and length	s
Wave period	$s^{0.5}$
Wave frequency	$s^{-0.5}$
Power density	$s^{2.5}$
Linear displacement	s
Angular displacement	1
Linear velocity	$s^{0.5}$
Angular velocity	$s^{-0.5}$
Linear acceleration	1
Angular acceleration	s^{-1}
Mass	s^{3}
Force	s^{3}
Torque	s^{4}
Power	$s^{3.5}$
Linear stiffness	s^{2}
Angular stiffness	s^{4}
Linear damping	$s^{2.5}$
Angular damping	$s^{4.5}$

Figure 102: Froude's scaling factors [51].

B   Peregrine code and manual

In this section, a short manual for the Peregrine cluster is given. For further information please consult the wiki of Peregrine. Under additional information, the course material can be found, which explains how to use Peregrine in-depth, along with some exercises (https://wiki.hpc.rug.nl/).

B.1   Connecting to the Peregrine cluster

First, download MobaXterm (https://mobaxterm.mobatek.net/). MobaXterm is a free linux environment, in a windows format. It is therefore, easy to use for both windows and MAC users. When downloaded and installed, please follow the steps below to connect to the cluster:

1. In the main menu, click on Session.

2. In the sessions settings, click on SSH (Secure Shell Protocol, which is the connection type to the cluster.)

3. Check the box for specify username and fill in your student number.

4. In 'remote host' type *peregrine.hpc.rug.nl*

5. Click on 'ok'

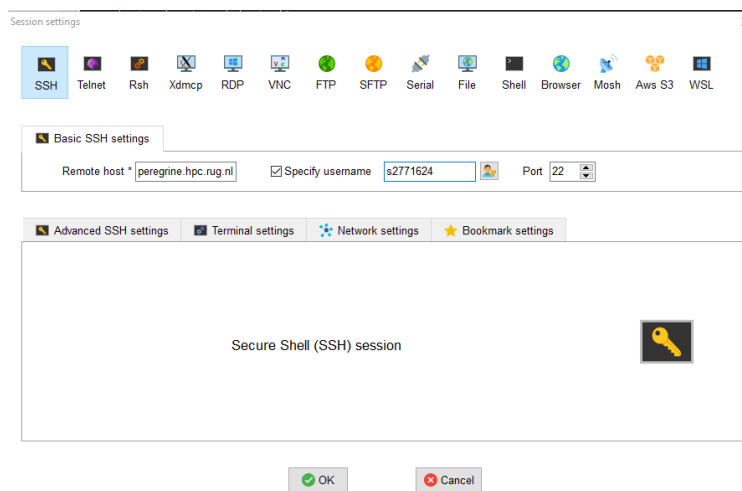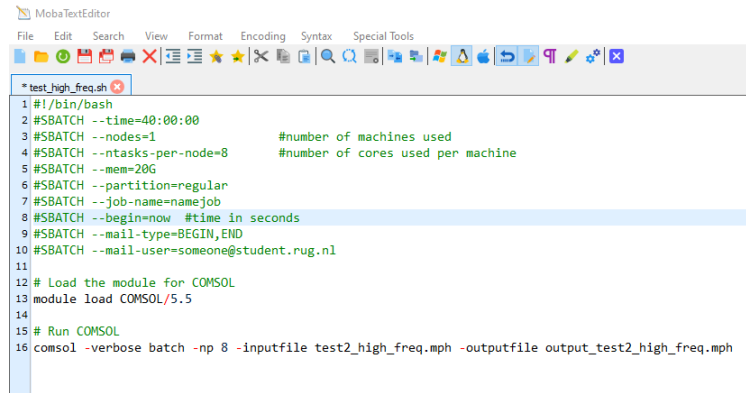6. Type your password in the terminal, please note that the password does not appear in the terminal.

Figure 103: SSH settings to connect to the Peregrine.

B.2   Creating folders and SLURM files

To run a model on Peregrine, aa sbatch command is used, which is a file with information on the resources used. Besides the resources, the in and output files are also stated here. To run a model, both the sbatch file and the model file should be in the same folder. To create a folder, right-click in the folder menu to create a folder. In the folder, upload the model and the SLURM file. The SLURM file is presented below.

Figure 104: SLURM file to schedule the job.

The SLURM file contains the following information:

- Time is the total duration of the model. Please note that when the time is exceeded, the job is cancelled, make sure to have sufficient time.

- Nodes is the amount of nodes (machines) used per model. A single node contains 22 to 24 cores.

- ntasks-per-node is the amount of cores used per node.

- mem is the total amount of memory used.

- job-name is the custom name for a job used to identify jobs.

- begin is when the job should start, in the current format, the job queues instantly. This can also be set to a predefined moment.

- mail-type is used to set when to receive e-mails. In this file, an e-mail is sent during the start and end of the job.

- mail-user is the email used to send the e-mails to.

- The module load command is used to load the module needed for the model, in this case COMSOL 5.5

- The -np is the number of cores used. This command is used to let COMSOL know how many core it should use. Therefore, -np x should be equal to ntasks-per-node. If using multiple nodes, it should be ntasks-per-node multiplied by the number of nodes used.

- Finally, the in and output files are the in an output file of the model. The name of the inputfile should be the same as the model file, the output file can be set freely.

Please note that the SLURM file should be saved as a .sh file. a .sh is a shell file, which is submitted as a job using a sbatch command. The complete SLURM file is presented in Appendix B.5.

B.3   Running a model

To run a model, one must change directory in the terminal. Please note that the navigation in the 'windows' menu on the left does not actually change the directory. To navigate to a directory, use the cd command. For example, to navigate to a folder, type cd foldername (to return to a previous folder, use cd ..). To navigate through multiple folders, use a backslash. For example to go from the home directory to a certain folder, type cd jobs/comsol/job1. For more information on linux commands, please consult the HPC wiki. In Figure 107 an example is given as well.

Once arrived in the right directory, one can use an sbatch command to run the model. To run a model, type sbatch nameslurmfile.sh. An example is given below.
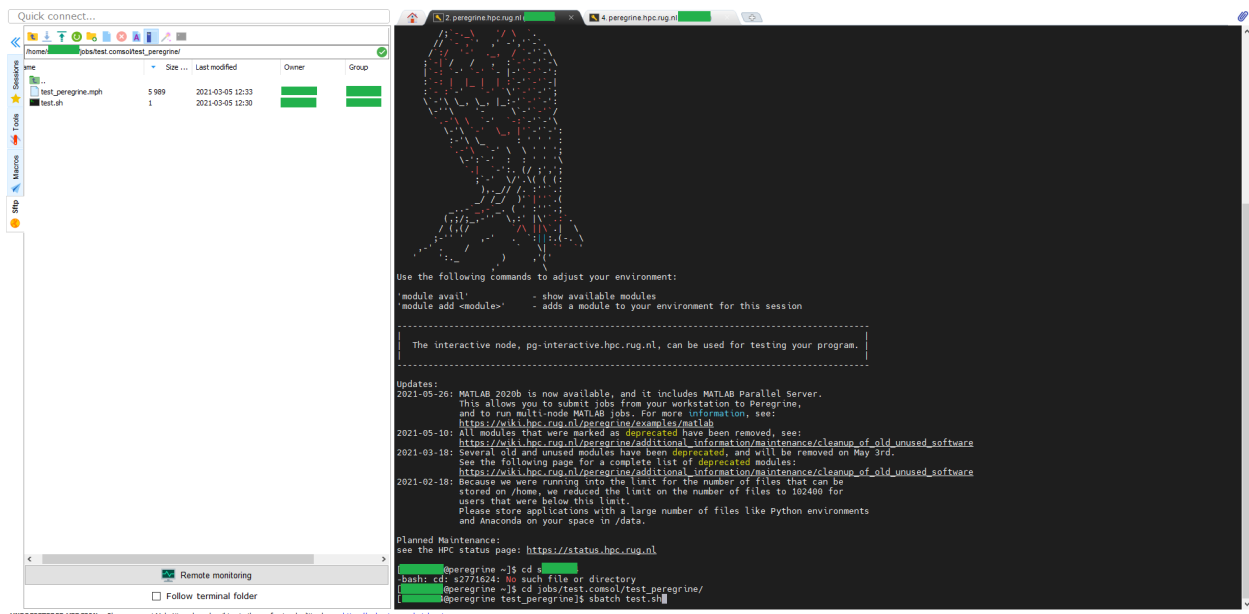

Figure 105: Running a job using the sbatch command. Please note the change in directory as well.

The job is now queued and will start when there is space available. Below are some useful commands to check on the progress of the model.

- When a job is submitted, the jobname is specified. To obtain information on this job, type *jobinfo xxxxxxxx (jobnumber)* to check on the job.

- As soon as a model starts running, an information file is generated. The files name is somewhat like *slurm-xxxxxxxx.out*. This file can be read using the cat command. When in the right directory, type cat slurm-xxxxxxxx.out and the file can be read to check on progress.

- Type squeue -u sxxxxxxx to check on active jobs.

- type scancel jobnumber to cancel a single job

- Type scancel -u sxxxxxxx to cancel all active jobs.

B.4   COMSOL Licenses

Since COMSOL is a commercial software, licenses are needed to run a COMSOL model. To check the availability of licenses, connect to the interactive node. To connect to the interactive node, create a new sessions as before, but connect to pg-interactive.hpc.rug.nl instead of peregrine.hpc.rug.nl. Use the following command after logging in:

/software/software/COMSOL/5.5/license/glnxa64/lmutil lmstat -a -c /software/software/COMSOL/5.5/license/license.dat

The available licenses and modules are presented in the list. Please note that there are only 3 licenses available for Peregrine at maximum.

B.5   Slurm file

The SLURM file used is presented below.

```
!/bin/bash
SBATCH --time=40:00:00
SBATCH --nodes=1
SBATCH --ntasks-per-node=8
SBATCH --mem=5G
SBATCH --partition=regular
SBATCH --job-name=testcomsol
SBATCH --begin=now

Load the module for COMSOL
module load COMSOL/5.5

Run COMSOL
comsol -verbose batch -np 8 -inputfile filename.mph -outputfile outputfilename.mph
```

C   Model

In this section, additional information on the model is presented.

C.1   Parameters

To use the model, most of the parameters of interest can be found in parameters 1, under global definitions. The main parameters are found below.

Name	Expression	Value	Description
width_floater	1[m]	1 m	width of the floaters
width_absorption	10[m]	10 m	width of the absorption layer
width	30[cm]*modifier*modifier_width	67.5 m	width domain
mu_water	0.0011	0.0011	dynamic viscosity water
modifier_width	1.5	1.5	modifier for width/height relation
modifier_viscosity	1	1	viscosity tuning parameter
modifier	150	150	modifier for sizing
height_floater	0.5[m]	0.5 m	height of the floatersr
height	10 [cm]*modifier	15 m	height domain
distance_floaters	1	1	distance between floaters [m]
damping_coefficient	2000	2000	damping coefficient of floaters
angular_velocity	((2*pi)/4)	1.5708	angular velocity of the wavemaker
angle_wavemaker	3	3	angle of the wavemaker

Figure 106: The main parameters of the study.

C.2   Absorption layer

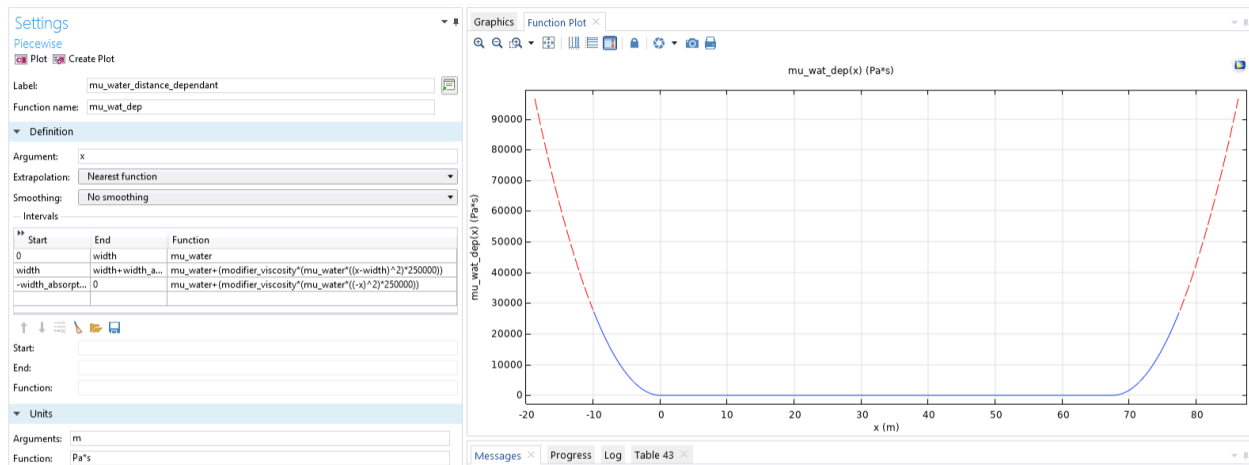The configuration for the absorption layer is presented below.

Figure 107: The settings for the absorption layer, the function mu wat dep is used as the dynamic viscosity of the water in the materials menu.

C.3   Damping coefficient

The piecewise function for the damping coefficient is presented below, where each floater has its own function. mbd.utY is the velocity of the floater.
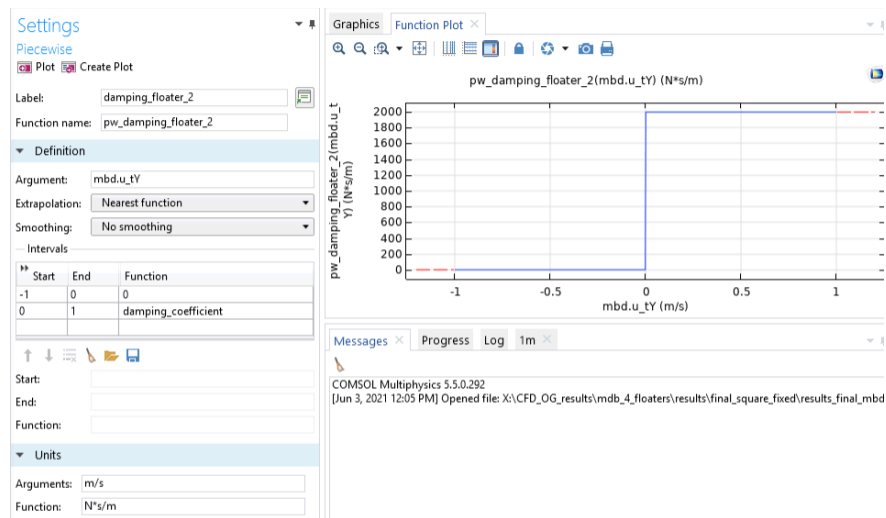

Figure 108: Piecewise functions for the damping coefficients for the floaters. The function damping floater 2 is used as the damping coefficient applied to the second floater.

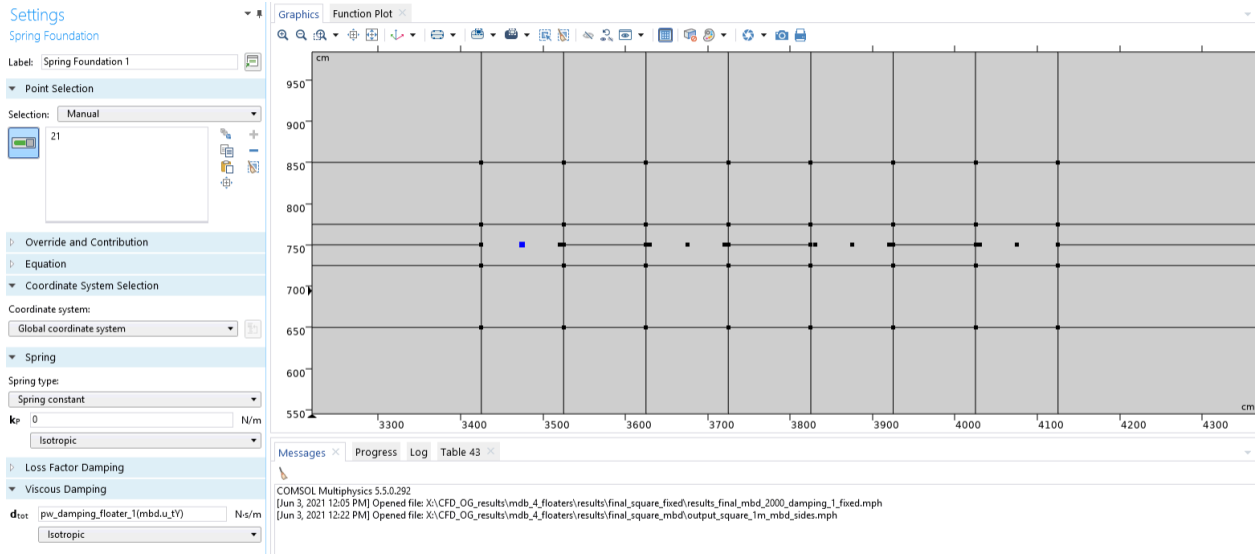The piecewise function is then applied to a certain point in the domain.

Figure 109: The selection of the damping location, in this case for floater 1.

C.4   Wavemaker

The wavemaker is controlled by the rotation axis base point and the wavefunction.
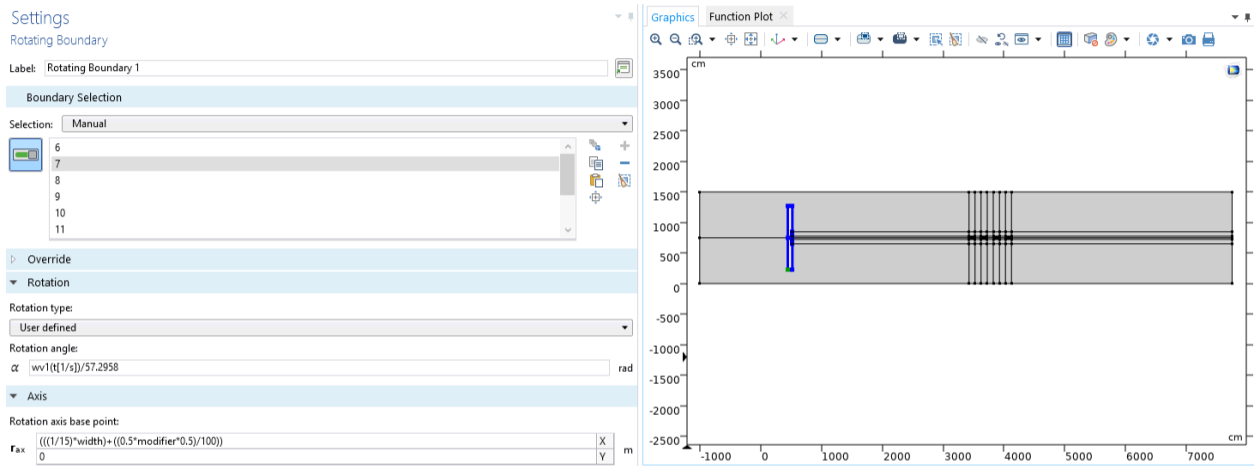

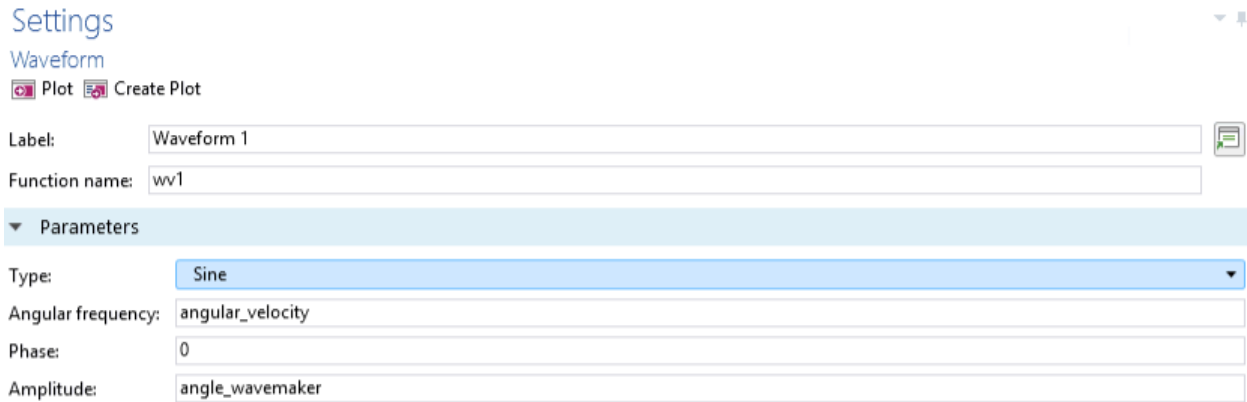Figure 110: Settings for the rotating boundary.

Figure 111: The waveform used to control the motion of the wavemaker.

C.5   Connections

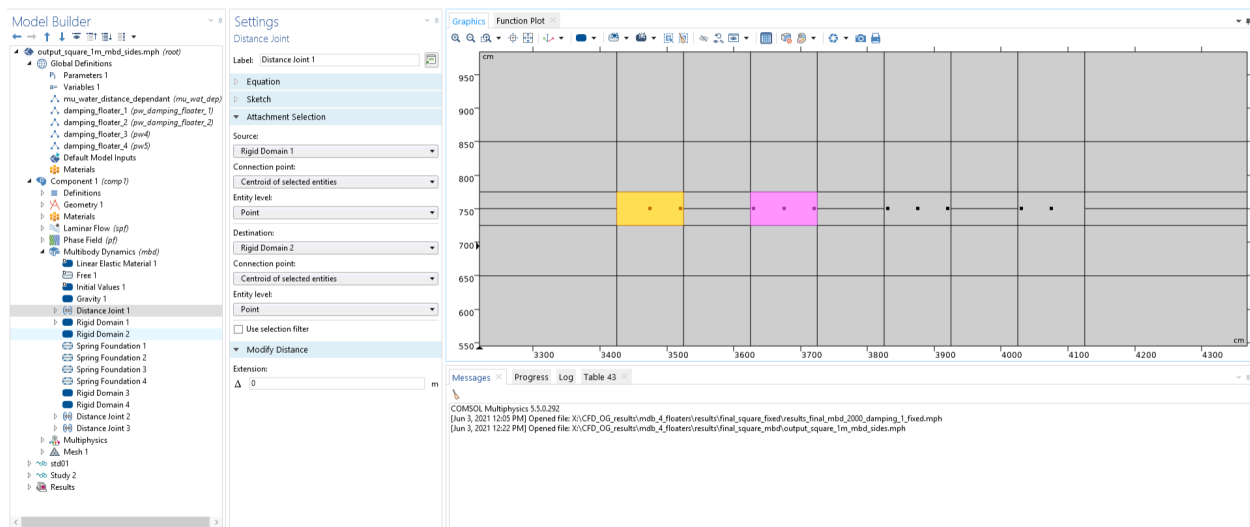An example for one of the connections is presented below.

Figure 112: The connection between the first and the second floater.

C.6   Phase field settings

The setting for the interface thickness and mobility tuning parameters can be found below.
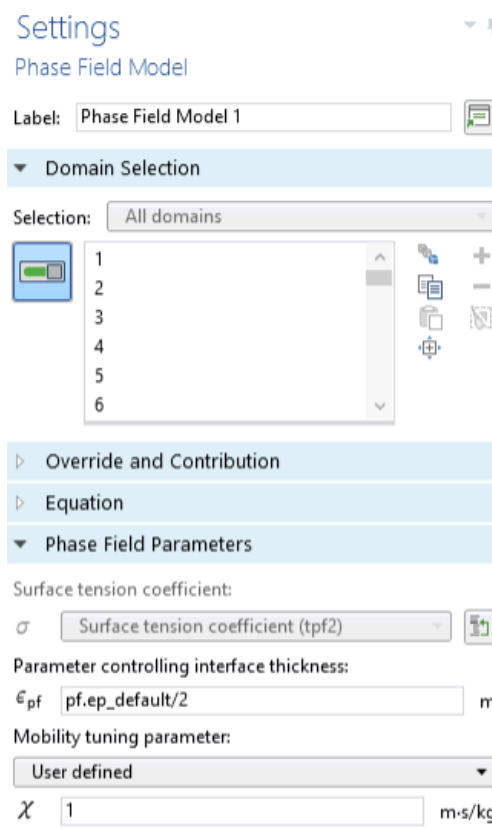
Figure 113: The setting for the phasefield.

C.7   Meshing

The mapped mesh is configured by setting a number of elements per boundary. The refinement of the mesh around the floaters is presented in Figure 115.
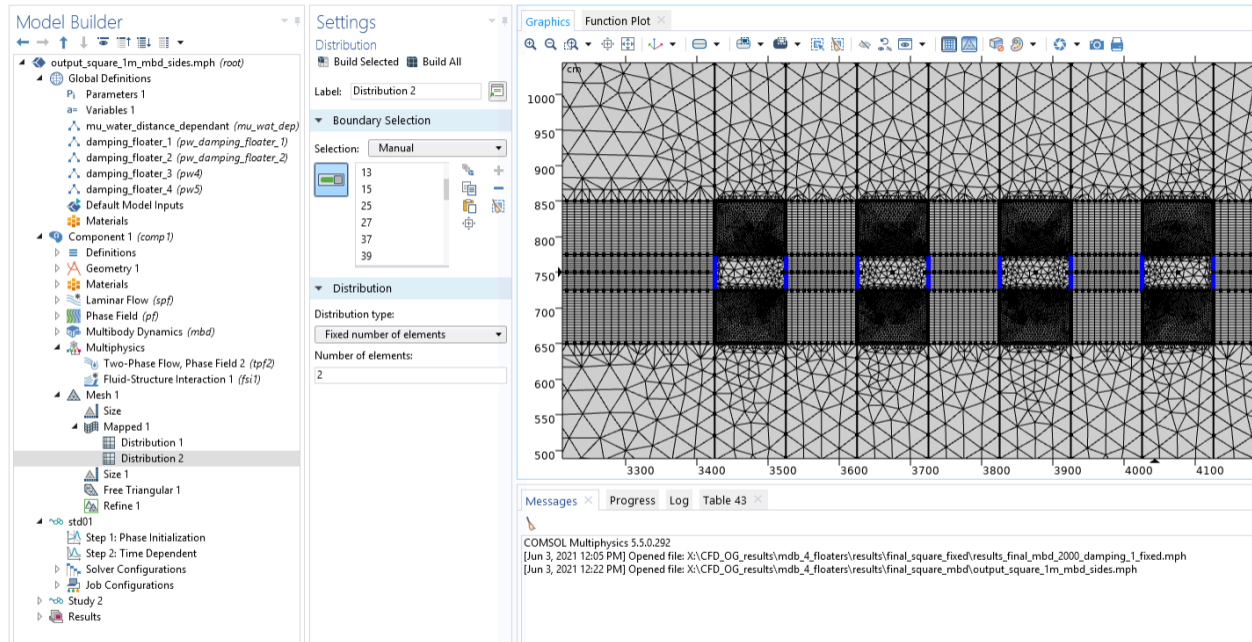
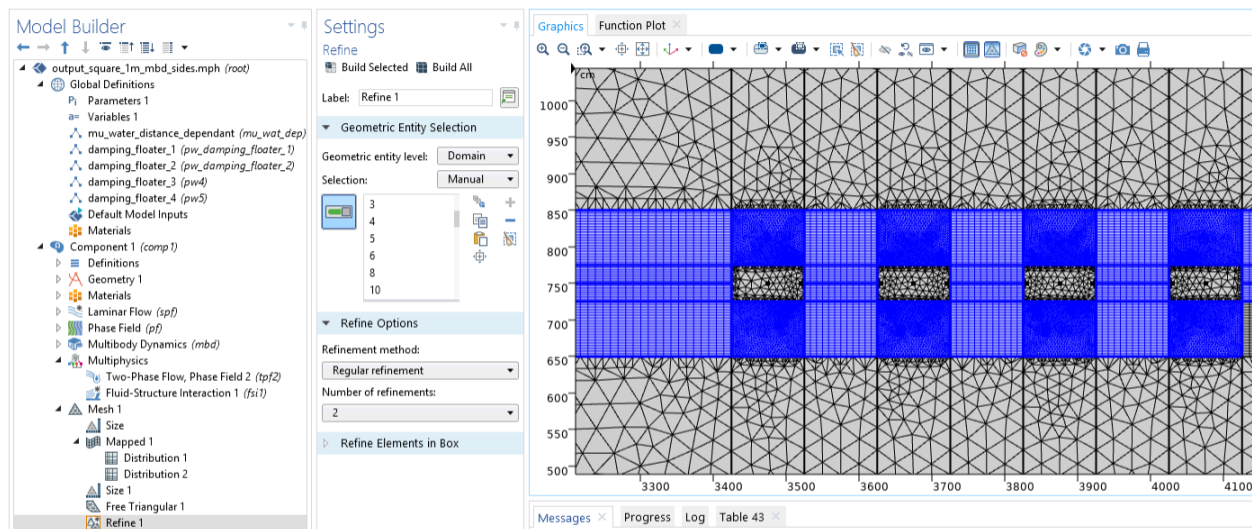Figure 114: Distribution of the mapped mesh for local refinement.

Figure 115: Local refinement of the mesh to comply with the mesh refinement study.

C.8   Multiphysics coupling

The multiphysics are coupled using two-phase flow (Figure 115) and fluid-structure interaction (Figure 116).

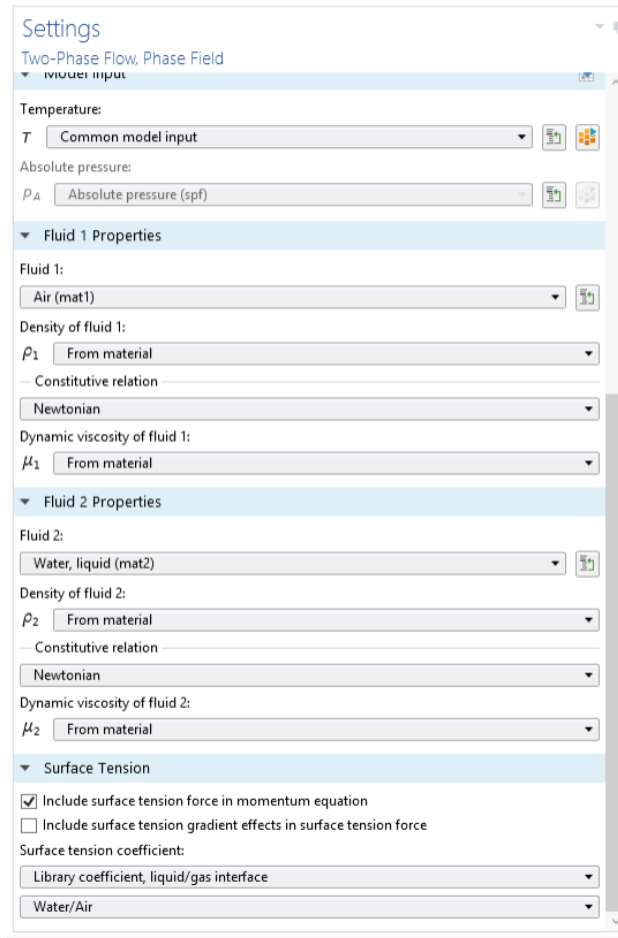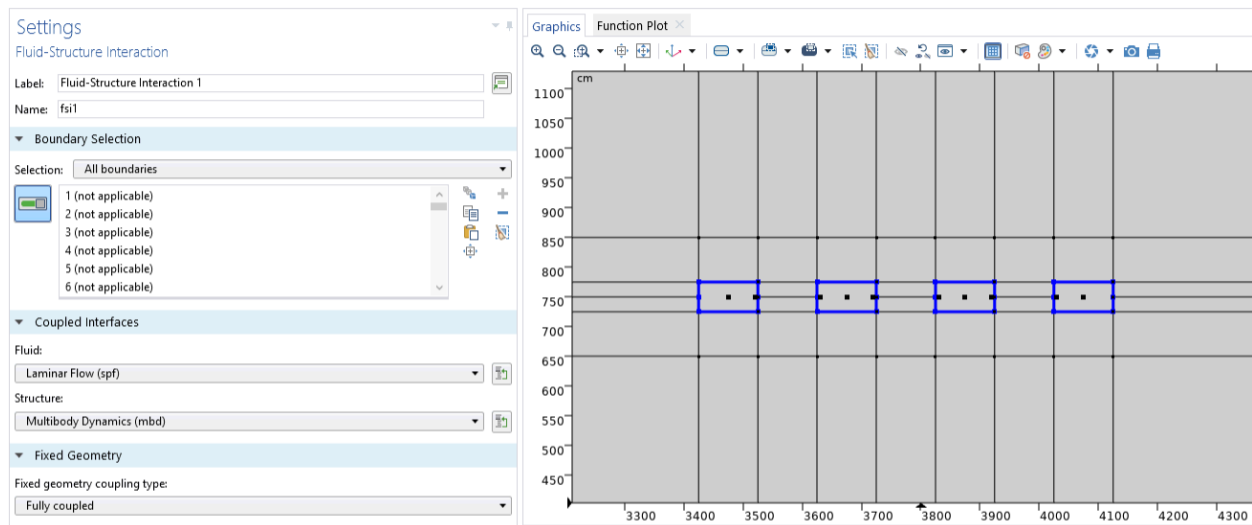Figure 116: Coupling of the fluid flow and phase field.

Figure 117: Coupling of the fluid flow and structure interactions.

C.9   File size reduction

To reduce the filesize (a single file is about 100 GB's) only a single timestep is saved every 10 timesteps. This is configured with the remove solutions function, see the settings below.
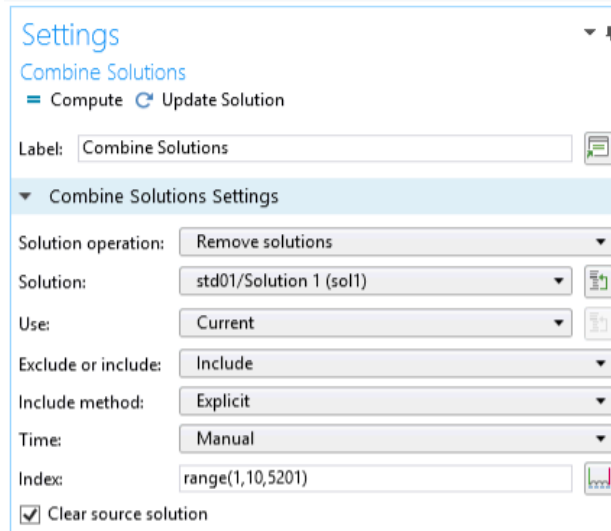

Figure 118: Coupling of the fluid flow and structure interactions.

References

[1] EIA, "International energy outlook 2020." `https://https://www.eia.gov/todayinenergy/detail.php?id=41433`, 2019. [Online; accessed 2-11-2020].

[2] H. Ritchie, "Fossil fuels," *Our World in Data*, 2017. https://ourworldindata.org/fossil-fuels.

[3] B. Dudley *et al.*, "Bp statistical review of world energy," *BP Statistical Review, London, UK, accessed Aug*, vol. 6, p. 2018, 2018.

[4] B. Dudley *et al.*, "Bp statistical review of world energy 2016," *London, UK*, 2015.

[5] M. Askari, M. Mirhabibi, M. Bahrampour, V. Mirzaei Mahmoud Abadi, and T. Mahdi, "Comparing the generation of electricity from renewable and non-renewable energy sources in iran and the world: now and future," *World Journal of Engineering*, vol. 12, p. 627–638, 12 2015.

[6] M. Z. Jacobson, "Review of solutions to global warming, air pollution, and energy security," *Energy & Environmental Science*, vol. 2, no. 2, pp. 148–173, 2009.

[7] G. R. Shaver, J. Canadell, F. S. Chapin, J. Gurevitch, J. Harte, G. Henry, P. Ineson, S. Jonasson, J. Melillo, L. Pitelka, *et al.*, "Global warming and terrestrial ecosystems: A conceptual framework for analysis: Ecosystem responses to global warming will be complex and varied. ecosystem warming experiments hold great potential for providing insights on ways terrestrial ecosystems will respond to upcoming decades of climate change. documentation of initial conditions provides the context for understanding and predicting ecosystem responses.," *Bioscience*, vol. 50, no. 10, pp. 871–882, 2000.

[8] P. Friedlingstein, M. Jones, M. O'sullivan, R. Andrew, J. Hauck, G. Peters, W. Peters, J. Pongratz, S. Sitch, C. Le Quéré, *et al.*, "Global carbon budget 2019," *Earth System Science Data*, vol. 11, no. 4, pp. 1783–1838, 2019.

[9] Rebecca Lindsey and LuAnn Dahlman, "Climate change: Global temperature." `https://www.climate.gov/news-features/understanding-climate/climate-change-global-temperature#:~:text=Change%20over%20time&text=According%20to%20the%20NOAA%202019,more%20than%20twice%20as%20great.`, 2020. [Online; accessed 2-11-2020].

[10] Michael Dhar, "How do solar panels work?." `https://www.livescience.com/41995-how-do-solar-panels-work.html`, 2017. [Online; accessed 2-11-2020].

[11] Woodford, Chris, "Wind turbines." `https://www.explainthatstuff.com/windturbines.html`, 2019. [Online; accessed 2-11-2020].

[12] P. A. Lynn, *Onshore and offshore wind energy: an introduction*. John Wiley & Sons, 2011.

[13] National Geographic Society, "Hydroelectric energy." `https://www.nationalgeographic.org/encyclopedia/hydroelectric-energy/#:~:text=Hydroelectric%20energy%2C%20also%20called%20hydroelectric,used%20this%20force%20for%20millennia.`, 2019. [Online; accessed 2-11-2020].

[14] Jack Unwin, "What is geothermal energy?." `https://www.power-technology.com/features/what-is-geothermal-energy/#:~:text=Geothermal%20energy%20is%20the%20heat,earth's%20hot%20molten%20rock%2C%20magma.`, 2019. [Online; accessed 2-11-2020].

[15] Talal Husseini, "Riding the renewable wave: tidal energy advantages and disadvantages?." `https://www.power-technology.com/features/tidal-energy-advantages-and-disadvantages/`, 2020. [Online; accessed 2-11-2020].

[16] Waves4Power, "Why wave power." `https://www.waves4power.com/why-wave-power/#:~:text=The%20Stable%20Energy%20Source&text=Sea%20states%20can%20be%20accurately,moves%20over%20the%20ocean%20surface.`, 2019. [Online; accessed 11-5-2021].

[17] Ocean Grazer , "Ocean energy for a sustainable future." `https://oceangrazer.com/`, 2020. [Online; accessed 3-11-2020].

[18] A. Bechlenberg, *Performance analysis and comparison of floater arrays in the ocean grazer 3.0 design.* PhD thesis, 2018.

[19] COMSOL, "-." `https://www.comsol.nl/`, 2021. [Online; accessed 27-3-2021].

[20] OpenFOAM, "About openfoam." `https://www.openfoam.com/`, 2021. [Online; accessed 27-3-2021].

[21] ComFLOW, "Comflow homepage." `http://www.math.rug.nl/~veldman/comflow/comflow.html`, 2021. [Online; accessed 25-5-2021].

[22] J. Cruz, *Ocean wave energy: current status and future prespectives.* Springer Science & Business Media, 2007.

[23] NEWS It's game over for investment bank Babcock Brown BY:SCOTT MURDOCH FromL , "It's game over for investment bank babcock brown?." `https://archive.vn/20120913200528/http://www.theaustralian.news.com.au/business/story/0,28124,25183580-36418,00.html#selection-1817.2-1817.52`, 2009. [Online; accessed 3-11-2020].

[24] H. He, Q. Qu, and J. Li, "Numerical simulation of section systems in the pelamis wave energy converter," *Advances in Mechanical Engineering*, vol. 5, pp. 186056–186056, 01 2015.

[25] E. Renzi, K. Doherty, A. Henry, and F. Dias, "How does oyster work? the simple interpretation of oyster mathematics," *European Journal of Mechanics - B/Fluids*, vol. 47, pp. 124–131, 04 2014.

[26] J. Sanjuan, C. Pimienta, and I. Oliveros, *Design and Analysis of a Wave Energy Converter of Point Absorber Type for the Energy Extraction from the Waves.* PhD thesis, 08 2019.

[27] Tom Lombardo , "World's largest wave energy farm." `https://www.engineering.com/ElectronicsDesign/ElectronicsDesignArticles/ArticleID/7162/Worlds-Largest-Wave-Energy-Farm.aspx`, 2014. [Online; accessed 3-11-2020].

[28] I. Hashem, H. A. Hameed, and M. Mohamed, "An axial turbine in an innovative oscillating water column (owc) device for sea-wave energy conversion," *Ocean Engineering*, vol. 164, pp. 536–562, 2018.

[29] Meredith Fish , "Overtopping terminator." `http://coastalenergyandenvironment.web.unc.edu/ocean-energy-generating-technologies/wave-energy/overtopping-terminator/`, 2012. [Online; accessed 3-11-2020].

[30] mikeatsea, "Waves 101." `https://mikeatsea.wordpress.com/2012/09/18/waves-101-part-1/`, 2012. [Online; accessed 11-11-2020].

[31] L. H. Holthuijsen, *Waves in oceanic and coastal waters.* Cambridge university press, 2010.

[32] R. de Winter, *Designing Ships using Constrained Multi-Objective Efficient Global Optimization.* PhD thesis, 05 2018.

[33] J. Falnes and A. Kurniawan, *Ocean waves and oscillating systems: linear interactions including wave-energy extraction*, vol. 8. Cambridge university press, 2020.

[34] Edingburgh designs, "Wave generators." `http://www4.edesign.co.uk/waves/some-wave-1/`, 2016. [Online; accessed 3-2-2021].

[35] MARINET, "Collation of wave simulation methods." `https://tethys.pnnl.gov/sites/default/files/publications/MARINET-D2.12.pdf`, 2014. [Online; accessed 3-2-2021].

[36] S. Michele, F. Buriani, E. Renzi, M. van Rooij, B. Jayawardhana, and A. I. Vakis, "Wave energy extraction by flexible floaters," *Energies*, vol. 13, no. 23, p. 6167, 2020.

[37] Jeff Hiller , "What is a pressure point constraint? when is it used?." `https://www.comsol.com/forum/thread/244582/what-is-a-pressure-point-constraint-when-is-it-used`, 2019. [Online; accessed 17-11-2020].

[38] B. E. Rapp, "Chapter 21-capillarity," *Microfluidics: Modelling, Mechanics and Mathematics*, pp. 445–451, 2017.

[39] CFD support, "slip vs noslip bc." `https://www.cfdsupport.com/OpenFOAM-Training-by-CFD-Support/node118.html`, 2016. [Online; accessed 3-2-2021].

[40] COMSOL, "Cfd module user's guide," in *User guides*, COMSOL, 2021.

[41] COMSOL, "Two-phase flow with fluid-structure interaction," in *Application library*, COMSOL, 2021.

[42] L. Martinelli and P. Ruol, "2d model of a floating body under nonlinear waves," in *Modelling and Simulation*, IntechOpen, 2008.

[43] V. I. Mauricio *et al.*, "Mechanical design of the ocean grazer's floater blanket," Master's thesis, Universitat Politècnica de Catalunya, 2019.

[44] Hrvoje Jasak, "Openfoam in wave and offshore cfd capabilities of the naval hydro pack," 2017.

[45] Y. Wei, A. Bechlenberg, M. van Rooij, B. Jayawardhana, and A. I. Vakis, "Modelling of a wave energy converter array with a nonlinear power take-off system in the frequency domain," *Applied Ocean Research*, vol. 90, p. 101824, 2019.

[46] G. De Backer, M. Vantorre, C. Beels, J. De Rouck, and P. Frigaard, "Performance of closely spaced point absorbers with constrained floater motion," in *The 8th European Wave and Tidal Conference: EWTEC 2009: Book of Abstracts*, pp. 53–54, The 8th European Wave and Tidal Conference, 2009.

[47] N. Sergiienko, B. Cazzolato, B. Ding, P. Hardy, and M. Arjomandi, "Performance comparison of the floating and fully submerged quasi-point absorber wave energy converters," *Renewable Energy*, vol. 108, pp. 425–437, 2017.

[48] R. Waters, *Energy from ocean waves: full scale experimental verification of a wave energy converter*. PhD thesis, Universitetsbiblioteket, 2008.

[49] Q. Zeng, R. Hekkenberg, C. Thill, and H. Hopman, "Scale effects on the wave-making resistance of ships sailing in shallow water," *Ocean Engineering*, vol. 212, p. 107654, 2020.

[50] D. Stagonas, D. Warbrick, G. Muller, and D. Magagna, "Surface tension effects on energy dissipation by small scale, experimental breaking waves," *Coastal Engineering*, vol. 58, no. 9, pp. 826–836, 2011.

[51] M. Islam, F. Jahra, and S. Hiscock, "Data analysis methodologies for hydrodynamic experiments in waves," *Journal of Naval Architecture and Marine Engineering*, vol. 13, p. 1, 06 2016.